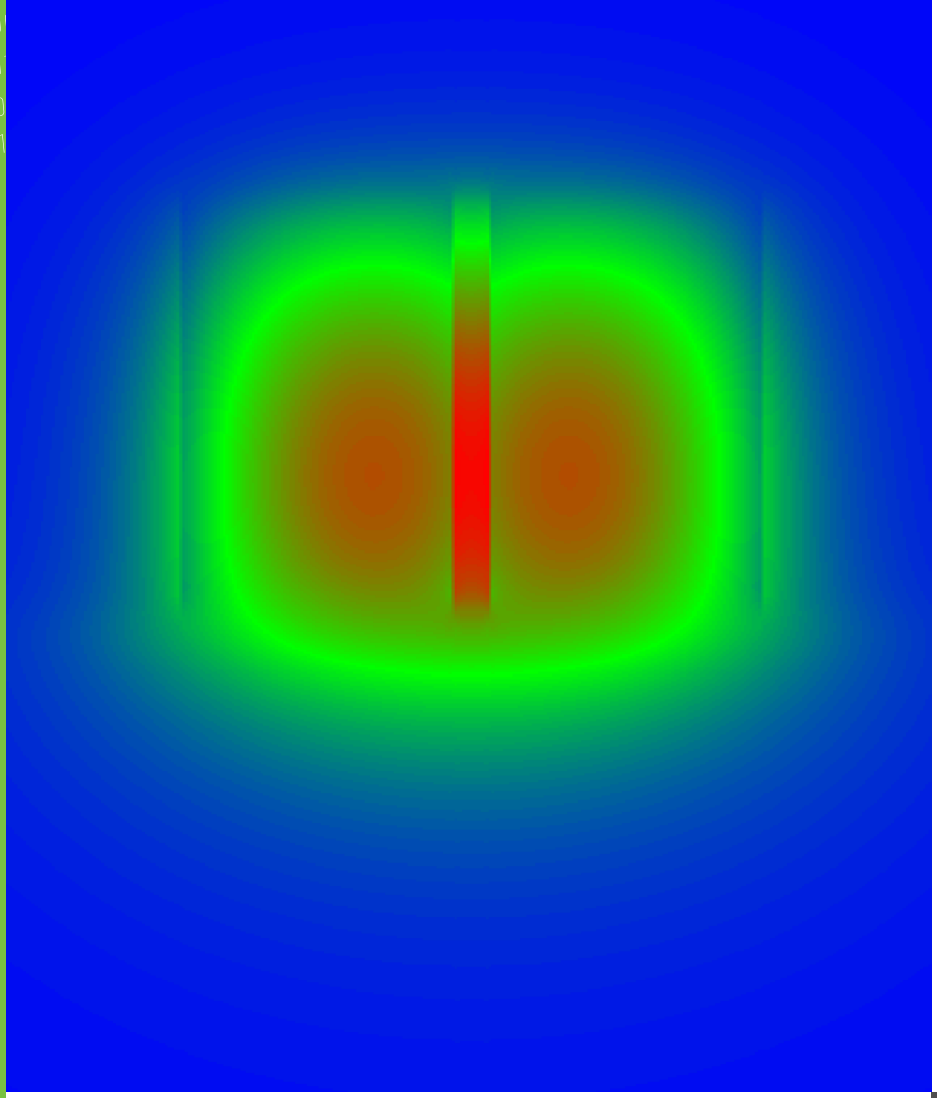

SCIENCE • TECHNOLOGY • RESEARCH HIGHLIGHTS • VISIONS

Dissertation
62

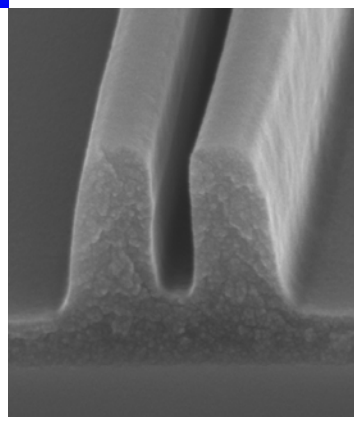

Polymeric slot waveguide interferometers

Marianne Hiltunen

VTT

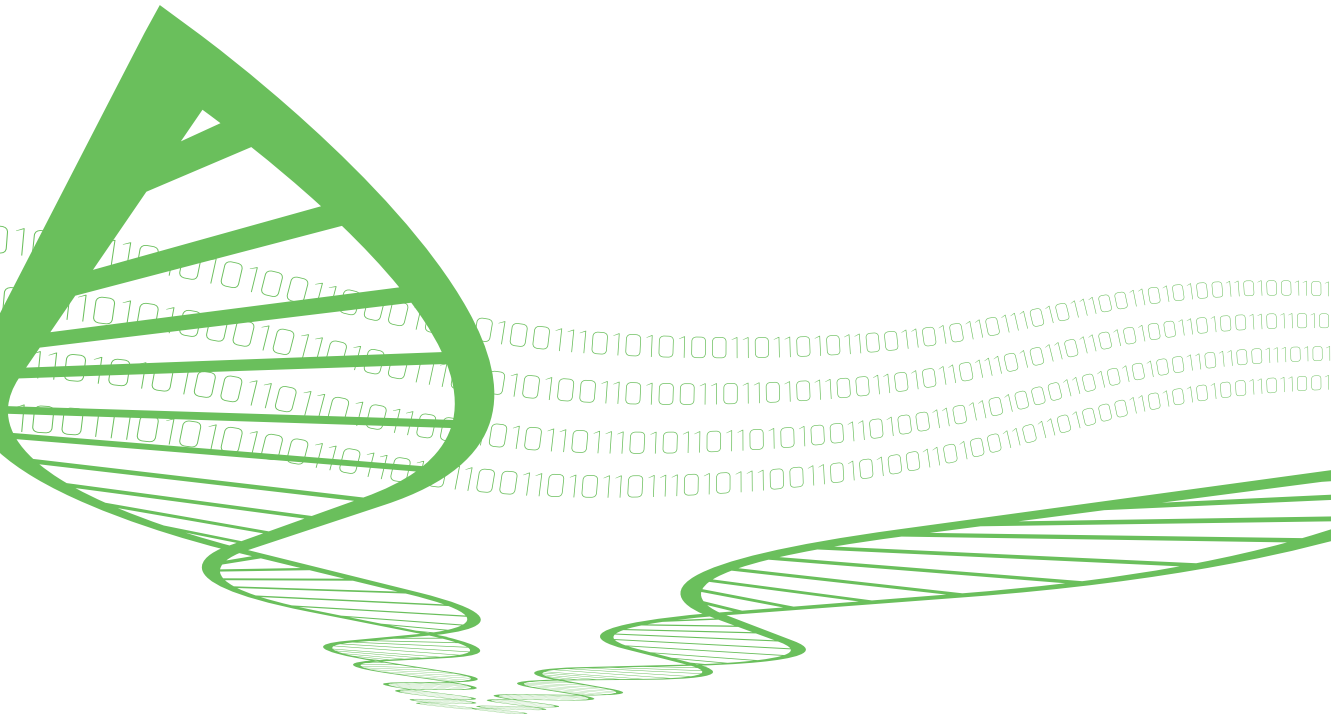

VTT SCIENCE 62

Polymeric slot waveguide interferometers

Marianne Hiltunen

Thesis for the degree of Doctor of Technology to be presented with due permission for public examination and criticism in OP-Sali (Auditorium L10), Linnanmaa, at the University of Oulu, on the 29th of August, at 12 o'clock noon.

ISBN 978-951-38-8271-6 (Soft back ed.)
ISBN 978-951-38-8272-3 (URL: http://www.vtt.fi/publications/index.jsp)

VTT Science 62

ISSN-L 2242-119X
ISSN 2242-119X (Print)
ISSN 2242-1203 (Online)

JULKAISIJA – UTGIVARE – PUBLISHER

VTT
PL 1000 (Tekniikantie 4 A, Espoo)
02044 VTT
Puh. 020 722 111, faksi 020 722 7001

VTT
PB 1000 (Teknikvägen 4 A, Esbo)
FI-02044 VTT
Tfn. +358 20 722 111, telefax +358 20 722 7001

VTT Technical Research Centre of Finland
P.O. Box 1000 (Tekniikantie 4 A, Espoo)
FI-02044 VTT, Finland
Tel. +358 20 722 111, fax +358 20 722 7001

Grano Oy, Kuopio 2014

Polymeric slot waveguide interferometers

Polymeeriset uravalokanavainterferometrit. **Marianne Hiltunen.**
Espoo 2014. VTT Science 62. 73 p. + app. 35 p.

Abstract

Slot waveguide is a specific light-guiding structure with a property to enhance the optical field in a nanometer scale void of low refractive index (RI) material embedded between higher RI material rails. Typically, slot waveguides have been fabricated from high refractive index inorganic dielectrics or semiconductors, such as silicon or silicon nitride, and they operate in the near infrared (NIR) wavelength region. The slot waveguide structure enables strong light–ambient interaction, a property that is preferred, for instance, in integrated optical sensors utilizing the change of the refractive index as the sensing transduction signal. In this thesis; the characteristic properties of slot waveguides were studied as regards their usage in polymer platforms.

The polymers are transparent in the visible and NIR wavelength region. In this work, the operation of the polymer slot waveguide was demonstrated for both visible and NIR wavelengths by using Young interferometer devices. For the device fabrication, the ultraviolet (UV) assisted nanoimprint moulding method was utilized. The emphasis was to demonstrate that the high performance slot waveguide sensor configuration is attainable with a simple low-cost fabrication method, enabling usage as disposable sensors.

The bulk refractive index (RI) response of the slot waveguide-based Young interferometer was characterized with glucose – deionized water solutions. With this arrangement, an ambient RI change of 6.4×10^{-6} was measured. In the slot Young interferometer structure, both waveguide arms of the interferometer detect the bulk RI changes of the ambient material. This novel structure was proved to effectively compensate for thermo-optic originated response drift while maintaining high sensitivity against bulk RI change.

Keywords Slot waveguide, polymer waveguide, nanoimprint moulding, Young interferometer

Polymeeriset uravalokanavainterferometrit

Polymeric slot waveguide interferometers. **Marianne Hiltunen.**
Espoo 2014. VTT Science 62. 73 s. + liitt. 35 s.

Tiivistelmä

Uravalokanavarakenteessa optinen kenttä on vahvistunut nanometrien levyisessä matalataitekertomisessa raossa, jota reunustavat kummaltakin puolelta korkeataitekertomiset harjanteet. Tyypillisesti uravalokanavarakenteet on valmistettu korkean taitekertoimen omaavista epäorgaanisista eristeistä tai puolijohteista, kuten piistä ja pii-nitridistä. Uravalokanava mahdollistaa voimakkaan valon ja materian vuorovaikutuksen. Tämä ominaisuus on erityisen tärkeä optisissa antureissa, joissa taitekertoimen muutosta hyödynnetään signaalin tunnistuksessa. Tässä työssä tutkitaan mahdollisuutta hyödyntää uravalokanavarakenteiden ominaisuuksia käytettäväksi polymeerialustalla.

Polymeerit läpäisevät valoa sekä näkyvän että lähi-infrapuna (NIR) aallonpituuden alueilla. Tässä työssä Youngin interferometrirakennetta hyödyntäen osoitettiin polymeeristen uravalokanavien toimivan näkyvällä ja NIR-aallonpituudella. Näytteet valmistettiin UV-valotusta hyödyntävällä painatusmenetelmällä. Tarkoituksena oli osoittaa, että yksinkertaisilla ja edullisilla valmistusmenetelmillä voidaan tehdä herkkiä uravalokanaviin perustuvia anturirakenteita. Rakenteen valmistuskustannusten pienentäminen saattaa mahdollistaa kertakäyttöisten antureiden hyödyntämisen.

Uravalokanavaan perustuvan Youngin interferometrin taitekerroinvastetta mitattiin glukoosi- ja ionipoistetun veden liuoksilla. Mittauksilla pystyttiin havaitsemaan suuruudeltaan 6.4×10^{-6} oleva taitekerroinmuutos liuoksessa. Tässä työssä käytetyssä Youngin interferometrirakenteessa sekä anturoiva uravalokanavahaara että referenssivalokanava havaitsevat ympäristön taitekerroinmuutoksen. Tämän uudenlaisen anturirakenteen osoitettiin kompensoivan lämpötilan muutoksesta aiheutuvaa vasteen ryömintää, vaikka rakenne pysyikin samanaikaisesti herkkänä taitekertoimen muutokselle.

Avainsanat Uravalokanava, polymeerivalokanava, nanopainatus kuviointi, Young interferometri

Preface

The work covered by this thesis has been carried out at VTT Technical Research Centre of Finland during the years 2010–2014. The research was executed in the SA-Brafin project funded by the Academy of Finland and VTT.

I wish to thank my supervisors, Prof. Pentti Karioja (VTT) and Prof. Jyrki Lappalainen (University of Oulu) for their guidance, support and encouragement during the course of this research. Dr. Jürgen Mohr (Karlsruhe Institute of Technology) and Dr. Shyqyri Haxha (University of Bedfordshire) are greatly acknowledged for comprehensive peer-reviewing of the thesis manuscript. I appreciate researchers of my doctoral training follow-up group, Dr. Matti Kinnunen (UO), Dr. Katariina Rahkomaa-Tolonen and Dr. Terho Kololuoma (VTT) for their guidance.

I am grateful to the co-authors and co-workers for their expertise, fellowship and contribution to this work. I especially want to thank Sanna Aikio, Jarno Petäjä, Lauri Kurki, Jarkko Tuominen, Annukka Kokkonen, Teemu Alajoki, Risto Karjalainen, Jyrki Ollila (VTT), Meng Wang, Esa Heinonen and Jarkko Puustinen (University of Oulu). I would like to acknowledge Tuija Soininen for helping me to improve the visualization of the publications. I especially wish to emphasize the contribution of Petri Stenberg (University of Eastern Finland), who continuously provided me his expertise and helped me to attain the results of this work. Moreover, I would like to thank Prof. Pasi Vahimaa (University of Eastern Finland) for helping to generate the research project for this thesis.

I would like to acknowledge the financial support for the finalization of the thesis from Tauno Tönning Foundation.

Finally, I would like to thank my parents and parents-in-law for believing in me and supporting me. I would like to express my deepest love and gratitude to my husband Jussi, son Ilari and daughter Elise for their love, patience and encouragement. Furthermore, I thank Jussi for guiding and supporting me in this dissertation process.

Oulu June 2014

Marianne Hiltunen

Academic dissertation

Supervisors	Prof. Jyrki Lappalainen Department of Electrical and Information Engineering University of Oulu, 90014 Finland
	Prof. Pentti Karioja VTT Technical Research Centre of Finland P.O. Box 1100 FI-90570 Oulu, Finland
Reviewers	Dr. Shyqyri Haxha University of Bedfordshire University Square, Luton Bedfordshire UK, LU1 3JU
	Dr. Jürgen Mohr Karlsruhe Institute of Technology, Hermann-von-Helmholtz-Platz 76344 Eggenstein-Leopoldshafen, Germany
Opponent	Prof. Tapio Niemi Optoelectronic Research Centre Tampere University of Technology P.O. Box 692 FI-33101 Tampere, Finland

List of publications

This thesis is based on the following original papers, which are referred to in the text as I–IV. The papers are reproduced with kind permission of the publishers.

I Hiltunen, M., Hiltunen, J., Suutala, A.,Tuominen, J. and Karioja, P. Polymer based single and multislot waveguides. Proc SPIE 2011. Vol. 8068, pp. 806812-1-6.

II Hiltunen, M., Hiltunen, J., Stenberg, P., Petäjä, J., Heinonen, E., Vahimaa, P. and Karioja P. Polymeric slot waveguide at visible wavelength. Optics Letters 2012. Vol. 37, pp. 4449–4451.

III Hiltunen, M., Heinonen, E., Hiltunen, J., Puustinen, J., Lappalainen, J. and Karioja, P. Nanoimprint fabrication of slot waveguides. Photonics Journal 2013. Vol. 5, No. 2, pp. 2200808.

IV Hiltunen, M., Hiltunen, J., Stenberg, P., Aikio, S., Kurki, L., Vahimaa, P. and Karioja, P. Polymeric slot waveguide interferometer for sensor application. Optics Express 2014. Vol. 22, pp. 7229–7237.

Other publications of the author related to this work, but not included in the thesis:

Fegadolli, W. S., Lira, H., L., R., Hiltunen, M., Karioja, P., Almeida and Scherer, A. Athermal silicon slot waveguide with an Ormocomp polymer overlayer. IEEE Photonics technology letters 2014. Vol. 26, pp. 1414-1417.

Hiltunen, J., Kokkonen, A., Puustinen, J., Hiltunen M. and Lappalainen, J. UV-imprinted single-mode waveguides with low loss at visible wavelength. IEEE Photonics technology letters 2013. Vol. 5, pp. 996–998.

Karvonen, L., Säynätjoki, A., Chen, Y., Tu, X., Liow, T.-Y., Hiltunen, J., Hiltunen, M., Lo G.-Q. and Honkanen, S. Low-Loss Multiple-Slot Waveguides Fabricated by Optical Lithography and Atomic Layer Deposition. IEEE Photonics Technology Letters 2012. Vol. 24, pp. 2074–2076.

Säynätjoki, A., Karvonen, L., Alasaarela, A., Tu, X., Liow, T. Y., Hiltunen, M. Tervonen, A., Lo, G. Q. and Honkanen, S. Low-loss silicon slot waveguides

and couplers fabricated with optical lithography and atomic layer deposition. Optics Express 2011. Vol. 19, pp. 26275–26282.

Hiltunen, J., Hiltunen, M., Puustinen J. and Karioja, P. Fabrication of optical waveguides by imprinting: Usage of positive tone resist as a mould for UV-curable polymer. Optics Express 2009. Vol. 17, pp. 22813–22822.

Hiltunen, M., Dal Negro, L., Feng, N.N, Kimerling, L. C. and Michel, J. Modeling of aperiodic fractal waveguide structures for multifrequency light transport. Journal of Lightwave Technology 2007. Vol. 25, pp. 1841–1847.

Author's contributions

The author of the thesis had a key role in the research work and was the main author of papers I–IV.

Paper I: "Polymer based single and multislot waveguides"

The author performed all the simulations and prepared the manuscript.

Paper II: "Polymeric slot waveguide at visible wavelength"

The author performed all the simulations and the main part of the fabrication processes, except the e-beam lithography. The device characterization, apart from SEM imaging, was performed by the author. The author prepared the manuscript.

Paper III: "Nanoimprint fabrication of slot waveguides"

The author performed all the simulations and contributed to the device fabrication by doing all the nanoimprint and negative tone lithography processes. The author characterized the devices, except for the SEM imaging and AFM measurement.

Paper IV: "Polymeric slot waveguide interferometer for sensor application"

The author conducted the main part of the fabrication processes, except the e-beam lithography. The device characterization, apart from SEM imaging, was mainly performed by the author. The author prepared the manuscript.

Contents

List of abbreviations

AFM	Atomic force microscope
BHF	Buffered hydrofluoric acid
BMP	Beam propagation method
CMOS	Complementary metal oxide semiconductor
CNP	Combined nanoimprint photolithography
DI	Deionized water
DUV	Deep ultraviolet
E	Electric
e-beam	Electron-beam
EME	Eigenmode expansion method
FDM	Finite difference method
FDTD	Finite-difference time-domain method
FEM	Finite element method
FFT	Fast Fourier transform
FIB	Focused ion beam
GaAs	Gallium arsenide
HBr	Hydrogen bromide
HSQ	Hydrogen silsesquioxane
ICP-RIE	Inductive coupled plasma-reactive ion etching
IO	Integrated optic
LOD	Limit of detection
NaOH	Sodium hydroxide

NIL	Nanoimprint
NIR	Near infrared
OIC	Optical integrated circuit
PM	Polarization maintaining
PMMA	Poly(methyl methacrylate)
RI	refractive index
RIU	Refractive index unit
RPM	Revolutions per minute
SEM	Scanning electron microscope
Si	Silicon
Si_3N_4	Silicon nitride
SiO_2	Silicon oxide
SOI	Silicon on insulator
TE	transverse electric
TiO_2	Titanium dioxin
TOC	Thermo-optic coefficient
TM	Transverse magnetic
UV	Ultraviolet
VIS	Visible
YI	Young interferometer

List of symbols

β, β_j	Propagation constant
c	Free-space speed of light
d	Distance between the waveguide arms
δ	Phase difference
$\Delta\varphi$	Phase difference between the sensing and reference waveguide arm
Δn_B	Change of bulk refractive index
Δn_{eff}	Effective index difference
Δs	Optical path length difference
E, E	Electric field
E_x, E_y	Electric field x- and y- direction
ε	Dielectric tensor
ε_0	Free-space dielectric permittivity
f	Distance of the detector from the waveguide output facet
f_S	Filling factor
H	Magnetic field
h_R	Residual layer thickness
I_1, I_2	Intensities of beams
$\boldsymbol{J}$	Current density
k_0	Wavenumber in vacuum
k_x,k_z	Wavenumber in the x- and z- directions
λ, λ_0	Wavelength of light, wavelength of light in vacuum
L	Length of the sensor

L	Litre
mol	mole
mol_g	Amount of glucose in moles
mol_{DI}	Amount of water in moles
μ_0	Free-space magnetic permeability
n	Refractive index
n_B	Bulk refractive index
n_{cl}, n_{co}	Refractive index of cladding, core
n_D, n_{GL}	Refractive index of DI water, glucose-water solution
n_{eff}	Effective refractive index
n_f, n_p	Refractive index of film, refractive index of prism
n_H, n_L	High refractive index, low refractive index
n_{su}	Refractive index of substrate
P_z(a)	Time averaged Poynting vector
θ	Angle of incidence with respect to the normal of the interface
θ_{cl}, θ_{su}	Critical angles of the rays
σ	Charge density
t	Time
ω	Angular frequency
W_R	Ridge width

1. Introduction

1.1 Integrated optics

Integrated optics is a technology field where the signals are carried and processed by an optical wave [1]. A typical optical integrated circuit (OIC) consists of a light source producing the optical signal, an optical waveguide devices transmitting and possibly processing the signal, and a detector converting the optical signal back to the electric domain. When the fabrication of all the active and passive components – source, waveguide, and detector – is carried out on a single substrate, the device is called a monolithic OIC. Monolithic OIC can be fabricated only from optically active materials. Another form of producing OIC is a hybrid technique, wherein devices fabricated from different material are somehow bonded together [2]. This approach enables single device fabrication utilizing ease and low-cost production techniques.

The applications for integrated optics are versatile. Primary OICs have been utilized in optical communication, imaging, signal processing, computing, instrumentation and sensing [3], [5]. The optical waveguide device, which is used to transmit the light from one point to another, simultaneously allows processing of the light propagation. This property has been utilized in passive waveguide devices, such as Bragg gratings and ring resonator filters, beam splitters and polarization controllers [6]–[9].

Data communication and sensor devices are the two main application fields utilizing optical waveguides. Typically, in data communication applications the transmitted light has been tightly guided inside the waveguide core, which enables compact device sizes, a tight bending radius and negligible light interaction with the ambient. However, in sensor applications, a strong light-ambient interaction is an advantageous property of the waveguide. Enhanced light-ambient interaction is one property of a unique waveguide geometry, namely slot waveguide, developed approximately ten years ago [10]. The characteristic property of slot waveguide is the ability to guide and confine the light in a narrow low refractive index material embedded between high refractive index materials. A great variety of photonic devices have been proposed or fabricated by exploiting slot waveguides, including microring and Fabry-Perot resonators [11], directional couplers [12] and polarization splitters [13]. They have been demonstrated for all-optical signal processing in

high-speed optical communication systems [14], [16]. Furthermore, slot waveguides have proved to effectively compensate the temperature dependency of integrated circuits [17]. One attractive application is realizing monolithic integration of the light source by exploiting properties of slot waveguide [18]. Slot waveguides have mainly been fabricated by utilizing CMOS-compatible material, such as silicon and Si_3N_4. Because silicon is not transparent in the visible wavelength region, the research has been focused on the near infrared (NIR) wavelengths. Although Si_3N_4 is transparent in the visible region, the demonstrated slot waveguide has still been working at NIR wavelengths.

1.2 Objective and outline of the thesis

A feature of confining light in a low refractive index material makes slot waveguide an attractive for sensing application, where a strong light-ambient interaction is required. Several sensors, mainly based on ring resonator geometry, have exploited slot waveguide configuration for enhancing the sensitivity compared to a regular ridge or strip waveguide [19]. The demonstrated bulk refractive sensitivity of slot ring resonator sensors have been in the order of 10^{-6} RIU at used NIR wavelengths [20]. In sensing applications, visible wavelengths are usually preferable. Visible wavelengths provide higher sensitivity and permit usage of both label-free and label-based sensing methods. Polymers are transparent at visible wavelengths; their surfaces can be functionalized and they are biocompatible, which makes them an attractive material option for sensor applications [21], [22].
Regeneration of the sensor between the analyses might be a very complicated procedure. To avoid regeneration of the sensor chip, the fabrication cost of the sensor should preferable be reduced in order to enable usage of disposable sensors. Therefore, an opportunity to apply simple and low-cost fabrication techniques makes polymers an attractive material in a sensor platform.

The objective of this thesis work was to demonstrate the operation of slot mode in a polymer waveguide. The operation of the slot waveguide-based interferometer was demonstrated both at visible and NIR wavelengths. The goal was to develop a high-performance sensor by increasing the light-ambient interaction by employing slot waveguide geometry in a Young interferometer. The fabrication process of slot waveguide sensors was developed based on nanoimprint moulding technique. This fabrication process potentially enables high volume, low-cost production of polymer sensors for aqueous environments.

Figure 1 gives an overview of the contents of this thesis, which is a combination of results presented in papers (I–IV). Paper I covers the theoretical study of polymer and composite polymer waveguide structures consisting of single and multiple slots. The first demonstration of slot waveguide mode at visible wavelengths has been presented in Paper II. Paper III shows the demonstration of polymer slot waveguide operation at 1305 nm NIR wavelength with the emphasis on device fabrication. The sensitivity analysis of the slot waveguide Young interferometer has been performed in Paper IV.

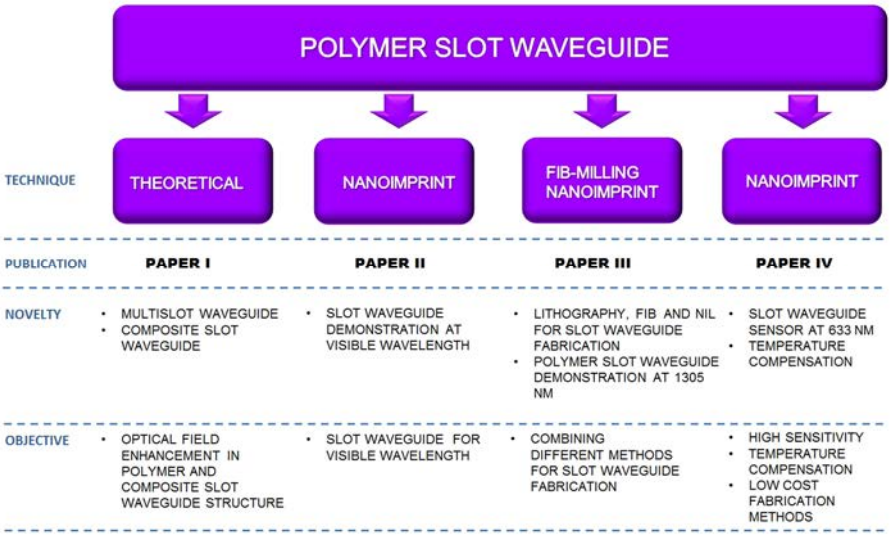

Figure 1. Overview of thesis content.

2. Optical waveguide

2.1 Principles of waveguiding

2.1.1 Ray optics

Light propagation in a waveguide can be described with the help of ray optics [23], [24]. Figure 2 illustrates the propagation of a coherent light beam in a two-dimensional

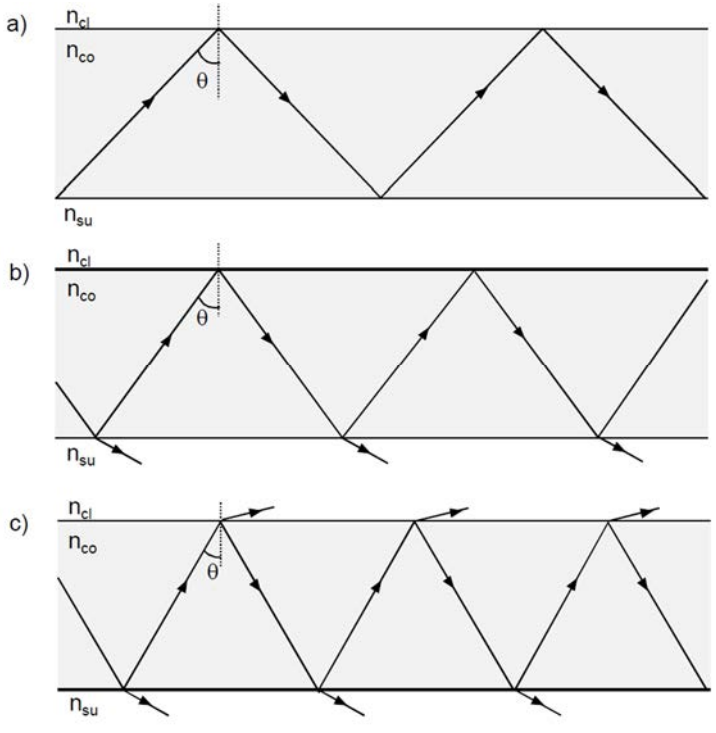

Figure 2. Propagation of a coherent light beam in a slab waveguide structure. a) Guided mode $\theta_{su} < \theta < 90°$, b) substrate radiation mode $\theta_{cl} < \theta < \theta_{su}$ and c) substrate-cladding radiation mode $\theta < \theta_{cl}$.

slab waveguide constructed from substrate, core and cladding, in which the refractive indices are $n_{cl} < n_{su} < n_{co}$. The incident light experiences the total internal refraction at the interfaces, if the angle of incidence θ with respect to the normal of the interface is larger than the critical angles in the core–cladding and core–substrate interfaces, respectively. These critical angles are defined as

$$\theta_{cl} = \sin^{-1}(n_{cl}/n_{co}) \tag{1}$$

$$\theta_{su} = \sin^{-1}(n_{su}/n_{co}). \tag{2}$$

Generally, $n_{su} > n_{cl}$ which leads to $\theta_{su} > \theta_{cl}$. For the angle of incidence $\theta_{su} < \theta < 90°$, the light is confined in the waveguide core and propagates along a zig-zag path, as presented in Figure 2 a). If the core material is lossless, light can propagate as a guided mode without any attenuation along the slab. Figure 2b) illustrates the propagation of light for the angle of incidences $\theta_{cl} < \theta < \theta_{su}$, where the light experiences the total internal reflection only at the core–cladding interface and it refracts into the substrate. The light propagates as a substrate radiation mode, and its amplitude decreases significantly along the propagation direction. The light refracts in both substrate and cladding in a radiation mode for the $\theta < \theta_{cl}$ (Figure 2 c).

In the guided wave, the modes are characterised by their propagation constants, which takes account of both the total internal reflection and the phase shift at the interfaces. The wave-vector diagram of the plane wave propagation constant is shown in Figure 3. The angle of incidence and the propagation constants along the x- and z- direction have relationships.

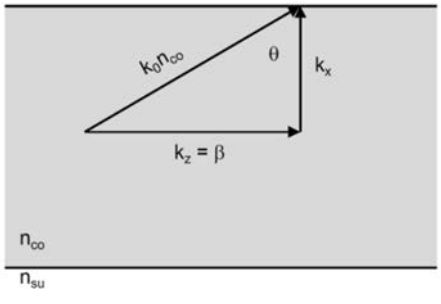

Figure 3. Wave-vector diagram in slab waveguide.

$$k_x = k_0 n_{co} cos\theta \tag{3}$$

$$k_z = k_0 n_{co} sin\theta = \beta, \tag{4}$$

where $k_0 = 2\pi/\lambda_0$ and λ_0 is the wavelength of light in a vacuum. The waveguide supports propagation of either one mode or multiple modes having a propagation constant β_j, which lies between

$$n_{su} k_0 < \beta_j \leq n_{co} k_0. \tag{5}$$

For each mode, an effective index can be defined as

$$\beta = k_0 n_{eff}, \quad \text{or} \quad n_{eff} = n_{co} sin\theta. \tag{6}$$

The effective indices of the guided waveguide modes are in the range

$$n_{su} < n_{eff} < n_{co}. \tag{7}$$

This can be determined by taking account of the acceptance angle of incidence $\theta_{su} < \theta < 90°$ for guided mode. The radiating modes have an effective index $n_{eff} < n_{su}$.

2.1.2 Wave equations

As described in the previous paragraph, the modes can be classified based on ray optics. The optical waves in the waveguide, where the refractive index profile along the propagation axis is invariant, are transmitted with constant spatial field distribution, propagation constant β and polarization, which they maintain at all distances along the waveguide. The spatial dependency of an electromagnetic field of an optical waveguide can be determined by Maxwell's equations. It is assumed, that field vectors time dependency is $exp(-i\omega t)$, current density J and charge density σ. The dielectric constant is related to the refractive index by $\varepsilon = n^2\varepsilon_0$. The Maxwell equations are expressed in the form

$$\nabla \times \mathbf{E} = i(\mu_0/\varepsilon_0)^{1/2} k_0 \mathbf{H}; \qquad \nabla \times \mathbf{H} = \mathbf{J} - i(\varepsilon_0/\mu_0)^{1/2} k_0 n^2 \mathbf{E} \tag{8}$$

$$\nabla \cdot (n^2\mathbf{E}) = \sigma/\varepsilon_0 \; ; \qquad \boldsymbol{\nabla} \cdot \mathbf{H} = 0 \tag{9}$$

where ε_0 and μ_0 are the dielectric permittivity and magnetic permeability in the free space, n is the refractive index, $k_0 = 2\pi/\lambda_0$ is a free space wavenumber, λ_0 is a wavelength of light in the vacuum [25]. In the regions free of charges and current, the boundary conditions are satisfied across interfaces of different materials when the magnetic field and the tangential component of the electric field are continuous. Moreover, the normal component of the dielectric displacement vector $\varepsilon_0 n^2 E$ have to be continuous [25], [26].

2.1.3 Polarization

In the waveguide applications, the polarization state of the propagating mode usually has to be known. Polarization of light is determined by the direction of the electric field in time. The paraxial electric-field vector propagates sinusoidal with different amplitude and phase at each vector position. When the waves are approximately transverse electromagnetic to the optical axis (z-axis) and the electric field lies in the transverse plane (x-y-plane), the wave is said to be elliptically polarized. The polarization state of the wave depends on the ratio of the magnitudes between x- and y-components, and the phase difference of the x- and y-components. When the magnitude ratio is one and the phase difference is $\pm\pi/2$, the light is circularly polarized. The light is linearly polarized if the magnitude of the x- or y-component is zero, or if the phase difference between x- and y-components is either 0 or π.

The waveguide modes, having an electric field transverse to the optical axis and parallel to the surface, are called transverse electric TE-modes. When the magnetic field is transverse to the optical axis, the mode is called transverse magnetic TM-mode. Figure 4 shows the field direction of TE and TM modes in planar waveguide.

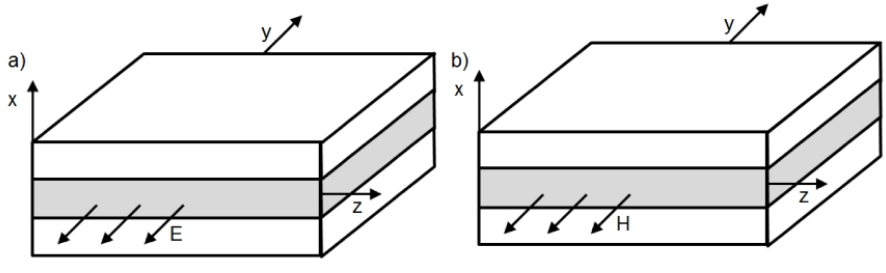

Figure 4. a) TE and b) TM modes in a slab waveguide.

The polarization state of the light coming from free space can be altered with different devices. The quarter wave plate is used to convert linearly polarized light into circularly polarized light or vice versa. The operation of the quarter wave plate consists in retarding of the y-component by the phase $\pi/2$. The quarter wave plate is wavelength-dependent. In the dichroic polarizer, the absorption of the light depends on the direction of the electric field. The light transmitted through a dichroic polarizer is linearly polarized. When the light is coming from the fibre-coupled laser source, fibre optic polarization controllers are used. The fibre optic polarization controller utilizes stress-induced birefringence in three fibre spools in order to create independent wave plates for altering the polarization state. The polarization conversion is achieved with retardation of the component phase by manually adjusting rotation of the fibre spools.

2.2 Waveguide mode simulation methods

The waveguide modes in complex waveguide structures can be solved with various computational methods. The finite difference method (FDM) [27], the finite-difference time-domain method (FDTD) [28], the film-mode matching method (FMM) [29] and the finite-element method (FEM) [30] are commonly used methods to solve waveguide modes. When modelling the unbound waveguide geometries, the artificial boundary elements at the computational domain have to be included. Commonly used approach with FDTD method is perfectly matched layer boundary condition, where the computational domain is surrounded by thickness of artificial conductor with graded electric and magnetic conductivity [31]. In this thesis work, the mode field simulations have been performed using FEM method available in commercial Fimmwave and Fimmprop software package of Photon Design Inc. [32]. The FEM divides the calculation area into the triangular meshes and is, therefore, a particularly suitable method for calculating modes in angled wall waveguides. With the FEM method used here, the perfect electric conductor boundary condition was applied at vertical artificial elements of the computational domain. This means that the tangential component of the electric field vanishes at the artificial vertical domain surface. Perfect magnetic conductor boundary condition is applied on the horizontal surfaces of the domain, which causes vanishing of the tangential component of the magnetic field in the boundary element [33].

The optical transmission along the waveguide can be modelled, for instance, with the FDTD method, beam propagation method (BPM) [34] or eigenmode expansion method (EME) [35]. The EME, used in this thesis work, solves the Maxwell equations for the given waveguide structure in terms of forward and backward propagating local modes. The optical transmission can be calculated by cascading the scattering matrix elements only at the interfaces of different subunits.

2.3 Waveguide geometries

The simplest waveguiding structure is a slab waveguide as illustrated in Figure 5 a). It consists of parallel planar layers, which are infinite in lateral directions. This kind of waveguide structure is not very practical in many applications, since the light is confined only in vertical direction. In order to confine the light in two directions, several other geometries are exploited. These useful structures are illustrated in Figures 5 b)–f), in which the darker colour expresses the higher refractive index. In the strip waveguide, Figure 5 b), the light is confined in the strip of higher RI material than the substrate and overcladding. The light is confined laterally by including a locally higher volume of core material in a vertical direction in a ridge (Figure 5 c), and an inverted ridge (Figure 5 d) waveguide geometry. In these two geometries, the height and the width of the ridge together with the slab thickness and the refractive indices determine the shapes and the number of guiding modes. In silicon photonic applications, a strip and a ridge waveguides are usually exploited. A ridge or inverted ridge geometries are commonly used for polymer waveguides [36], [37]. The effective index in the high RI slab layer is locally higher under a lower RI strip than in the adjacent regions in a strip-loaded waveguide structure (Figure 5 e). Strip-loaded waveguides have been fabricated, for instance, from GaAs [38]. In the slot waveguide geometry, the light is confined in the low RI material between the higher RI rails. The slot waveguide (Figure 5 f) geometry is discussed in detail in paragraphs that follow.

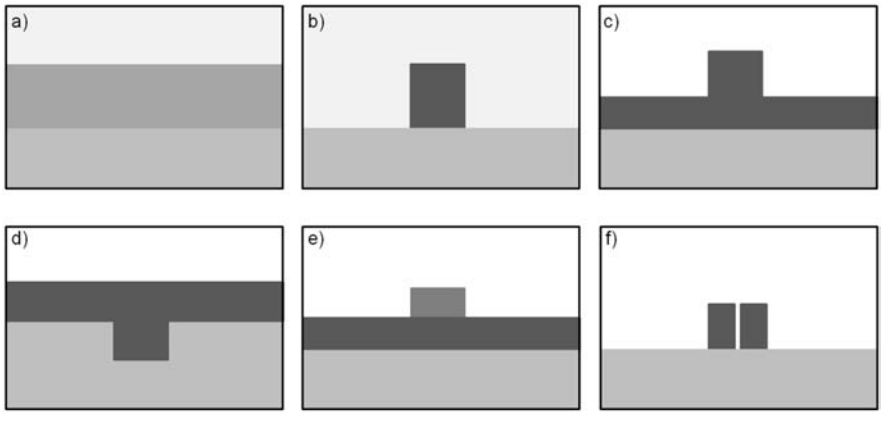

Figure 5. Cross-section image of different waveguide geometries a) slab waveguide; b) strip waveguide; c) ridge waveguide; d) inverted ridge waveguide; e) strip-loaded waveguide; f) slot waveguide.

2.4 Slot waveguide

The slot waveguide configuration was originally presented by Almeida *et al.* [10]. The slot waveguide structure simultaneously guides, enhances and confines the light in the low refractive index region embedded between high refractive index horizontal slabs or vertical strips [39], [42]. The principle of the slab-based slot waveguide structure is illustrated in Figure 6 a). It consists of a low RI (n_L) SiO_2 layer sandwiched between high RI (n_H) silicon layers. To satisfy the boundary conditions of the Maxwell equations in the high RI contrast interface, the surface normal component of the electric flux density has to be continuous at the boundaries. Therefore, the corresponding *E* field in the slot, have to undergo a large discontinuity at the interface with the higher amplitude in the low RI material. When the thickness of the low RI layer is much smaller than the field decay length, the *E*-field remains high across the slot. The *E*-field immediately inside the low RI slot is enhanced by the factor of n_H^2/n_L^2 respect to the *E*-field immediately inside the high RI slab. In the fundamental TM mode of the slab-based slot waveguide, the main electric field E_x is orientated normal to the interfaces. The E_x field distributions of slab slot waveguide structure, with 200 nm thick Si layers and with varying thicknesses of SiO_2 slot layers, are shown in Figure 6 b). A large discontinuity of the E_x field occurs in the slab-slot interface, and the field is enhanced in the low RI slot region. The field enhancement decreases as the SiO_2 slot layer becomes thicker. In the fundamental TE mode of slab slot structure, the main electric field E_y is orientated parallel to the slabs and, therefore, the discontinuity of the electric field does not occur as shown in Figure 6 c). Although, the E_y field is not enhanced in the slot region, the field remains high in a thin low RI layer.

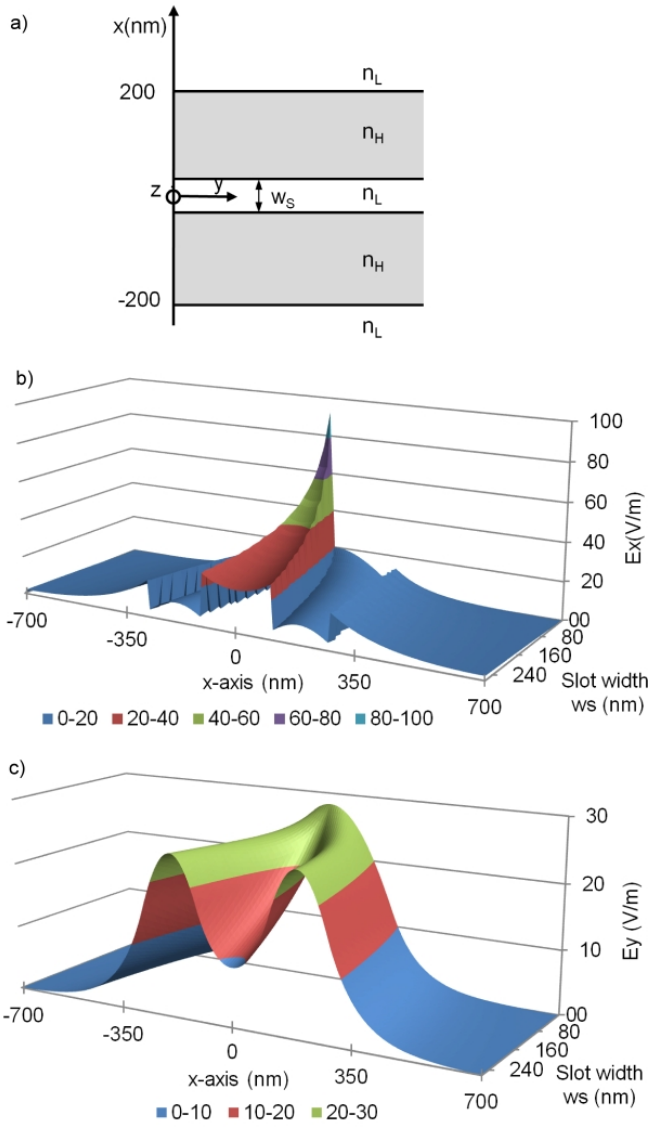

Figure 6. a) Slab slot waveguide configuration. b) Horizontal cross-section plots of the main electric fields in Si – SiO_2 – Si slab structure, with constant 200 nm Si thickness and varying SiO_2 slot layer width, calculated for TM mode (E_x) and c) TE mode (E_y).

2.4.1 High refractive index contrast slot waveguide

Most of the research on the slot waveguides has been concentrated on high refractive index materials, such as silicon and silicon nitride [39], [42], [43]. In a slot waveguide consisting of a high RI strips, the TE mode exhibit a strong field enhancement in the slot region. The electric field distribution of different SOI waveguide structures are compared in order to indicate the influence of each waveguide geometry producing a slot mode. The electric field distribution of the fundamental TE modes of these waveguide geometries are calculated at 1550 nm wavelength.

A cross-section images of different waveguide geometries employed for the comparison are illustrated inside dot dashed boxes in Figure 7 a). A green and a red box on the left dot dashed box represents an individual Si strip with a width of 200 nm and height of 300 nm. The vertical cross-sections of transverse electric E_x field at the middle of a single left strip (green box) or single right strip (red box) are plotted in the Figure 7 b) as a green and red curve, respectively. The values are normalized with the maximum E_x. The slot waveguide geometry is illustrated with blue boxes in the middle dot dashed box of Figure 7 a). The slot width of 50 nm is much smaller than the decay length of the electric field outside the single strips. The vertical cross-section plot of E_x field in the slot waveguide, indicated as a blue line in Figure 7 c), shows discontinuity of the E_x field in the Si - SiO_2 interface and a strong field enhancement in the slot. The conventional Si strip waveguide is illustrated with a black box in the right dot dashed box of Figure 7 a). The black line in Figure 7c) is the vertical cross-section plot of the E_x field in the strip waveguide. It shows that the E_x field locates mostly in the high refractive index Si strip.

The fundamental TE and TM modes were calculated for the slot waveguide geometry shown in the middle of Figure 7 a). The main electric field distributions of the fundamental TE mode and TM modes at 1550 nm wavelength are shown in Figure 8. The maximum of the electric field (E_x) locates in the slot at TE mode, whereas in the TM mode, the maximum of the electric field (E_y) locates both on the top and in the bottom of silicon strips. A higher fraction of the optical field locates in the SiO_2 slot at TE polarization state than at TM polarization state. This causes a high birefringence, i.e. effective index difference between two polarization states, in the slot waveguide structure. For the previous slot waveguide geometry, the effective refractive indices of TE and TM mode are 1.931 and 2.072, respectively.

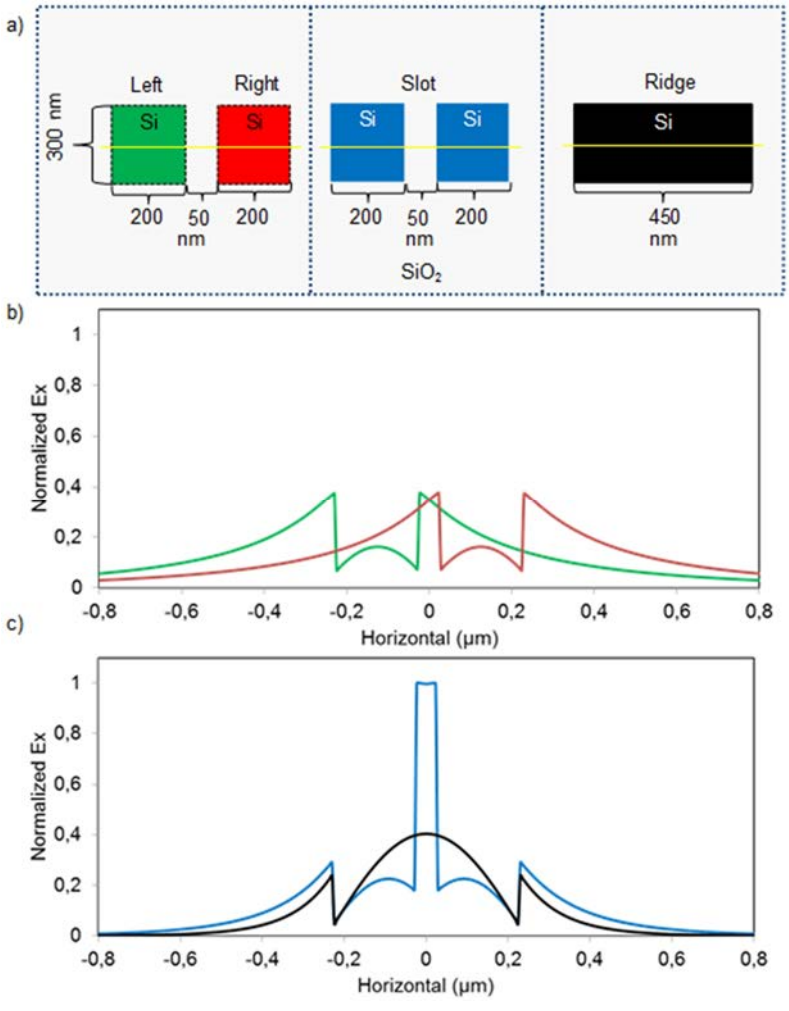

Figure 7. a) Schematics of different SOI waveguide geometries illustrated in separate dot dashed boxes. The yellow line indicates the position of vertical cross section of normalized electric fields (E_x) plotted in b) and c). The green plot was calculated for a single Si strip on the left (green box) and the red plot for a single Si strip on right (red box) in the left dot dashed box. c) Blue line was calculated for a slot waveguide in the middle dot dashed box and the black line for a strip waveguide on the right dot dashed box.

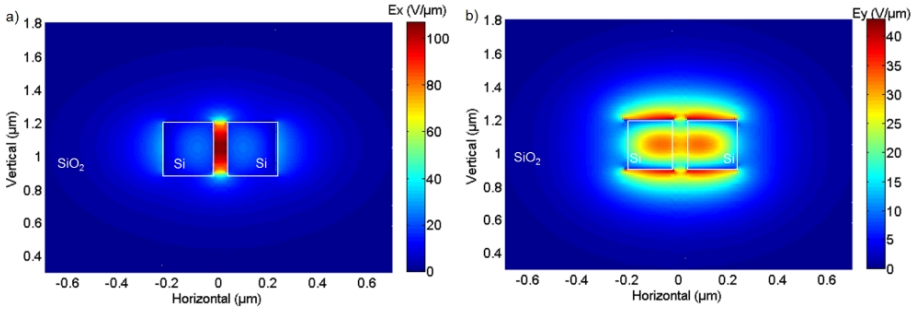

Figure 8. a) The electric field (E_x) distribution of the fundamental TE mode and b) the electric field (E_y) distribution of the fundamental TM mode in SOI slot waveguide.

The field enhancement in the slot waveguide comes from the boundary conditions of the Maxwell equations, which states that the tangential component of the electric field is continuous across the interfaces. The main electric field of TE mode is orientated normal to the high refractive index contrast interfaces, and to fulfil the boundary conditions it experiences a large discontinuity at these interfaces. This causes a formation of enhanced and confined intensity in the slot region for TE mode. Since the main electric field component of TM mode is parallel to the high RI contrast interfaces, a similar field enhancement effect does not occur for TM mode. However, a significant fraction of the light is still guided in the slot with the TM mode.

The width of the low RI void has to be below the decay length of the mode field inside the slot. Therefore, the slot widths in high RI contrast waveguides, such as, Si/SiO_2, are in 100 nm regime setting tight tolerances to the fabrication. The fabrication constraints can be relieved, when the slot width is increased by decreasing the RI contrast or partial filling of the slot with thin film coating [44].

Electron-beam (e-beam) lithography and deep ultraviolet (DUV) processes are typically used to fabricate vertically etched slot waveguides in high RI contrast materials [30], [39], [42], [45], [46]. Horizontal slot waveguide structures, where the low RI material is sandwiched between high RI layers, have been fabricated by thin film deposition technologies [40]. The feature of confining light in low refractive index material enables several applications, for instance, optical trapping, all-optical switching and sensing [47], [49]. Slot waveguide geometry has been utilized for controlling the temperature dependency of resonator devices [17], [50], [51]. The capacity of having a giant birefringence, has been exploited in polarization splitter devices [13], [52]. Furthermore, horizontal slot waveguide geometry has recently been realized as monolithic integrated light emitter in a silicon photonic circuit [18].

2.4.2 Polymeric slot waveguide

Low RI contrast slot waveguide realized from polymers has several advantages, especially in sensor applications. Particularly, transparency of polymers in visible wavelength range is a preferred property for sensor applications. Bio-sensing analysis is often performed in an aqueous environment. The water absorption in the visible range is more than a thousand times less than at NIR wavelength [53]. Moreover, operation at visible wavelength provides higher sensitivity and permits the use of fluorescent markers in label-based sensing methods. The polymers are biocompatible, and their surfaces can be functionalized [54], [55]. One main advantage of choosing polymer for slot waveguide structure is a potential of employing simple low-cost fabrication methods, such as nanoimprint moulding.

Figures 9 a) and b) show the main electric field distribution in the polymer slot waveguide calculated at 633 nm wavelength for TE and TM polarizations, respectively. The substrate of Ormocore (commercial optical polymer by Micro Resist Technology GmbH) polymer slot waveguide was SiO_2, and the cladding was water. As seen in Figure 9 a), the electric field (E_x) of TE mode is enhanced and confined in the slot region. The vertical cross section plot of the E_x field for different slot widths of fundamental TE modes are shown in Figure 9 c). Also, a percentage proportion of the modes optical field intensity locating in the slot region for each slot width is presented in Figures 9 c) and d). The electric field (E_y) of TM mode also propagates in the slot region, but regardless of how narrow the slot is, the field does not enhance. However, the percentage proportion of the optical field intensity in the slot region is almost the same with both TE and TM mode.

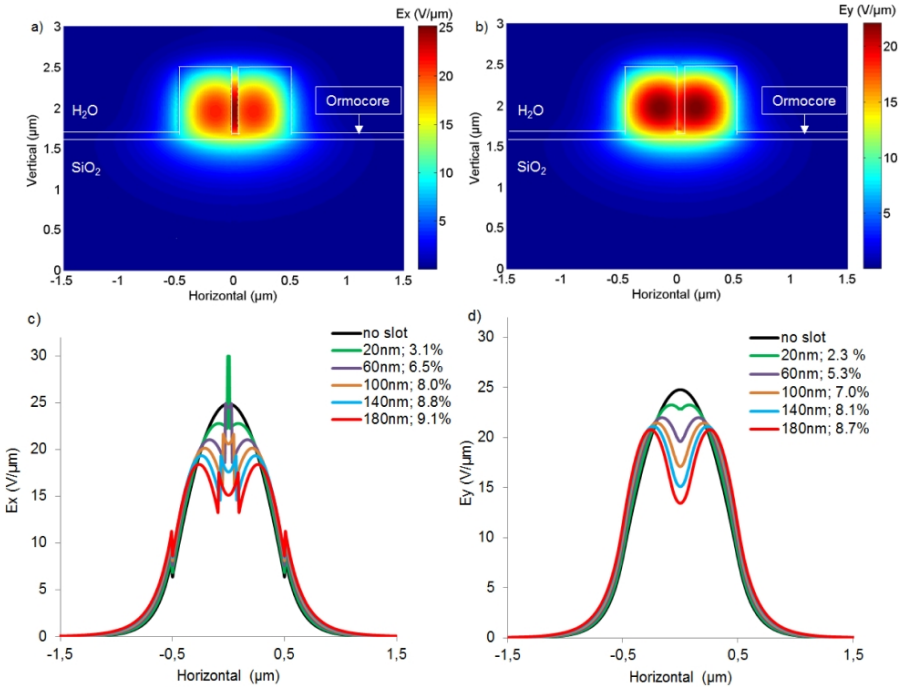

Figure 9. The main electric field distribution of a) fundamental TE mode (E_x) and b) fundamental TM mode (E_y) in polymer slot waveguides. The vertical cross section plot of the electric field at the middle of the waveguide calculated for various slot widths for c) TE mode and d) TM mode. The percentage fractions of the optical field intensity in the slot region are shown next to the slot width.

The disadvantage of the polymer slot waveguide is the lower field enhancement compared to high RI contrast slot waveguides. This is due to the lower refractive index contrast between the materials of the waveguide core and the slot. However, the RI contrast in polymer slot waveguide can be increased with a composite structure proposed in Paper I. Thin high RI coatings, for instance TiO_2, on the top of the polymer waveguide pushes the optical field more into the slot region, and therefore enhances the light matter interaction in the slot waveguide [56]. The enhanced light matter interaction due to the high refractive index coating on polymer waveguide has been on demonstrated in [54]. A theoretical study of high refractive index coating on the polymer slot waveguide is discussed in paragraph 5.1.

2.5 Integrated waveguide sensors

Integrated optical sensor detects perturbation of the evanescent field. This can be exploited to measure changes of the refractive index, absorbance or fluorescence properties of an analyte, and (bio)chemical activities. IO sensors possess several

advantages, such as immunity to the electromagnetic interference, high sensitivity, small size and possibility for real-time and multi-analyte detection [20], [57]. The optical biosensors can be divided into two classes. The first one uses the fluorescent markers for labelling the target analyte i.e. fluorescent-based detection. The other class is direct label-free optical detection. The fluorescent-based detection enables an extremely low detection limit, but it requires labelling pre-treatment of the sample. The label-free method is attractive in many cases, since the target molecules are detected in their natural form.

Several IO sensor devices, such as ring-resonators, grating structures, Mach-Zehnder and Young interferometers, have been demonstrated by utilizing evanescent field label-free techniques. Sensors based on surface plasmon resonance and slab Young interferometer configuration are already commercially available [58], [59]. Typically, the sensor detects the refractive index change of the ambient material. In the integrated devices, the small proportion of the optical field locates near the sensor surface, and the evanescent field, capable of detecting the RI, vanishes within the decay length characteristic of each device. The decay length varies from tens to a few hundreds of nanometers. Usually, IO sensors are fabricated from inorganic dielectrics, such as SOI or Si_3N_4, ion-diffused glasses and polymers. For each configuration, the geometry has to be carefully optimized in order to maximize the light-analyte interaction. The strength of light-analyte interaction determines the sensitivity of the device, i.e. magnitude of the transduction signal changes in response to the analyte variation. Another important parameter characterizing the sensor performance is the limit of detection (LOD), which takes also into account the noise of the transduction signal. Sensors detecting the bulk refractive index change have an LOD from 10^{-4} down to 10^{-9} refractive index unit (RIU) [60]–[65].

2.5.1 Young interferometer

In this thesis work, the Young interferometer sensor structure was utilized. A typical integrated Young interferometer is presented in Figure 10. The optical path length difference Δs of two output mode beams interfering at the position y on the detector is given by

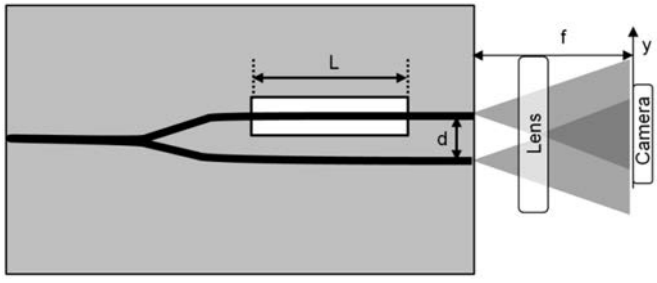

Figure 10. Schematic of integrated Young interferometer.

$$\Delta s = \frac{n_B d}{f} y, \tag{10}$$

where n_B is the bulk RI of the ambient material, d the distance between the output waveguide arms, and f the distance of the detector from the output facet of the interferometer. This equation is valid, when $f >> d$ [66]. The phase difference $\Delta\varphi$ between the mode beams at the interfering position is

$$\Delta\varphi = \frac{2\pi}{\lambda_0} \frac{n_B d}{f} y, \tag{11}$$

where λ_0 is the wavelength of light in a vacuum. The intensity distribution on the detector follows a cosine function. The intensity of the interferogram pattern can be described by the equation

$$I = I_1 + I_2 + 2\sqrt{I_1 I_2}\cos(\Delta\varphi - \delta) \tag{12}$$

where I_1 and I_2 are the intensities of two interfering waveguide beams and $\Delta\varphi$ is the phase difference of the beams [67]. When one of the waveguide arms detects the refractive index change at the length of L, an additional phase difference δ will occur. This additional difference can be calculated by the equation

$$\delta = 2\pi \frac{L}{\lambda_0} \Delta n_{eff}, \tag{13}$$

in which Δn_{eff} is the effective RI change of the fundamental mode as the RI of ambient material (n_B) changes [68].

Several aspects need to be taken into account, when designing the Young interferometer. Since the spatial shift of the interference pattern is measured, the short distance between two waveguide arms is advantageous. The camera does not have to be moved far, which enables readability of even a low intensity interference pattern. Also, when the waveguide arms are close to each other, the influence of temperature fluctuations is low. The sensitivity of the device is proportional to the length of the sensing window and the magnitude of the waveguides sensitivity coefficient. The sensitivity coefficient can be maximized by optimizing the waveguide structure to have large Δn_{eff} for small n_B change.

In this work, the designed slot waveguide operation was verified by measuring the phase shift between the arms of slot waveguide-based Young interferometer. The Young interferometer was designed to support only one mode for both the TE and TM polarization state. Simultaneously, the slot waveguide dimensions were optimized in order to have a large sensitivity coefficient in the sensing window. In the slot Young interferometer structure demonstrated, both waveguide arms of the interferometer detect the bulk RI changes of the ambient material. In some wave-

guide geometries, having large sensitivity, the higher order modes could theoretically propagate if the cladding was either air or water. The propagation of the high order mode was prevented by adding a polymer cladding layer on the input and output regions of the waveguide. The Y-branch and the interfaces of different waveguide sections are attributed to waveguide losses, which can be reduced by careful device design. The eigenmode expansion method (EME) was used to calculate the mode coupling loss in the cladding covered waveguide–uncovered waveguide interface and in the ridge waveguide–slot waveguide interfaces.

3. Fabrication methods

The principles of equipment operation and methods for enabling fabrication of the devices used in this thesis work are briefly introduced in this section. After each common introduction of the equipment, the methods utilized in this thesis are specified. It was intended to fabricate long waveguide devices, which include a slot of approximately 1 µm deep and 100 nm wide by nanoimprint moulding using the following tools.

3.1 Electron-beam lithography

Electron-beam lithography (e-beam) is a direct maskless patterning method, in which the electron sensitive resist is scanned with a focused beam of electrons to draw custom patterns on the surface. Depending on the type of resist, either exposed or un-exposed regions are removed with a developer.

The master mould for NIL process was fabricated with an e-beam process using Vistec's EBPG5000+ES HR equipment at the University of Eastern Finland. First, a silicon wafer was coated with a negative tone hydrogen silsesquioxane (HSQ) e-beam resist XR-1541 from Dow Corning ®, followed by the e-beam lithography to define the patterns. The acceleration voltage of the e-beam was 100 kV. Then the resist was developed in NaOH based Microposit 351 – water solution (1:3). The glazed resist was hardened by post baking at 300 °C for one hour. Once the patterns were transferred to the wafer, they were dry-etched for 6 minutes in HBr based ICP-RIE process. Finally, the HSQ resist was removed with BHF.

3.2 Focused Ion beam milling

The focused ion beam (FIB) equipment uses a highly focused beam of gallium ions for removing the sample material. FIB milling is a straightforward method to etch the patterns directly on the sample surface, without using a mask or resist. The milling depth depends on the material to be removed, beam acceleration voltage, ion current and irradiation time [69]. FEI Helios Dualbeam 600 FIB equipment, at the Center of Microscopy and Nanotechnology in the University of

Oulu, was used to mill the slot on the Ormocore master. The beam current during the milling was 28 pA and the beam voltage was 30 kV.

3.3 Photolithography

Photolithography is a fabrication process for transferring shapes on a photomask to the resist on the wafer. Usually the resist is spin-coated on the wafer. The mask layout used for the particular resist type, either positive tone or negative tone, determines the shape of the pattern. The UV-light exposed areas of the positive tone resist are removed in a developer. Negative tone resist behaves oppositely, and only the unexposed areas are removed during development.

Karl Suss MA6 Mask Aligner, at VTT Oulu, was utilized in all photolithography processes in this thesis work. The aligner is equipped with a mercury arc lamp with I-line (365 nm) filter. Both positive and negative tone lithography were carried out. For positive tone lithography, Ultra-I 123 resist (Microchem), and for negative tone lithography Ormostamp (Micro Resist Technology) was utilized.

3.4 Nanoimprint moulding

The nanoimprint method was introduced by Chou [70] by creating 25 nm vias and trenches on thermoplastic PMMA film. Nanoimprint moulding is a direct pattern transfer method, where the resolution is not limited by the diffraction or scattering from the substrate and resist interfaces. The method requires the use of a mould with predefined surface relief patterns and a suitable resist material, which can be deformed and hardened to preserve the replicated patterns. The resist material can be cured either thermally or by UV light. When the thermal nanoimprint method is employed, the polymerization is attained by raising the temperature above the glass transition temperature of the polymer. After the mould and polymer are cooled down below the glass transition temperature, the polymer can preserve the imprinted pattern. For the thermal imprint process, the substrate and mould need to be chosen carefully, in order to prevent a thermal mismatch during the heating–cooling process [71]. The thermal expansion mismatch can be avoided if the resist is cured with UV light, in a room temperature nanoimprint process. In this work a UV-assisted nanoimprint process is utilized.

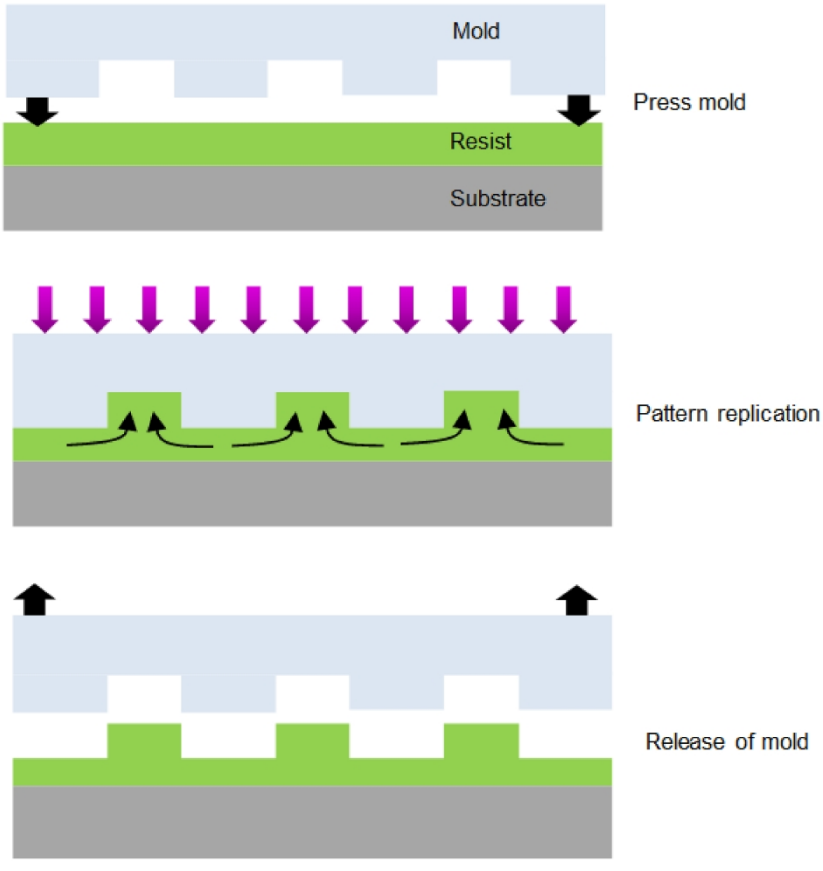

Figure 11. Fabrications steps during UV-based nanoimprint moulding.

In Figure 11, the schematic image of the UV-assisted nanoimprint process is presented. Either the mould or the substrate has to be transparent at the wavelength used for the exposure. The resist is spin- or dip-coated on the substrate, followed by pressing the mould against the resist. After the resist is cured by UV exposure, the mould is released from the replicated resist. When a large area surface is to be replicated, the mould release becomes one critical process step. Therefore, the resist has to exhibit strong adhesion to the substrate. In this work, inorganic-organic hybrid polymers ORMOCER® are used, which are commercialized by Micro Resist Technology GmbH. They offer a good adhesion to commonly used substrates, such as Si, SiO_2, glass and polymers. To allow easy mould-resist release, a low-surface-energy coating of (1,1,2,2 H perfluorodecyl)-trichlorosilane release agent is formed on the top of the mould by the vapour-phase reaction.

A thin residual layer of polymer remains under the replicated patterns, unless an additional etching process or combined nanoimprint-photolithography (CNP) process is applied [72]–[74]. The thickness of the residual layer can be adjusted

by adding solvent and therefore decreasing the viscosity of the resist. However, when a very thin layer of resist is used to fill high aspect ratio patterns on a large surface, an incomplete pattern replication might occur. Complete filling of the patterns with polymer flow can be ensured by adjusting the imprint time and pressure for each viscosity and thickness of the resist, and the required pattern aspect ratio.

The nanoimprint replication equipments are relatively cheap compared to the nanopatterning systems based on point-to-point stepping method, such as electron and ion beam equipment. The patterns can be replicated fast and repeatedly by NIL on large area several times with high quality. As a one-step process method, it doesn't require additional post processing phase, such as dry etching or solvent treatment. For above mentioned reasons, NIL enables simple, low-cost and high-throughput fabrication of nanostructures on a large area [71], [72].

In this work, both laboratory-customized imprinting set-up and commercial Obducat Eitre 6 nanoimprint equipment was utilized. The UV-expose wavelength was 365 nm with both equipment.

4. Characterization methods

This chapter presents the characterization methods utilized in this thesis.

4.1 Prism coupling method

The prism coupling method can be utilized to determinate the refractive index of the bulk substrate or slab film layer [75]. The principle of the prism coupling method is illustrated in Figure 12. When the RI of prism (n_p) is higher than the RI of film (n_f), total reflection of the incoming laser beam occurs at the bottom of the prism, and the intensity of the reflected light beam is detected with a photodetector. The sample is in contact with a coupling prism mounted on a rotating holder. The laser beam is directed on the rotating prism–sample holder, and the power of the reflected beam is monitored as a function of incident light angle. At a certain angle of incidence θ, the k_z component of the propagation constant of the beam in the prism matches the propagation constant of the film mode, and the light couples

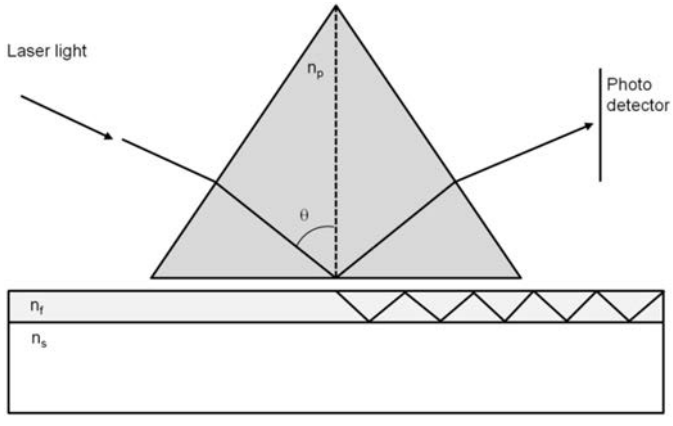

Figure 12. Schematic of prism coupling measurement.

into the film. The light coupling into the film can be detected as an intensity drop. The refractive index of the film material can be calculated by $n_f = n_p \sin\theta$, where the θ is the angle of incidence which causes abruptly intensity drop. When the film is thick enough for allowing the propagation of at least two modes, both the refractive index and the thickness of the film can be determined. If only one mode can propagate in the film, either the thickness or refractive index of the film can be determined, provided that the other parameter is known.

A Metricon 2000 prism coupler was used to measure the refractive index of Ormocore and Ormostamp at 1552 nm, 1320 nm and 633 nm wavelengths. For the measurements, a several micrometre-thick slab waveguide sample was prepared by spin coating polymer on glass wafer, followed by UV exposure and hard baking.

4.2 Scanning electron microscope

In the scanning electron microscope (SEM), the focused beam of electrons is scanned over the sample, and the electrons interacting with the atoms of the sample generate a secondary electron signal that is combined with the information of the beam's position so as to produce an image. SEM fitted in FEI Helios Dualbeam 600 FIB equipment at the Center of Microscopy and Nanotechnology in the University of Oulu, was used to characterize short slot waveguides. Platinum was deposited on the sample to improve the quality of the image. The long slot waveguides were characterized with SEM LEO 1550 Gemini at the University of Eastern Finland. A thin copper layer was sputtered on the sample in order to make it electrically conductive and therefore improve the quality of the image.

4.3 Atomic Force microscopy

An atomic force microscope (AFM) is based on the measurement of the deflection of a sharp tip on micron-sized cantilever as the tip scans across the sample surface. Veeco Dimension 3100 AFM, at the University of Oulu, was used to estimate the surface roughness of the slot waveguide. The tapping mode scan was used in characterization.

4.4 Waveguide transmission measurement

The waveguide loss is often measured with a cut-back technique. The devices in this thesis work include Y-branch, which allows the measurement of the loss in slot waveguide by exploiting other methods, presented in the paragraphs that follow.

Two different measurement arrangements were used in order to measure the transmission of the waveguides. Figure 13 a) sketches the fibre-optic measurement set-up, in which a pigtailed laser diode operating at either 1305 nm or 633 nm wavelength was used as a light source. The polarization state was adjusted

with fibre-optic polarization controller installed between the laser and the polarization maintaining (PM) tapered input fibre. The correct polarization state was verified with an external polarizer. The output fibre, identical to the input fibre, was connected to the optical power meter (Newport Dual-Channel power meter, Model 2836-C with universal fibre optic detector Model181-IS-1) enabling the reading of the light intensity. The input and output fibres were aligned optimally with the waveguide so as to produce maximum light coupling into the waveguide, and out from both Y-branch arms. The maximum power transmissions through the waveguide were measured, and these measured values were referenced with the fibre-to-fibre power transmission measurement. The light intensity was compared between the ridge and slot waveguide arms, in order to estimate or measure the loss in the slot waveguide. Since the lengths of the slot waveguides characterized with the fiber optic set-up are in 100 µm scale, the loss values could be determined only approximately.

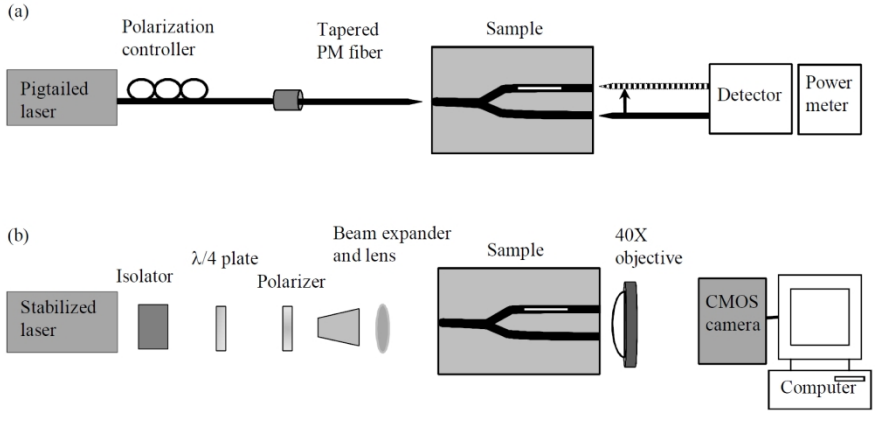

Figure 13. Schematic of the optical characterization methods. a) Fibre optics measurement set-up utilized in Papers II and III. b) Free-space light coupling measurement set-up utilized in Paper IV.

Figure 13 b) illustrates the waveguide transmission measurement arrangement, where the light was coupled into the sample from the free space. A wavelength stabilized laser operating at 633 nm wavelength was used as a light source. The optical isolator prevents the back-reflection of the light into the laser. A quarter-wave plate was used to convert the linearly polarized light of the source into the circularly polarized light, and the dichroic polarizer was used to control the polarization state of the light coupling into the waveguide. The correct polarization state was verified with an external polarizer. A beam expander and a lens were used for adjusting the input beam size and maximising the light coupling into the sample. The microscope objective collects and magnifies the images of the waveguide modes, and the images are captured with a CMOS camera. The loss in the slot waveguide can be deduced from the images of the normalized mode intensity pro-

files of the ridge waveguide arm and the ridge waveguide arm consisting of a slot part. The intensity deviation between the waveguide arms was obtained by comparing the output intensities of two identical waveguide arms (without a slot structure).

4.5 Young interferometer sensor measurement

Bulk refractive index measurement

The operation of the slot Young interferometer is based on the phase difference produced by two waveguide arms, one acting as a reference arm and another containing a slot section as a sensor arm. The slot determines the sensing length, in which the phase shift difference is produced. Two different methods to couple the light into the waveguide have been described in chapter 4.4 and schematically illustrated in Figure 13. The schematic image in Figure 14 illustrates the principle of the slot Young interferometer used in this work (Papers II, III and IV). When the light was coupled from the fibre into the waveguide (Figure 13 a), VIS-NIR camera (ElectroPhysics, MicronViewer Model 7290A) was used to video record the interference pattern. Microscope objective with 20X magnification, placed after the waveguides, was moved away from the focus of the waveguide output beams, in order to acquire the far field interference pattern with vertical parallel lines. The fibre coupling system was utilized for experimentally verifying the slot mode operation by recording the interferogram pattern shift, while a droplet of water was applied on the arms of Young interferometer (Papers II and III).

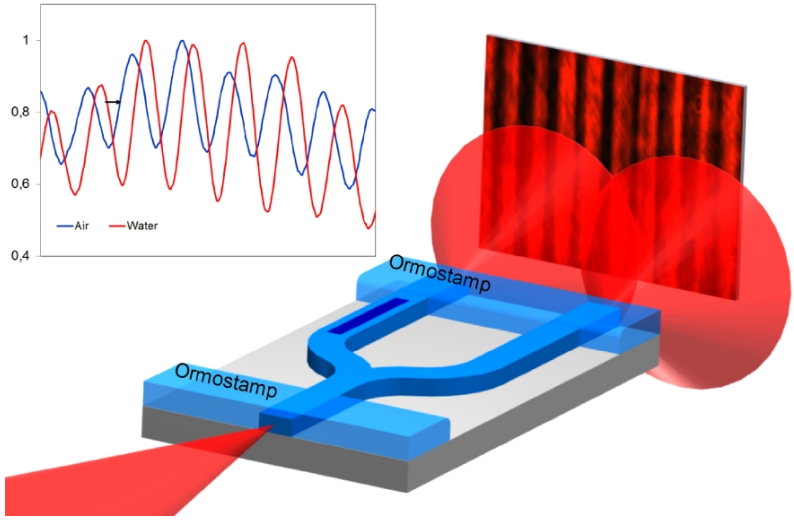

Figure 14. Schematic image of the slot Young interferometer and measurement set-up. The left arm includes a slot part, which produces the phase difference between the waveguide arms, and the right arm acts as a reference ridge waveguide. Insets shows the shift of interference pattern plot, when the droplet of water is applied.

The free space coupling method was used as a light coupling method, when the sensitivity response against the change of bulk refractive index of the slot Young interferometer sensor was measured (Paper IV). Microscope objective of 40X magnification was moved 1.35 mm away from the waveguide facet focus in order to generate an interference fringe pattern and the patterns were recorded with a CMOS camera (Pixelink, Model PL-E425CU). So as to evaluate the response of the sensor against the change of bulk refractive index, the deionized water with various concentrations of glucose-water solutions was applied on the sensing window of the device. The liquids were applied on the sensor by pumping them through a flow cell using a syringe pump (Nexus 3000, Chemyx Inc.) at 250 µL/min flow velocity.

Temperature sensitivity measurement

The measurement set-up used to determine the response of the sensor against the temperature variation is shown in Figure 15. A laser diode controller with TEC mode, (ILX Lightwave) was used to control the Peltier element under the sample holder, and the temperature was verified with a 10 kΩ NTC thermistor glued next to the device. The device was glued on the sample holder. Still DI water standing on the sensor window, improved the readability of the interferogram during the measurement. To take into account mechanical drifts, the mode intensity profiles at the waveguide output facet were focused onto the camera. Then their displacement relative to the temperature change was recorded with the CMOS camera (Pixelink, Model PL-E425CU). Due to the thermal expansion of the device holder, the coupling of the light into the waveguide was lost at the edge of the tunable temperature region, limiting the maximum temperature variation to approximately 5 °C. The displacement of the mode intensity profiles at different temperatures comes from thermo-mechanical movements in the whole measurement system. In the phase response measurement, the microscope objective was moved away from the focus so as to generate the interference fringe pattern. The thermo-optic coefficients (TOC) of the waveguide materials and water cause additional movement of the interference fringe pattern. The fringe pattern at each temperature after stabilization was recorded. In order to remove the thermo-mechanical movement of the device, the displacement of the mass centre of the focused mode intensity profiles was extracted from the interference pattern displacement prior the phase shift calculation.

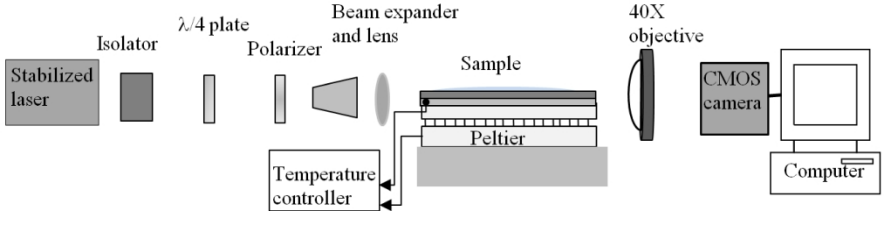

Figure 15. Measurement set-up utilized for temperature sensitivity characterization.

5. Results and discussion

In this thesis work, polymer slot waveguide structures were studied theoretically and experimentally. The theoretical study focused on establishing the characteristic slot mode properties in the polymeric material and designing the optimal structural dimensions that enable high light-matter interaction. The slot mode properties were established for near infrared and visible wavelengths. Theoretical studies were verified with experimental demonstrations by utilizing Young interferometer structure. Different methods for producing master moulds for the waveguide sample fabrication by replication methods were tested.

5.1 Theoretical modelling of polymer slot waveguide

5.1.1 Slot mode operation in polymeric waveguide

The light confining and the field enhancement in low RI material was originally established in an SOI-based slot waveguide at 1550 nm wavelength [10]. The same NIR wavelength was chosen, therefore, to show the slot mode properties in polymeric single and multiple slot waveguide structure in this work. The slot waveguide structure was also simulated for visible wavelength 633 nm.

The waveguide modes were calculated with commercial mode solver software, Fimmwave, using a finite element method (FEM). The filling factor of the mode in a slot region is defined as the fraction of optical mode flux f_S in the slot area by the equation

$$f_S = \frac{\int_S P_Z(a)da}{\int_\infty P_Z(a)da} \tag{14}$$

where $P_z(a)$ is the time averaged Poynting vector and the nominator is integral over the slot region S [76]. The dimensions were chosen in such a way that the highest possible f_S could be achieved while simultaneously maintaining a single mode operation with TE polarization state. The materials and the corresponding refractive indices used in the simulation for 1550 nm wavelength were the waveguide core Ormocore n = 1.538, glass substrate n = 1.45 and water cladding n = 1.33. The highest f_S for a single slot waveguide was calculated for the structure

parameters of polymer rail width of 1085 nm, rail height of 1300 nm, slot width of 330 nm, slot depth of 1500 nm, and a residual polymer layer of 200 nm. In this structure, 6% of the mode flux is located in the slot region. The mode intensity profile of TE mode in the single slot waveguide structure is shown in Figure 16 a). The cross section plots of transverse electric E_x field across the waveguide, shown in Figure 16 b), highlights that the electric field undergoes discontinuity at the slot interface. The mode flux was simulated to be 12% in the slot region of the triple slot waveguide structure, where three 330 nm wide slots were separated with 545 nm wide polymer rails. The mode intensity profile of this triple slot waveguide structure is shown in Figure 16 c), and the cross section plots of E_x field across the waveguide is shown in Figure 16 d).

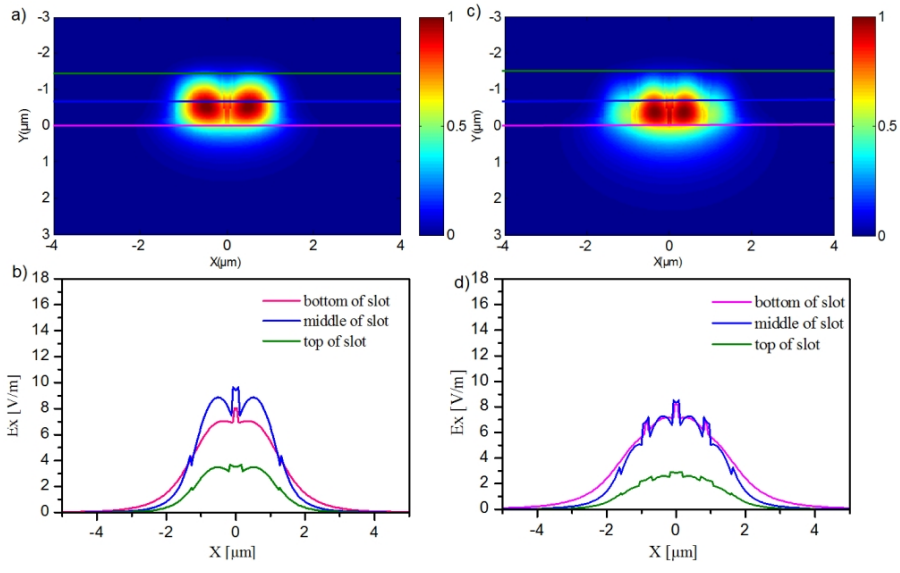

Figure 16. a) a) The intensity distribution of quasi-TE mode in a single slot waveguide with 1085 nm rail width and 330 nm slot width. The height of the rail is 1300 nm, and the depth of the slot is 1500 nm. b) The cross sections plots of the transverse electric Ex field of TE mode on the bottom, middle and the top of the slot in the single slot structure. c) The intensity distribution of quasi-TE mode in triple-slot waveguide with the 545 nm rail width and 330 nm slot width. d) The cross sections plots of the Ex field on the bottom, middle and the top of the slot in the triple-slot structure. (Paper I).

The increase of the electric field immediately inside the slot depends on the RI contrast between the slot and the rails. Therefore, in the composite slot waveguide structure, the impact of a 50 nm thick amorphous TiO_2 (n = 2.018) [77] coating on the top of polymer was evaluated as a factor in the field enhancement effect and the mode flux in the slot region. Figure 17 a) shows the TE-mode intensity distribu-

tion of TiO_2 covered slot structure, with a rail height of 1300 nm, rail widths 585 nm and a slot width of 230 nm. Although the slot is 100 nm narrower in the composite slot waveguide than in a fully polymeric slot waveguide, the mode flux is increased to the value of 7%. A large discontinuity effect at the slot interface and high enhancement inside the slot is shown in the cross section plots in Figure 17 b). Figure 17 c) shows the simulated mode profile of the TiO_2 covered triple slot waveguide structure, where the middle slot of width 230 nm is reciprocally surrounded with 100 nm wide middle rails, and with side slots of width 230 nm bounded with outer rails of width 500 nm. The mode flux in the slot regions of this structure is 15%. The cross section plots in Figure 17 d) of the E_x field across the triple slot structure shows discontinuity of the electric field at the high RI contrast interfaces and field enhancement in the slot region.

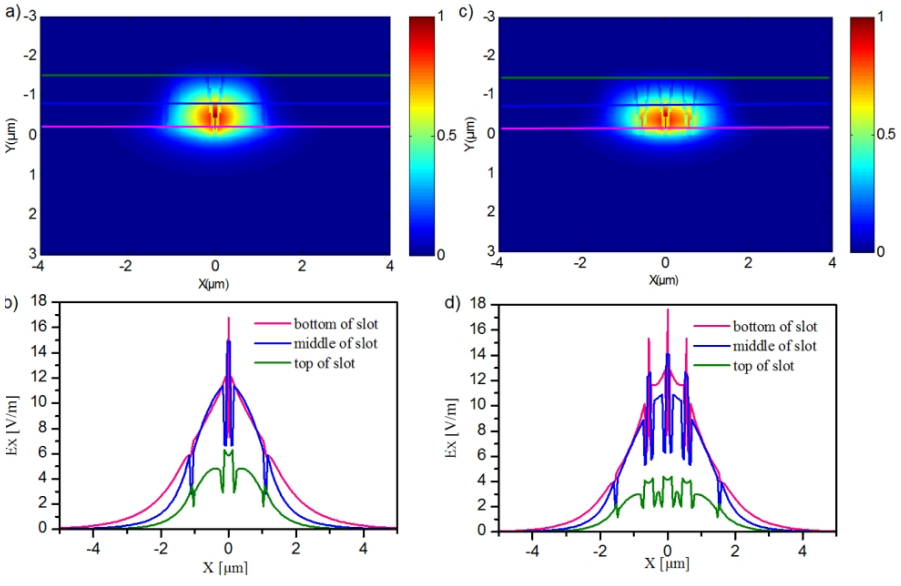

Figure 17. a) The intensity distribution of quasi-TE mode in a TiO_2 covered single slot waveguide with 585 nm rail width and 330 nm slot width. The height of the rail is 1300 nm and the depth of the slot is 1500 nm. b) A cross section plot of the *Ex* field on the bottom, middle and the top of the slot in the single slot structure. c) The intensity distribution of quasi-TE mode in a triple-slot waveguide with 500 nm side rail, 100 nm middle rail and 330 nm slot width. d) The cross section plots of the *Ex* fields on the bottom, middle and top of the slot in the triple-slot structure. (Paper I).

The slot mode operation was theoretically investigated also for the visible region at 633 nm wavelength. As a background to the experimental demonstration of slot waveguide, the optimal waveguide dimensions were designed. The schematic illustration of the parameters for the design are shown in Figure 18. The refractive

indices used in the simulation were 1.457 (SiO_2), 1.553 (Ormocore), 1.33 (water) and 1 (air). In the design, the ridge width W_R = 1 µm and residual polymer layer thickness h_R = 150 nm were maintained as a constant and the optical mode flux in slot region was calculated for the top cladding material to be either water or air. For the demonstration, the waveguide mode has to be guided with both top cladding materials. Based on the mode calculation, the condition was verified as being fulfilled when filling factor in slot of Eguation (14) is over 1%. Figure 19 a) shows the dependence of percentage filling factor of TE mode on the slot width and the ridge height with water top cladding. When the top cladding is water, the TE-mode is guided with all simulated dimensions. Figure 19 b) indicates that the TE-mode becomes leaky in the air top cladding structure, when the ridge height decrease and the slot width increases (dark blue region). Figure 19 a) and b) present, that the dependency of the percentage filling factor of the slot width for constant ridge height is inversed in the air top cladding compared to the water top cladding. This indicates, that with a certain refractive index of the cladding, the percentage filling factor remains constant for each slot width. With the cladding RI of 1.24, the filling factor is nearly invariant of the slot width. The Figure 19 c) shows the dependence of percentage filling factor of TE mode on the slot width and the ridge height with a top cladding of RI 1.24. The Figure d) shows the percentage filling factors in a slot region for constant 750 nm ridge height and varying slot widths with top claddings RI's of 1, 1.24 and 1.33.

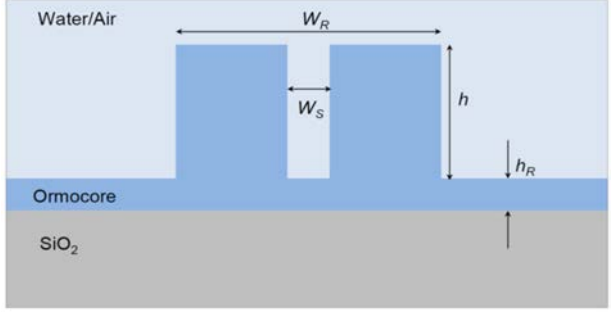

Figure 18. Schematic cross-section illustration of the polymer slot waveguide.

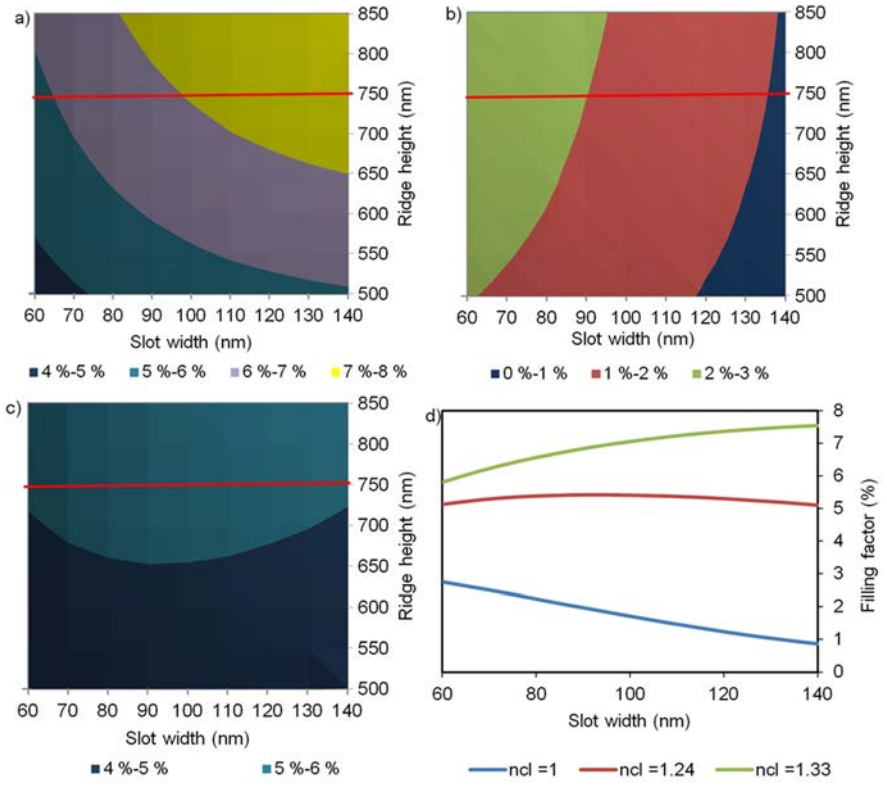

Figure 19. Percentage of filling factor for TE mode in the slot region with a) water b) air top cladding. The modes in the dark blue region are leaky. c) Percentage filling factor for TE mode in slot region with a cladding of n = 1.24. d) Percentage filling factor of the polymer slot waveguide with constant ridge height of 750 nm and for varying slot widths. The red line in a)-c) indicates the position, from where the filling factor values are taken.

5.1.2 Light-ambient interaction

In waveguide sensors, the effective refractive index of the waveguide mode should be highly sensitive to the refractive index of the ambient surroundings. The normalized effective refractive index change $\Delta n_{eff}/n_{eff}$ of TE mode in polymeric and composite waveguides was compared at the 1550 nm NIR wavelength. The normalization n_{eff} was calculated for cladding n = 1.32. Three different configurations was chosen: ridge, single slot and triple slot waveguide structures. In this sensitivity analysis, the mode effective RI values were calculated by FEM for the ambient cladding changing from 1.32 up to 1.33. The waveguide dimensions used in the sensitivity analysis were the same as in Figure 16 and Figure 17. The ridge waveguide otherwise had the same dimensions as the single slot waveguide structure,

but excludes the slot. The effective index shifts by the cladding index change in fully polymeric and composite waveguides are shown in Figure 20 a) and Figure 20 b), respectively. The single and triple slot polymeric waveguides have almost three- and four-fold better responses to the cladding index change compared to the polymer ridge waveguide as shown in Figure 20 a). Thin high index coating on the ridge waveguide improves the response by 2.4 times compared to the fully polymeric ridge waveguide. The response is further increased by a factor of 1.5 and 1.9, if one or three slots is included to composite structure.

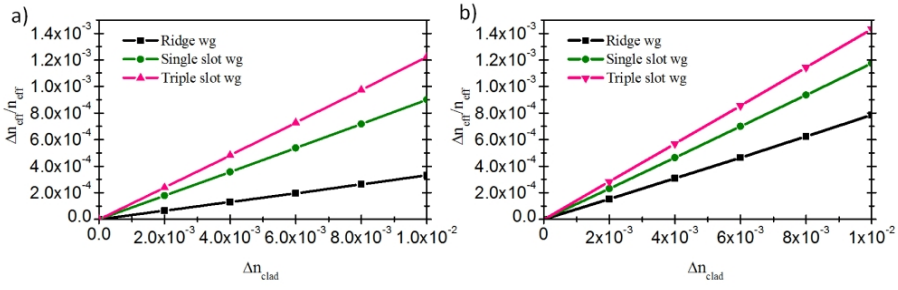

Figure 20. The effective index change comparison as a function of the cladding refractive index, which is varied from 1.32 to 1.33. a) Fully polymer waveguides. b) Polymer waveguides covered with a 50 nm thick TiO_2 layer.

5.2 Fabricated samples

Three different kinds of slot-waveguide Young interferometer were fabricated by exploiting NIL masters so as to produce the samples. For clarity, the samples types are labelled as A, B and C. The naming is shown in Table 1.The interferometer of type B operated as a single mode device at 1305 nm wavelength, while the others were demonstrated to be single mode devices at 633 nm wavelength.

Table 1. Naming of fabricated samples.

Name	NIL master fabrication	Operating wavelength	Slot length scale	Paper
A	E-beam lithography	633 nm	µm	II
B	Photolithography & FIB	1305 nm	µm	III
C	E-beam lithography	633 nm	mm	IV

5.2.1 Master fabrication

Combined photolithography and FIB milling master

A process for producing a master mould employed to fabricate a slot waveguide operating at 1305 nm wavelength is illustrated in Figure 21 (sample B). The master fabrication includes three main fabrications steps: (1) photolithography of positive tone resist, (2) nanoimprint moulding and (3) focused ion beam etching. First, Ultra-I 123 positive resist was spin-coated on a silicon wafer (800 RPM, 60 sec.) followed by a soft-bake of the resist (90 °C, 90 sec.). With the process parameters used, the resist thickness, defining the final pattern height, was approximately 1.3 µm. Vacuum contact lithography mode of Karl Suss MA6 Mask Aligner and I-line filter was exploited so as to provide good resolution of the pattern. The transfer resist was UV-exposed through a shadow mask defining the waveguide structures with dose of 300 mJ/cm^2, followed by a post-expose bake at 110 °C for 90 sec. Finally, the exposed areas were removed by rinsing for 2 minutes in an MA26 developer. This patterned positive tone resist stamp could only be used for a single imprint replication. For the nanoimprint step, the negative tone resist, Ormocore, was dispensed on a glass substrate. The patterns on positive tone stamp were replicated on Ormocore with a laboratory-customized imprinter. The Ormocore was hard-baked for one hour at 130 °C. A conductive aluminium coating was vacuum-evaporated on the Ormocore prior to the FIB milling. As a final step for the master fabrication, nanoscale slots were milled into Ormocore waveguide templates with an FIB system (FEI Helios Dualbeam 600). Three different slot lengths (40 µm, 80 µm and 120 µm) were milled into the middle of one arm of the Y-branch waveguide master. Finally, the aluminium was removed with 10% NaOH solution.

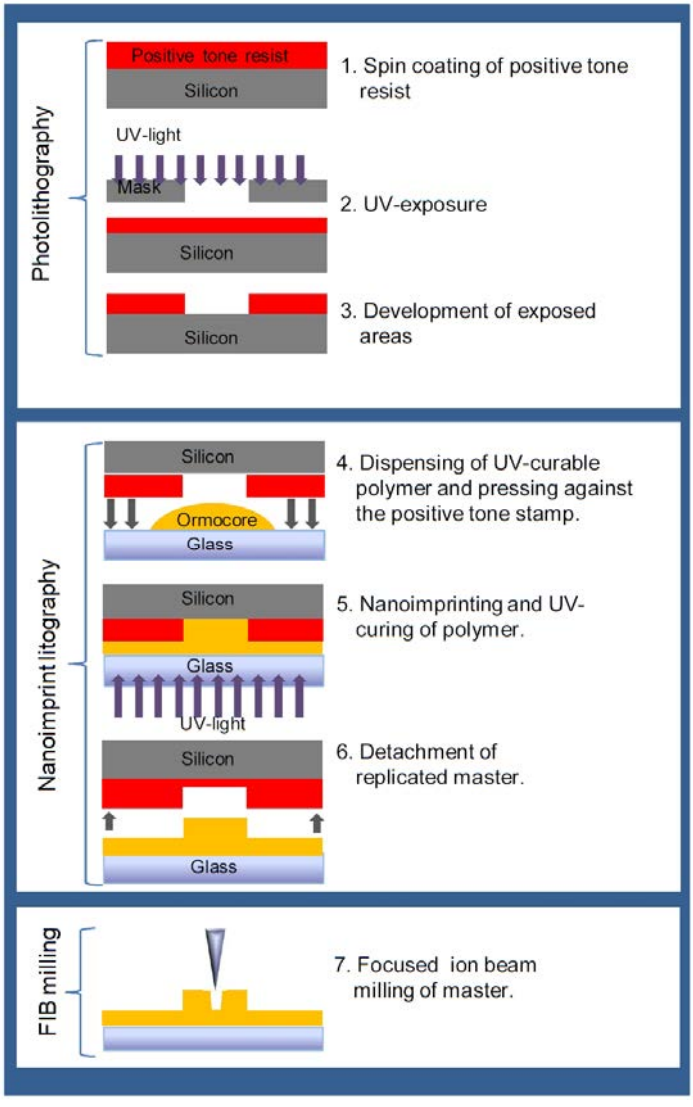

Figure 21. Main fabrication steps in making a master by combining photolithography, nanoimprint moulding and FIB milling.

Electron beam fabrication of a master

The master utilized to produce waveguide structures operating at 633 nm wavelength was fabricated with Vistec's EBPG5000+ES HR equipment. The master for sample B included three different lengths of slots (20 µm, 30 µm and 40 µm) in separate interferometers, and the total length of the Young interferometer patterns

was 10 mm. The master for sample C included slots either of length 5 mm or 10 mm, and the total length of the Young interferometer patterns were 30 mm. E-beam lithography enables the fabrication of a master mould including long slot sections, in contrast to the FIB milling method presented in the previous paragraph.

Despite the fabrication method, all the masters had identical ridge shapes in the final samples. Therefore, those needed to be replicated in order to fabricate a final mould for the waveguide NIL process. Prior to the replication, the masters were treated with an antiadhesion coating of (1,1,2,2 H perfluorooctyl)-trichlorosilane in a vapour-phase.

5.2.2 Mould fabrication

The replicas from the master mould were used as a mould for nanoimprinting the samples. The masters for producing a mould for replicating slot waveguides of the length of tens of micrometers (sample A and B) were replicated by dispensing Ormocomp on a glass wafer followed by imprinting using a customized laboratory imprinter and UV expose for 2 minutes. The master of an NIL mould for millimetre-long slot waveguide (sample C) was replicated into Ormostamp, which was spin-coated (at 2000 RPM, 60 sec.) on a glass wafer. The master and Ormostamp glass wafer stack was pressed with 1 bar pressure in Obducat Eitre 6 nanoimprint equipment, and exposed to UV-light for 2 minutes. Finally, each mould was treated with an antiadhesion coating.

5.2.3 Waveguide replication

The actual waveguide replication process of the samples was started by spin-coating diluted Ormocore (Ormocore:Ma-T1050, 1:7) on substrate. The substrate for sample B was borofloat glass. For samples A and C, a silicon wafer with a thermal oxide layer TEOS (oxide thickness 3 µm in sample A and 2 µm in sample C) acting as an undercladding layer was chosen for easier cutting up of the waveguides. After spinning, the thinner Ma-T1050 was evaporated out on a hotplate. For samples A and B, the waveguides of Ormocore were replicated from the Ormocomp moulds using laboratory customized imprinter and UV curing for 2 minutes. For waveguide replication of sample C, the Ormostamp mould was stacked up in contact with the Ormocore-coated wafer and pressed together at 10 bar pressure and UV-cured for 2 minutes in Obducat nanoimprinter. All the samples were hardened by post-baking them on hot plane at 130 °C for one hour. As a final fabrication step for the Young interferometer sensor, an optical lithography was performed using Ormostamp resist to provide a top cladding only in the input/output sections and to determine the length of the sensor window. Prior the measurement, the devices were placed in a plasma etcher (Pico, Diener Electronic GmbH) for 10 s to open the bonds on the imprinted Ormocore. The Figure 22 shows a microsope image of the fabricated Young interferometer sensor.

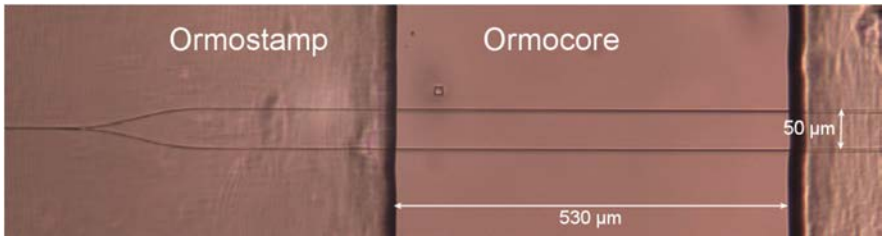

Figure 22. Microscope image of the fabricated slot Young interferometer.

The Young interferometers on glass wafers (sample B) were diced with an automatic dicing saw (Disco DAD 341) prior to the characterization. In order to protect the waveguide during the dicing, Ultra-I 123 positive tone resist was spin-coated on the wafer. The resist was removed with acetone after the dicing. The samples on TEOS were cleaved for producing good output facets of the waveguides.

5.3 Structural properties of the slot waveguide

Figure 23 shows the cross-section SEM images of fabricated slot waveguides. It can be seen that the slot in sample A Figure 23 a) and sample B Figure 23 b) are not fully open to the bottom of the waveguide. There are a few possible causes for incomplete opening of the slot; one originating from the master fabrication and another one from nanoimprint replication process. For example, the FIB-tooling of the master has not been deep enough or the etching in the e-beam lithography process has been incomplete. However, the most plausible cause is the partial filling of the master (and also the mould) during replication processes using the custom laboratory imprinter. The slot was completely open in the structure fabricated with commercial Obducat nanoimprint equipment, sample C Figure 23 c).

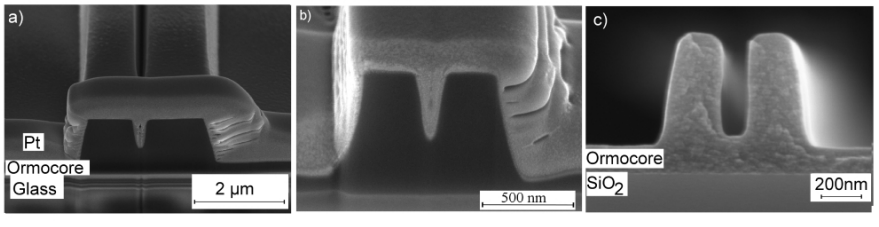

Figure 23. Cross-section images of slot waveguides fabricated in this work: a) operating at 1305 nm wavelength, photolithography and FIB milling used for master fabrication (Paper III) b) Operating at 633 nm, e-beam lithography for master fabrication (Paper II). C) Operating at 633 nm, e-beam lithography for master fabrication (Paper IV).

5.3.1 Slot waveguide loss

Analysis of the slot waveguide fabricated by using an FIB milled master

The scattering loss in the waveguide is proportional to the electric field amplitude at the core-cladding interfaces, the RI contrast at the interfaces and the surface roughness [78]. In the slot waveguide structure, where a large proportion of the modal electric field locates at the vertical interfaces, the waveguide losses may become very high [79]. Furthermore, additional loss arises from mode mismatching at the ridge–slot–ridge waveguide interfaces.

The roughness in the slot was analysed from FIB-milled Ormocore, shown in the SEM image in Figure 24 a), by atomic force microscope AFM (Veeco Dimensions 3100). The root mean square RMS roughness of the FIB milled edge and the sidewall were 2.4 and 2.0 nm, respectively. These small roughness values suggest that losses caused by the FIB milling roughness are very small. The roughness values of FIB-milled polymer are in the same magnitude than with E-beam process (3.6 nm) [80].

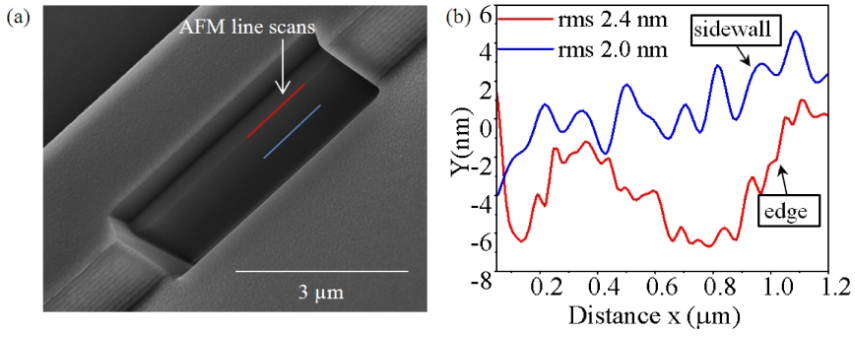

Figure 24. a) SEM image of the FIB-milled part of the Ormocore waveguide ridge. b) Roughness plot of the edge and sidewall region indicated as red and blue lines in a).

The average transmission for the slot and reference ridge arm of eight slot Young interferometer was measured for both TE and TM polarization state with a fibre coupling system shown in Figure 13 a). The wavelength used in the measurement was 1305 nm, and the lengths of the slots were 40, 80 and 120 µm. The transmission measurement proved that average 44% of optical power was transmitted through the slot-embedded waveguide arm. Since the length of the slot in waveguides fabricated by using FIB milled master are approximately 100 µm, the dB/cm loss value can't be determined accurately.

Analysis of slot waveguide fabricated by using e-beam lithography master

The transmission properties of the millimetre-long slot waveguide, fabricated by exploiting a master mould fabricated with the e-beam lithography method, were characterized at 633 nm wavelength for TM polarization. The free space light coupling set-up, shown in Figure 13 b), was utilized to measure the waveguide loss. A CMOS camera captured the mode profiles at the output facet of the Young interferometer. Still water was standing on the waveguides to improve the transmission. A loss in the slot waveguide was deduced from the normalized mode intensity profiles of a ridge waveguide arm and a waveguide arm consisting either a 5 mm or 10 mm long slot section. The intensity deviation between the two arms was measured to be below 20%. This value was obtained by comparing the output intensities of two identical waveguide arms (without slot structure). The slot waveguide loss of 14 dB/cm was calculated by comparing the mode intensities between the ridge and the slot consisting arm of these two slot lengths. The measured loss value also includes the coupling loss caused to the mode mismatching of the TM_{00}-modes at the ridge–slot–ridge interfaces. The coupling loss, calculated with an overlap integral method between the TM_{00}-modes in ridge–slot–ridge interfaces, was 1 dB. The loss in the TE polarization state was measured as 0.8 dB/cm higher than with the TM polarization state. The coupling loss for TE_{00}-modes at interfaces was calculated to be 1.6 dB.

Since the of waveguides fabricated by using e-beam master or FIB-master differ significantly from each other's with their operating wavelength and the slot length, the loss values in dB/cm are hard to compare. However, the low roughness values of FIB-milled Ormocore suggest, that the slot waveguide losses might be in the same magnitude than in waveguides fabricated by using e-beam master.

5.4 Sensing of bulk refractive index change

The slot Young interferometer operating at 1305 nm was exploited to demonstrate the slot mode operation in a polymeric slot waveguide in the NIR wavelength region. For the waveguide fabrication, the FIB milled master was used. The phase shift resulting from the change of ambient from air to water was measured with four different Young interferometers. One interferometer was used for reference measurement, and it did not include slot. Three interferometers had one reference arm, and the other arm consisted of a slot with length 40, 80 or 120 µm. The measurement was made for both the TE and TM polarization state, using fibre coupling measurement system. Table 2 shows the measured and simulated phase shifts for TE and TM polarization states. The effective RI both with air and water ambient in the slot and ridge waveguides were calculated using FEM, and the difference of the effective RI changes in the waveguide arms (Δn_{eff}) was inserted in Equation (13). The waveguide dimensions were extracted from Figure 23 with the assumption that the ridge waveguide has the same dimensions, but excluding the slot.

Table 2. Measured and simulated phase shifts for change of ambient from air to water.

		TE polarization		TM polarization	
Wavelength	Device/ Slot length (µm)	Measured phase shift	Simulated phase shift	Measured phase shift	Simulated phase shift
1305 nm Paper II	0 (reference)	0.00±0.01	0	0.00±0.01	0
	40	1.10±0.01	1.1	0.84±0.01	0.7
	80	2.66±0.01	2.3	1.91±0.01	1.4
	120	3.68±0.01	3.4	2.32±0.01	2.1
633 nm Paper III	0 (reference)	-0.4±0.3	0	-0.3±0.3	0
	20	1.1±0.3	1.34	1.1±0.3	1.04
	30	1.9±0.3	2.00	1.8±0.3	1.56
	40	3.0±0.3	2.69	2.7±0.3	2.08

The slot waveguide mode at visible wavelength was demonstrated utilizing a slot Young interferometer operating at 633 nm wavelength. The interferogram pattern generated at the 1.2 mm distance from the waveguide facet was video-recorded while a droplet of water was applied on the arms of Young interferometer. The distinct length of the slot in each measured interferometer was 20, 30 and 40 µm. Measured and simulated phase shifts for TE and TM polarizations are shown in Table 2. For the simulation, the waveguide dimensions were extracted from Figure 23. The differences of the measured and simulated phase shifts are attributed to the local waveguide variations and incomplete slot filling. Potentially, the depth or the width of the slots differs a little from the SEM image used for calculating the theoretical phase shift, causing the difference between the measured and the simulated phase shift.

For the bulk refractive index sensing measurements, aqueous glucose solutions (D-glucose, Sigma-Aldrich) of various molar concentrations (0.005%, 0.01%, 0.03%, 0.05%, 0.1%, 0.2% mol/L) were prepared. The bulk refractive index change at 20°C temperature, Δn_B, of the aqueous glucose solution with respect to deionized (DI) water was calculated based on empirical data from ref. [81]

$$\Delta n_B = 1.4014 \times \frac{(mol_g)}{(mol_{DI})}, \quad (15)$$

where mol_g and mol_{DI} are the amount of glucose and water in moles, respectively.

The bulk RI sensing measurement of the Young interferometer sensor, including 5 mm long slot in a sensor arm, was made at 633 nm wavelength for TE and TM polarizations using the measurement set-up shown in Figure 13 b). The waveguides were fabricated by utilizing e-beam lithography master. The fluidic cell was placed on the top of the sensor, as illustrated in Figure 25, and liquids of DI water and aqueous glucose solutions were pumped through the flow cell at the flow velocity of 250 µL/min using a syringe pump (Nexus 3000, Chemyx Inc.). The interference fringe pattern images generated at 1.35 mm distance from the waveguide facet focus were recorded with a CMOS camera (Pixelink, Model PL-E425CU). The phase of each interference image at the respective spatial period was extracted by using the two-dimensional Fast Fourier Transform (FFT) method. First, DI water was circulated through the sensor window followed by aqueous glucose flow. After each concentration of aqueous glucose, the sensor window was flushed with DI water before repeating the measurement with another glucose concentration. With TM polarization, the glucose concentration of 0.005% induced a phase response of 0.04 rad/min, as shown in Figure 26. This smallest measured concentration corresponds to the bulk refractive index change Δn_B of 6.4×10^{-6} with respect to DI water. Figure 27 a)–c) shows the phase shift response of 0.01%, 0.03% and 0.05% aqueous glucose solutions measured for both TE and TM polarization.

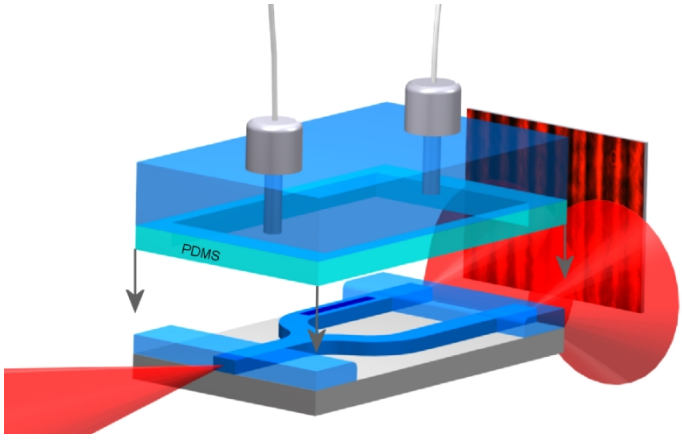

Figure 25. Schematic image of fluidic measurement set-up for bulk refractive index measurement.

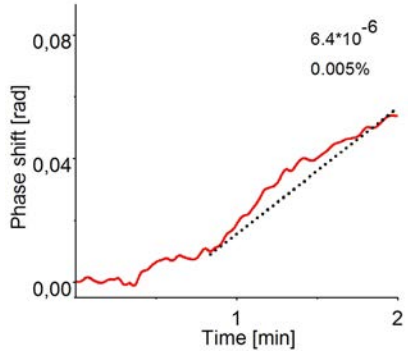

Figure 26. Phase shift response at TM polarization measured for water – 0.005% glucose-water concentration. The glucose solution is applied on the sample at the moment of 0.9 min. The dotted line indicates the slope of the phase shift over one minute.

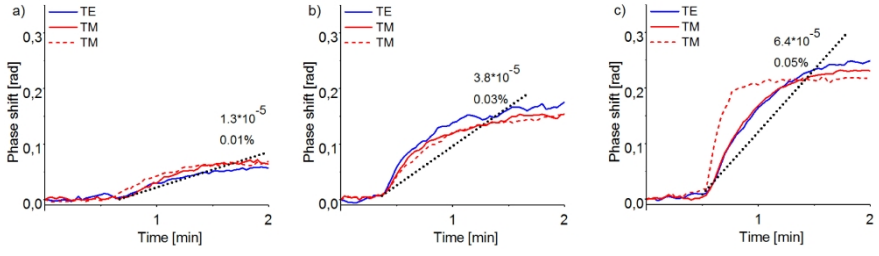

Figure 27. The phase shift response at TE and TM polarizations measured at various glucose-water concentrations as a function of time when glucose-water solution is applied into the sensing window. The dashed red line is a repeated measurement for TM polarization. The dotted line indicates the slope of the phase shift over one minute. The molar concentrations (mol/L) and the corresponding Δn_B with respect to the RI of DI water are marked above the glucose concentrations. Glucose concentrations are a) 0.01%, b) 0.03% and c) 0.05%. (Paper IV).

During the aqueous glucose solution flow, the phase shift increased in time in despite of the constant glucose concentration. This was assumed to be caused by the accumulation of glucose molecules in the slot region. To count out the phase drift caused by the glucose molecule accumulation, the phase shift caused by the RI change of the ambient material was calculated from the slope of the phase shift during one minute time period (starting at the moment of aqueous glucose solution flown into the sensing window). This slope of the phase shift is indicated as a dotted line in Figure 27. The measured slopes of phase shift and the simulated phase shift for different glucose solution concentrations are shown in Figure 28. The simulated phase shifts are calculated with equation (13) for 633 nm wavelength and 5 mm long slot length. The phase responses are for all measured glu-

cose concentrations fitted on the same linear line. Both the simulation and the experimental result show that the TM polarization shows a slightly higher response compared to the TE polarization.

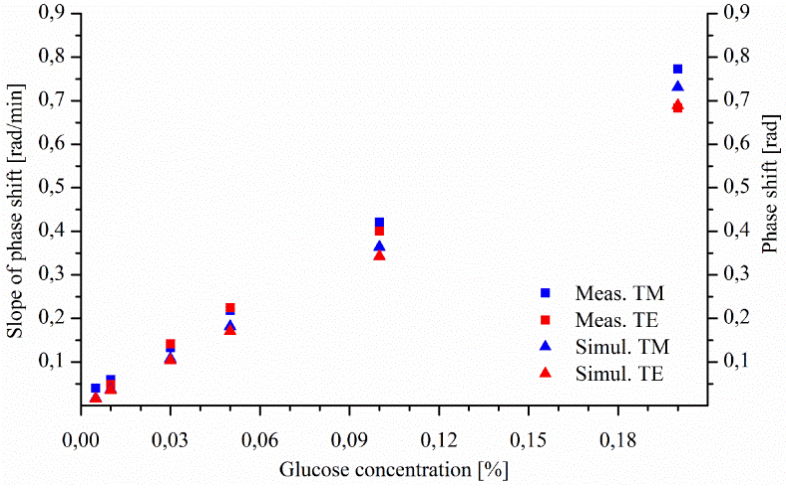

Figure 28. Plot of the measured slopes of the phase shifts in a one minute time period starting at the moment of glucose solution passed into the sensing window. Measurements for TM and TE polarizations are marked as blue and red squares, respectively. The blue (TM polarization) and the red (TE polarization) triangle markers represent the simulated phase shifts at the same glucose concentrations of the fabricated structure.

The origin of higher sensitivity at TM polarization was calculated for a fabricated slot waveguide and ridge waveguide geometries shown in Figure 29. For calculating the sensitivity of the slot and ridge waveguide, the following refractive indices were used: waveguide core n_{co} = 1.553 (Ormocore) and substrate n_{subst} = 1.457 (SiO2) as a sensor structure, deionized water n_D = 1.33299 and 1% (mol/L) concentration of glucose-water solution n_{GL} = 1.33427 as ambient materials. The change of the ambient material from DI water to 1% glucose-water solution caused an effective RI change, Δn_{eff}, of 1.52×10^{-4} in the slot waveguide, and 8.27×10^{-5} in the ridge waveguide for the transverse electric (TE) polarization state. For the transverse magnetic (TM) polarization state, Δn_{eff} were 1.44×10^{-4} and 7.03×10^{-5} for slot and ridge waveguide, respectively. It may be noted that the slot waveguide is more sensitive than the ridge waveguide to the bulk RI change in both polarization states. Although Δn_{eff} in the slot waveguide is higher at TE polarization, the total difference in Δn_{eff} between the ridge and the slot waveguide is slightly higher with TM polarization. The slot waveguide is more sensitive than the ridge waveguide to the bulk RI change in both polarization states. The sensitivity of the slot waveguide is higher with TE polarization state, while the sensitivity of the ridge waveguide is higher at TM polarization causing that sensitivity of the

whole waveguide device to be slightly higher with TM polarization. The mode sensitivity calculation for polymer slot waveguide interferometer arms was consistent with the characterization results.

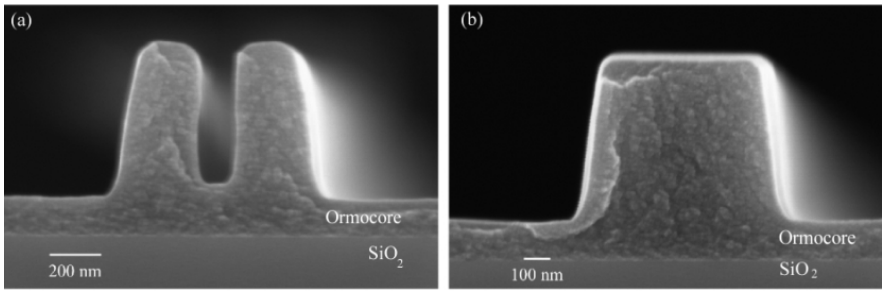

Figure 29. SEM image of a) slot waveguide and b) ridge waveguide in polymer Young interferometer. (PAPER IV)

5.5 Temperature response of the slot Young interferometer

The stability of the Young interferometer against temperature variation was experimentally determined for the device with both waveguide arms exposed to still DI water. The measurement was performed for the device without a slot and for devices with a slot of length either 5 mm or 10 mm. Figure 30 a) shows on an example intensity profile at the waveguide facet. The displacement of the mode intensity profiles was recorded for each stabilized temperature. The interference pattern generated when the microscope objective was moved 1.35 mm from the focus is shown in Figure 30 b). Also, the interference fringe pattern was recorded at each temperature after stabilization. The thermo-mechanical movement, shown in the displacement of mode intensity profiles, was extracted from the interference pattern displacement prior the phase shift calculation. The response of different Young interferometer structures to the temperature change was simulated. Figure 31 a) illustrates the geometry that is experimentally verified in this work. Usually, in the integrated Young interferometer measurements, the reference arm is covered with a cladding layer. The schematic image of each simulated structure is shown in Figure 31. The measured and simulated phase shift responses to the temperature change are shown in Table 3. The phase shift was calculated by Equation (13), with a modification of the symbol Δn_{eff} describing the derivative of the effective RI change in both of the waveguide arms as the RI of the waveguide and ambient material change. For the simulation, waveguide dimensions in the Figure 29 and the thermo-optic coefficient (TOC) of -2.5×10^{-4} / K and -9.4×10^{-5}/K were used for Ormocore and DI water, respectively [82]. There is a good correlation between the measured and simulated phase shifts. The measured phase shift compared to the simulated one is higher in the device with a longer slot, which is potentially attributed to local waveguide variations. Usually, in the integrated Young interferometers detecting ambient RI change, a part of the sensing arm is

open while the rest of the interferometer is protected with an overcladding layer. Therefore, the thermal phase shift of the structure similar to the regular Young interferometer was also calculated (illustrated in Figure 30b) and c)). In the simulation, the whole reference arm was assumed to be covered with Ormostamp (n = 1.515, TOC = -2.8×10^{-4}/K), and the length of the sensing window in the reference structure (without a slot) was 5 mm.

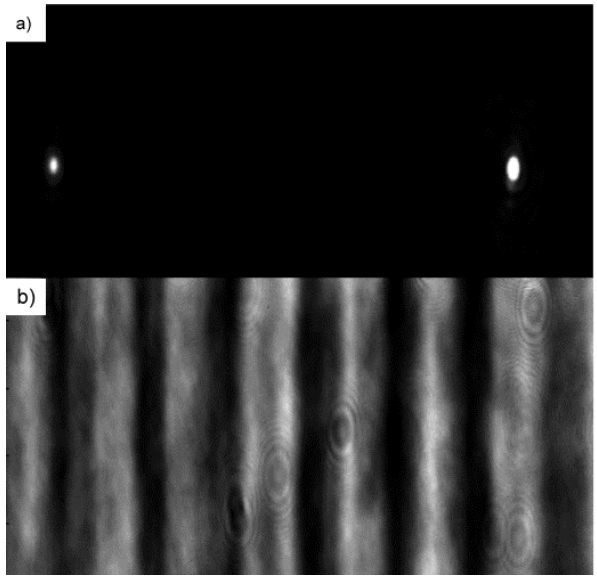

Figure 30. a) Image captured at the end of the slot Young interferometer waveguide. The left mode intensity profile consists of a waveguide with a 5 mm-long slot section and the right mode intensity profile consist of a ridge waveguide. b) The interferogram generated at 1.35 mm distance from the waveguide facet. (Paper IV).

Table 3. Measured and simulated phase shifts for temperature change.

Device Slot length (mm)	Measured phase shift (rad/K)	Simulated phase shift (rad/K)	Simulated phase shift with covered reference arm (rad/K)
0 reference	-0.3	0	2.9 (L = 5 mm)
5	2.1	2.2	5.1
10	5.7	4.3	10.1

By comparing the third and fourth column in Table 3, it can be seen that the temperature sensitivity of the structure with a protected reference arm has more than twice the response to the thermal variations than the structure with both waveguide arms open. Therefore, the temperature dependence of a proposed slot

Young interferometer structure is greatly reduced compared to a regular Young interferometer.

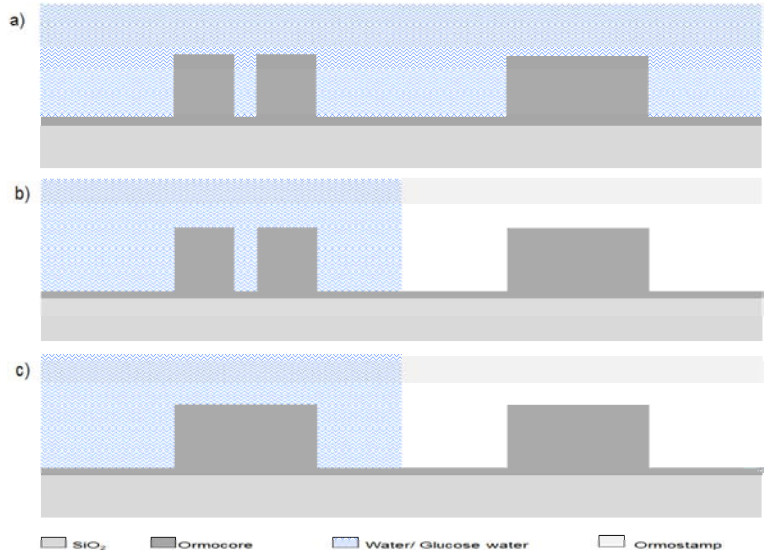

Figure 31. Different geometries of waveguide arms in the Young interferometer. a) Slot and ridge waveguide arms both sensing the changes of the ambient. b) Slot waveguide sensing the changing of the ambient while the reference ridge arm is protected with an overcladding layer. c) Ridge-sensing arm and protected reference arm.

The slot Young interferometer with a 5 mm-long slot is simulated to have a 2.2 rad/K response to the temperature change. This is slightly lower than in a ridge Young interferometer with a covered reference arm (2.9 rad/K). In order to compare the bulk RI sensitivity of the structures illustrated in Figure 31, the simulated phase shift caused by the ambient change from DI water to 1% glucose-water solution was calculated. In these simulations, a constant temperature of 20 °C was used. The simulated phase shifts caused by bulk RI change of ambient material for each structure are presented in Table 4.

Table 4. Simulated phase shifts for ambient RI change when DI water is replaced by 1% glucose-water solution.

Geometry	Phase shift for TM polarization (rad)
Slot YI, 5-mm-long slot waveguide, both arms open	3.6
Slot YI, 5-mm-long slot waveguide, reference arm covered	7.1
Ridge YI, 5-mm-long sensing window, reference arm covered	3.5

The bulk RI sensitivity of the slot Young interferometer with both waveguide arms open is approximately the same as the sensitivity of the ridge waveguide Young interferometer with a protected reference arm. Furthermore, the temperature sensitivity is less for the interferometer with both arms open compared to the one with the reference arm covered. The sensitivity of the slot Young interferometer could be doubled if the reference arm is protected at the expense of increased sensitivity to the temperature variations.

5.6 Future work

There are several methods for further improving the performance of the interferometer structure developed in this thesis work. For improving the sensitivity of the slot YI sensor, theoretically established multiple slot and high refractive index coated devices should be experimentally verified. Theoretical analysis of multislot waveguide geometry propose, that with the developed device fabrication process even further enhanced light-ambient interaction with low thermal fluctuation might be achieved. The protection of the reference arm with a polymer layer would increase the bulk RI sensitivity, even with a single slot fully polymeric YI. By combining reference arm protection and multislot with a high RI coating, greatly increased sensitivity might be achievable. Furthermore, the length of the sensing window could be increased with longer slot waveguides, just as long as the interference pattern intensity remains readable. The ridge–slot–ridge interface mode-coupling loss could be reduced with an adiabatic coupling structure.

The influence of the nanoscale slot for the specific molecular binding events need to be studied, in order to determine the selectivity of the developed sensor. The applicability of the developed interferometer as a biosensor could be verified by investigating the molecule specific detection with an antibody–antigen binding interactions. Moreover, for the biosensor applications, multiparameter sensing applications could be realized with integrating several parallel YI into one input.

6. Summary

The main aim of this thesis was to demonstrate the slot waveguide operation with polymer material for both visible and NIR wavelengths. Commercial UV-curable inorganic-organic hybrid polymers Ormocer®, were used to fabricate the slot waveguide-based sensor devices. The emphasis was to develop the device fabrication process by employing low-cost nanoimprint moulding method and subsequent photolithography with very loose alignment tolerances. This opens up the possibility for mass-producible fabrication of disposable sensors.

The polymer slot waveguide structure was designed to produce strong light–matter interaction. Theoretically, the interaction was established to be increased with multislot geometry and with a thin high refractive index coating on the polymer. To enable the experimental verification of the slot waveguide operation, two different methods of fabricating original master mould for nanoimprint process was studied. One consisted of an e-beam patterning process, and the other combined several process steps, such as, photolithography, nanoimprint moulding and FIB milling. With both master mould fabrication methods, viable slot Young interferometers were replicated. The e-beam lithography was verified as a feasible method for fabricating a master mould for a long slot waveguide replication process.

The operation of slot waveguide was demonstrated for 1305 nm and 633 nm wavelengths with a novel Young interferometer structure established in this work. The operation of the developed Young interferometer was based on the phase shift difference produced at the length of the slot waveguide embedded into one of the Y-branch arms of the device. The reference arm experiences the same changes of the ambient as the sensor arm, which assists in compensating for the thermal fluctuation of the ambient. It was established that the YI sensor developed in this work is less sensitive to the temperature variations as a conventional YI sensor, where a reference waveguide arm is protected with a polymer overcladding.

The developed slot waveguide YI sensor was evaluated for both TE and TM polarization states, with glucose–deionized water solutions for homogenous bulk RI sensing. The lowest measured RI change was 6.4×10^{-6}. If tolerating more constrains fabrication tolerances and increase of the noise coming from the thermal fluctuations, the limit of detection could be further improved by combining the slot waveguide geometry into a conventional Young interferometer, with a reference arm protected with polymer overcladding. Furhermore, theoretical analysis of

multislot waveguide geometry proposed, that even further increased sensitivity of the Young interferometer with low thermal fluctuations might be achieved.

References

[1]. Hunsperger, R. G. Integrated Optics Theory and Technology. Sixth Edition. Springer 2009. Chapter 1. ISBN 978-0-387-89776-9.

[2]. Nishihara, H., Haruna, M. and Suhara, T. Optical Integrated Circuits. New York, NY: Mc Graw-Hill Publishing Company, 1985. Chapter 1. ISBN 0-07-046092-2.

[3]. Brenner, K.-H. Programmable optical processor based on symbolic substitution. Applied Optics 1988. Vol. 27, pp. 1687–1691.

[4]. Nishihara, H., Haruna, M. and Suhara, T. Optical Integrated Circuits. New York, NY: Mc Graw-Hill Publishing Company, 1985. Chapter 11. ISBN 0-07-046092-2.

[5]. Hunsperger, R. G. Integrated Optics Theory and Technology. Sixth Edition. Springer 2009. Chapter 20. ISBN 978-0-387-89776-9.

[6]. Zengerle, R. and Leminger, O. Phase-shifted Bragg-grating filters with improved transmission characteristics Journal of Lightwave Techology 1995. Vol. 13, pp. 2354–2358.

[7]. Little, B. E., Foresi, J. S., Thoen, E. R., Chu, S. T., Haus, H. A., Ippen, E. P., Kimerling, L. C. and Greene, W. Ultra-Compact Si-SiO_2 microring resonator optical channel dropping filters. Photonics Technology Letters 1998. Vol. 10, pp. 549–551.

[8]. Zabelin, V., Dunbar, L. A., Le Thomas, N. and Houndre R. Self-collimating photonics crystal polarization beam splitter. Optics Letters 2007. Vol. 32, pp. 530–532.

[9]. Kwon, D.-H. and Werner, D- H. Polarization splitter and polarization rotator design based on transformation optics. Optics Express 2008. Vol. 16, pp.18731–18738.

[10]. Almeida, V. R., Xu, Q., Barrios, C. A. and Lipson, M. Guiding and confining light in void nanostructure. Optics Letters 2004. Vol. 29, pp. 1209–1211.

[11]. Barrios, C. A. and Lipson, M. Electrically driven silicon resonant light emitting device based on slot-waveguide. Optics Express 2005. Vol. 13, pp. 10092–10101.

[12]. Fujisawa, T. and Koshiba M. Polarization-independent optical directional coupler based on slot waveguides. Optics Letters 2006. Vol. 31, pp. 56–58.

[13]. Lin, S., Hu, J. and Crozier, K. B. Ultracompact, broadband slot waveguide polarization splitter. Applied Physics Letters 2011. Vol. 98, pp. 151101-1-3.

[14]. Barrios, C. A. High-performance all-optical silicon microswitch. Electronics Letters 2004. Vol. 40, pp. 862–863.

[15]. Koos, C., Dumon, P., Baets, R., Esembson, B., Biaggio, I., Michinobu, T., Diederich, F., Freude, W. and Leuthold, J. Highly-nonlinear silicon photonics slot waveguide. Proceeding Optical Fiber Communication Conference 2008.

[16]. Martinez, A., Blasco, J., Sanchis, P., Galan, J. V., Garcia-Ruperez, J., Jordana, E., Gautier, P., Lebour, Y., Hernandez, S., Spano, R., Guider, R., Daldosso, N., Garrido, B., Fedeli, J. M., Pavesi, L. and Marti, J. Ultrafast all-optical switching in a silicon-nanocrystal-based silicon slot waveguide at telecom wavelengths. Nanoletters 2010. Vol. 10, pp. 1506–1511.

[17]. Lee, J. M., Kim, D.-J., Kim, G.-H., Kwon, O.-K., Kim, K.-J. and Kim, G. Controlling temperature dependence of silicon waveguide using slot structure. Optics Express 2008. Vol. 16, pp. 1645–1652.

[18]. Ramirez, J. M., Lupi, F. F., Berencen, Y., Anapchenko, A., Colonna, J. P., Jambois, O., Fedeli, J. M, Pavesi, L., Prtljaga, N., Rivallin, P., Tengattini, A., Navarro-Urrios, D. and Garrido, B. Er-dobed light emitting slot waveguides monolithically integrated in a silicon photonic chip. Nanotechnology 2013. Vol. 24, pp. 115202.

[19]. Barrios, C. A., Gylfason, K. B., Sanchez, B., Griol, A., Sohlström, H., Holgado, M. and Casquel, R. Slot-waveguide biochemical sensor. Optics Letters 2007. Vol. 32, pp. 3080–3082.

[20]. Carlborg, C. F., Gylfason, K. B, Kazmierczak, A., Dortu, F., Banuls Polo, M., Maquieira Catala, A., Kresbach, G. M., Sohlsröm, H., Moh, T., Vivien, L., Popplewell, J., Ronan, G., Barrios, C. A., Stemme, G. and van der Wijngaart, W. A packaged optical slot-waveguide ring resonator sensor array for multiplex label-free assays in lab-on-chips. Lab on a chip 2010. Vol. 10, pp. 281–290.

[21]. Wang, M., Hiltunen, J., Liedert, C., Hakalahti, L. and Myllylä, R. An integrated Young interferometer based on UV-imprinted polymer waveguides

for label-free biosensing applications. Journal of European Optical Society Rapid. Publications. 2012. Vol. 7, pp. 12019-1-7.

[22]. Chao, C.-Y., Fung, W. and Jay Guo, L. Polymer microring resonators for biochemical sensing applications. Journal of selected topics in quantum electronics 2006. Vol. 12, pp. 134–142.

[23]. Nishihara, H., Haruna, M. and Suhara, T. Optical Integrated Circuits. New York, NY: Mc Graw-Hill Publishing Company, 1985. Chapter 2. ISBN 0-07-046092-2.

[24]. Snyder, A. W and Love, J. D. Optical Waveguide Theory. First Edition. Chapman and Hall Ltd. Chapter 1. ISBN 0-412-23250-8.

[25]. Snyder, A. W and Love, J. D. Optical Waveguide Theory. First Edition. Chapman and Hall Ltd. Chapter 30. ISBN 0-412-23250-8

[26]. Saleeh, A. W and Love, J. D. Optical Waveguide Theory. First Edition. Chapman and Hall Ltd. Chapter 30. ISBN 0-412-23250-8.

[27]. Lusse, P., Stuwe, P., Schule, J. and Unger, H.-G. Analysis of vectorial mode fields in optical waveguides by new finite difference method. Journal of Lightwave Technology 1994. Vol. 12, pp. 487–494.

[28]. Huang, W. P., Chu, S. T. and Chaudhuri, S. K. A scalar finite-difference time –domain approach to guided-wave optics. Photonics Technology Letters 1991. Vol. 3, pp. 524–526.

[29]. Sudbo, A. S. Film mode matching: a versatile numerical method for vector mode field calculations in dielectric waveguides. Pure Applied Optics 1993. Vol. 2, pp. 211–233.

[30]. Säynätjoki, A., Bai, B., Tervonen, A., Turunen, J. and Honkanen, S. Enhanced vertical confinement in angled-wall slot waveguides. Optical Review 2010. Vol. 17, pp. 181–186.

[31]. Manolatou, C. and Haus, H. Passive components for dense optical integration. First Edition. Kluwer Academic Publishers. Chapter 1. ISBN 0-7923-7603-X.

[32]. FimmWave and FimmProp softwares, Photon Desing Ltd. Oxford. U.K.

[33]. Dossou, K. and Fontaine, M. A high order isoparametric finite element method for the computation of waveguide modes. Computational Methods Applied Mechanics and Engineering 2005. Vol. 194, pp. 837–858.

[34]. Feng, N.-N. and Haung, W.-P. Time-domain reflective beam propagation method. Journal of Quantum Electronics 2004. Vol. 40, pp.778–783.

[35]. Gallagher, D. F. G. and Felici, T. P. Eigenmode expansion method for simulation of optical propagation in photonics- Pros and Const. Proceeding of Integrated optics: Devices, materials and technologies VII SPIE 2003. Vol. 4987, pp. 69–82

[36]. Bruck, R., Melnik, E., Muellner, P., Hainberger, R. and Lämmerhofer, M. Integrated polymer-based Mach-Zehnder interferometer label-free strepavidin biosensor compatible with injection molding. Biosensors and Bioelectronics 2011. Vol. 26, pp. 3832–3837.

[37]. Yang, B., Hu, R., Sheng, Z., Dai, D., Liu, Q. and He, S. Fabrication and characterization of small optical ridge waveguides based on SU-8 polymer. Journal of Lightwave Technology 2009. Vol. 27, pp. 4091–4096.

[38]. Byun, Y. T., Park, K. H., Kim, S. h., Choi, S. S. and Lim, T. K. Single-mode GaAs/AlGaAs W waveguides with low propagation loss. Applied Optics 1996. Vol. 35, pp. 928–933.

[39]. Xu, Q., Almeida, V. R., Panepucci, R. R. and Lipson, M. Experimental demonstrations of guiding and confining light in nanometer-size low refractive index material. Optics Letters 2004. Vol. 29, pp. 1626–1628.

[40]. Sun, R., Dong, P., Feng, N.-N., Hong, C., Michel, J., Lipson, M. and Kimerling L. Horizontal single and multiple slot waveguides: optical transmission at λ =1550 nm. Optics Express 2007. Vol. 15. Pp. 17967–17972.

[41]. Vivien, L., Marri, D., Griol, A., Gylfason, K. B., Hill, D., Alvarez, J., Sohlström, H., Hurtado, J., Boulville, D. and Cassan, E. Vertical multiple-slot waveguide ring resonators in silicon nitride. Optics Express 2008. Vol. 16, pp. 17237–17242.

[42]. Barrios, C. A., Sanchez, b., Gylfason, K.b., Sohlström, H., Holgado, M. and Casquel, R. Demonstration of slot-waveguide structures on silicon nitride/silicon oxide platform. Optics Express 2007. Vol. 15, pp. 6836–6856.

[43]. Baehr-Jones, T., Hochberg, M., Walker, C. and Scherer, A. High-Q optical resonators in silicon-on-insulator-based slot waveguides. Applied Physics Letters 2005. Vol. 86, pp. 081101-1-3.

[44]. Alasaarela, T., Säynätjoki, A., Hakkarainen, T. and Honkanen S. Feature size reductions of silicon slot waveguides by partial filling using atomic layer deposition. Optical Engineering 2009. Vol. 48, pp. 08502-1-3.

[45]. Karvonen, L., Säynätjoki, A., Chen, Y., Tu, X., Liow, T.-Y., Hiltunen, J., Hiltunen, M., Lo, G.-Q. and Honkanen S. Low-loss multiple-slot waveguides fabricated by optical lithography and atomic layer deposition. Photonics Technology Letters 2012. Vol. 24, pp. 2074–2076.

[46]. Jordana, E., Fedeli, J.-M., El Melhaoui, L., Lyan, P., Colonna, J. P., Daldosso, N., Pavesi, L., Pellegrino, P., Garrido, B, Vila, A. and Lebour, Y. Deep-UV lithography fabrication of slot waveguides and sandwiched waveguides for nonlinear applications. IEEE International conference on Group IV Photonics 2007. Japan. Pp. 1–3.

[47]. Almeida, V. R., Barrios, C. A., Panepucci, R. R. and Lipson, M. All-optical control of light on silicon chip. Nature 2004. Vol. 432, pp. 1081–1084.

[48]. Yang, A. H. J., Moore, S. D., Schmidt, B. S., Klug, M., Lipson, M. and Erickson, D. Optical manipulation of nanoparticles and biomolecules in sub-wavelength slot waveguides. Nature 2009. Vol. 457, pp. 71–75.

[49]. Barrios, C. A. Optical slot-waveguide based biochemical sensors. Sensors 2009. Vol. 9, pp. 4751–4765.

[50]. Gylfalson, K. B., Carlborg, C. F., Kazmierczak, A., Dortu, F., Sohlström, H., Vivien, L., Barrios, C. A., van der Wijngaart, W. and Stemme, G. On-chip temperature compensation in an integrated slot-waveguide ring resonator refractive index sensor array. Optics Express 2010. Vol. 18, pp. 3226–3237.

[51]. Zhou, L., Okamoto, K. and Yoo, S. J. B. Athermalizing and trimming of slotted silicon microring resonators with UV-sensitive PMMA upper-cladding. Photonics Technology Letters 2009. Vol. 21, pp. 1175–1177.

[52]. Yang, S. H., Cooper, M. L., Bandaru, P. and Mookherjea, S. Giant birefringence in multi-slotted silicon nanophotonics waveguides. Optics Express 2008. Vol. 16, pp. 8306–8316.

[53]. Testa, G. and Bernini, R. Slot and layer-slot waveguide in the visible spectrum. Journal of Lightwave Technology 2011. Vol. 29, pp. 2979–2984.

[54]. Wang, M., Hiltunen, J., Liedert, C., Pearce, S., Charlton, M., Hakalahti, L., Karioja, P. and Myllylä, R. Highly sensitive biosensor based on UV-inmprinted layered polymeric-inorganic composite waveguides. Optics Express 2012. Vol. 20, pp. 20309–20317.

[55]. Voskerician, G., Shive, M. S., Shawgo, R. S., von Recum, H., Anderson, J. M., Cima, M. J. and Langer, R. Biocomaptilility and biofouling of MEMS drug delivery devices. Biomaterials 2003. Vol. 24, pp. 1959–1967.

[56]. Ahmadi, L., Tervo, J., Saarinen, J. and Honkanen, S. Enhanced sensitivity in polymer slot waveguides by atomic layer deposited bilayer coatings. Applied Optics 2013. Vol. 52, pp. 8089–8094.

[57]. Lambeck, P. V. Integrated optical sensors for the chemical domain. Measurement Science and Technology 2006. Vol. 17, pp. R93–R116.

[58]. HORIBA Ltd, Scientific innovative SPRi.

[59]. Farfield Group Ltd, *Ana*Light ®.

[60]. Homola, J., Sinclair, S. Y. and Gauglitz, G. Surface plasmon resonance sensors: review. Sensors and actuators B 1999. Vol. 54, pp. 3–15.

[61]. Khan, A., Krupin, O., Lisicka-Skrzek, E. and Berini, P. Mach-Zehnder refractometric sensor using long-range surface plasmon waveguides. Applied Physics Letters 2013. Vol. 103, pp. 111108-1-4.

[62]. Schmitt, K., Schirmer, B., Hoffmann, C., Branderburg, A. and Meyrueis, P. Interferometric biosensor based on planar optical waveguide sensor chips for label-free detection of surface bound bioreactions. Biosensors and bioelectronics 2007. Vol. 22, pp. 2591–2597.

[63]. Wang, X. and Madsen, C. K. Highly sensitive compact refractive index sensor based on phase-shifted sidewall Bragg gratings in slot waveguide. Applied Optics 2014. Vol. 53, pp. 96–102.

[64]. Fan, X., White, I. M., Shopova, S. I., Zhu, H., Suter, J. D. and Sun, Y. Sensitive optical biosensors for unlabelled targets: A review. Analytica Chimica Acta 2008. Vol. 620, pp. 8–26.

[65]. Kim, J.-W., Kim, K.-J., Yi, J.-A. and Oh, M.-C. Polymer waveguide label-free biosensors with enhanced sensitivity by incorporating low-refractive-index polymers. Journal of selected topics in Quantum Electronics 2010. Vol., 16, pp. 973–980.

[66]. Brandenburg, A. and Henning, R. Integrated optical Young interferometer. Applied Optics 1994. Vol. 33, pp. 5941–5947.

[67]. Saleh B. E. A. and Teich, M. C. Fundamentals of Photonics. John WilwySons, Inc., 1991. Chaper 2. ISBN 0-471-83965-5.

[68]. Ymeti, A., Kanger, J. S., Wijn, R., Lambeck, P. and Greve, J. Development of multichannel integrated interferometer immunosensor. Sensors and Actuators B 2002. Vol. 83, pp. 1–7.

[69]. Moon, M.-M., Han., J. H., Vaziri, a., Her, E. K, Oh, K. H., Lee, K.-R. and Hutchinson, J. W. Nanoscale ripples on polymers created by a focused ion beam. Nanotechnology 2009. Vol. 20, pp. 115301.

[70]. Chou, S., Krauss, P. R. and Rengstom P. J. Imprint of sub-25 nm vias and trenches in polymers. Applied Physics Letters 1995. Vol. 67, pp. 3114–3116.

[71]. Guo, L. J. Nanoimprint lithography: Methods and material requirements. Advanced Materials 2007. Vol. 19, pp. 495–513.

[72]. Guo, L. J. Recent progress in nanoimprint technology and its applications. Journal of Physics D: Applied Physics 2004. Vol. 37, pp. 123–141.

[73]. Cheng, X. and Guo, J. L. A combined-nanoimprint-and-photolithography patterning technique. Microelectronics Engineering 2004. Vol. 71, pp. 277–282.

[74]. Kim, J. W., Plachetka, U., Moormann, C. and Kurz, H. Fabrication of inverse micro/nano pyramid structures using soft UV-NIL and wet chemical methods for residual layer removal and Si-etching. Microelectronics Engineering 2013. Vol. 110, pp. 403–407.

[75]. Ulrich, R. and Torge, R. Measurement of thin film parameters with a prism coupler. Applied Optics 1973. Vol. 12, pp. 2901–2908.

[76]. Visser, T. D., Demeulenaere, B., Haes, J., Lenstra, D., Baets R. and Blok H. Confinement and modal gain in dielectric waveguides. Journal of Lightwave technology 1996. Vol. 14, pp. 885–887.

[77]. Alasaarela, T., Saastamoinen, T., Hiltunen, J., Säynätjoki, A., Tervonen, A., Stenberg, P., Kuittinen, M. and Honkanen, S. Atomic mayer deposited titanium dioxide and its application in resonant waveguide grating. Applied Optics 2010. Vol. 49, pp. 4321–4325.

[78]. Payne, F. P. and Lacey, F. P. A theoretical analysis of scattering loss from planar optical waveguides. Optical and Quantum Electronics 1994. Vol. 26, pp. 977–986.

[79]. Zhang, H., Zhang, J., Chen, S. Song, J. Kee, J. S., Yu, M. and Lo G.-Q. CMOS-compatible fabrication of silicon-based sub-100-nm slot waveguide with efficient channel-slot coupler. Photonics Technology Letters 2012. Vol. 24, pp. 10–12.

[80]. Yap, K. P., Delage, A., Lapointe, J., Lamontagne, B., Schmid, J. H., Waldron, P., Syrett, B. A. and Janz, S. Correlation of scattering loss, sidewall roughness and waveguide width in silicon-on-insulation (SOI) ridge waveguides. Journal of Lightwave Technology 2009, Vol. 27, pp. 3999–4008.

[81]. Fucaloro, A. F., Pu, Y., Cha, K., Williams, A. and Conrad, K. Partial molar volumes and refractions of aqueous solutions of fructose, glucose, mannose and sucrose at 15.00, 20.00, and 25.00°C. Journal Solution Chemica 2007. Vol. 36, pp. 61–80.

[82]. Daimon, M. and Masumura, A. Measurement of the refractive index of distilled water from the near-infrared region to the ultraviolet region. Applied Optics 2007. Vol. 46, pp. 3811–3820.

PAPER I

Polymer based single and multislot waveguides

In: Proc SPIE 8068, pp. 806812-1-6.

Polymer based single and multislot waveguides

M. Hiltunen*[a], J. Hiltunen[a,b], Antti Suutala[b], Jarkko Tuominen[a], Pentti Karioja[a]
[a]VTT Technical Research Centre of Finland, Kaitoväylä 1, 90570 Oulu, Finland;
[b]OU, Dept. of Microelectronics and materials physics laboratories, P.O. Box 4500, 90014 University of Oulu, Finland

ABSTRACT

We discuss the applicability of using polymers for producing slot waveguide modes in single and triple-slot waveguide structures. We use finite element method to computationally study the field confinement and enhancement in the slot region with and without high refractive index coating on the top of the low index polymeric waveguide. The sensitivity to refractive index shift in ambient surrounding is improved almost five times in proposed high index coated polymer triple-slot waveguide structure compared to the ridge polymer waveguide.

Keywords: Slot waveguide, polymer

1. INTRODUCTION

Slot waveguides guide and confine the light in the sub-wavelength low refractive index region between high refractive index rails or layers[1][2]. The width of the slot has to be much smaller than the decay length of the modefield inside the slot. Typical slot widths of silicon/silica slot waveguides are in 100 nm regime[3]. Such a small feature sizes are challenging to fabricate. The width of the slot can be increased by decreasing the index contrast between the rails and slots [4]. With the silicon-nitride/silicon oxide slot waveguide structure, the slot widths are increased up to 200 nm regime, relieving the fabrication constraints[5][6]. The electric field inside the slot of refractive index n_L is higher than inside the high index rails (n_H) by the factor of n_H^2/n_L^2 [1]. Therefore, by reducing the index contrast, the slot mode field enhancement decreases too. On the other hand, scattering loss caused by the surface roughness decrease and the structure becomes less sensitive to device-dimension deviations. Some liquids are also easier to introduce inside the wider slots [7].

Optical waveguides fabricated by imprinting UV-curable polymers have demonstrated to have high optical transmission[8]. The imprinting technique enables reproducible low-cost and high-throughput fabrication of waveguides. The motivation for this work was to investigate the formation of slot mode into a low refractive index polymer waveguide. The larger localization of the electric field in the slot region can be achieved with a structure consisting of multiple slots [5]. The optical field can be localized more on the top surface of low refractive index waveguide with high refractive index coating [9][10]. The electric field is enhanced in the slot region by adding the high index coating and increasing the number of the slots. As a framework for the simulation, we used our previous studies on polymer waveguide fabricated from commercial UV-curable polymer Ormocore and preliminary demonstrations of FIB etching of Ormocore slab and using those FIB milled structures as a replica of imprinting mould [8][11]. Focused ion beam lithography has been demonstrated for high-resolution (below 80 nm) deep etching or milling [12].

2. DESIGN OF SLOT WAVEGUIDE

2.1 Polymer waveguide

The schematic cross section pictures of single and triple-slot waveguides are shown in Figure 1. The angle and the width (w_{slot}) of the slot are assumed to be 4.7 deg and 330 nm, respectively, which are obtained from our preliminary study on FIB etching of Ormocore material [11]. The sidewall angle of the polymer is assumed to be 3 deg based on our previous studies on ridge type of imprinted polymer waveguides [8]. The imprinting method is successfully used for fabricating ridge type waveguide. Since the method is based on the pressing the mould against the spin coated polymer without applying a subsequent etching step, a thin residual layer of polymer will remain on the substrate. When optimizing the waveguide dimensions, the slot width of 330 nm, slot height of 1500 nm and the residual layer thickness 200 nm were kept as a constant.

Bioelectronics, Biomedical, and Bioinspired Systems V; and Nanotechnology V, edited by Ángel B. Rodríguez-Vázquez, Ricardo A. Carmona-Galán, Gustavo Liñán-Cembrano, Rainer Adelung, Carsten Ronning, Proc. of SPIE Vol. 8068, 806812 · © 2011 SPIE · CCC code: 0277-786X/11/$18 · doi: 10.1117/12.886815

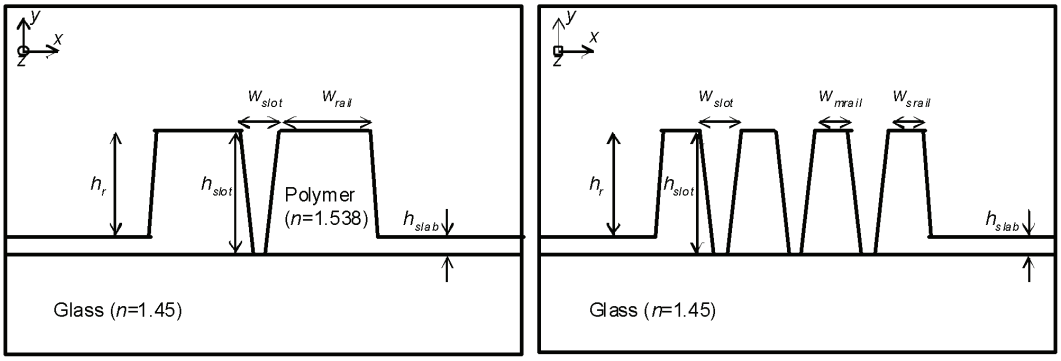

Figure 1. Left) Schematic of the single slot waveguide and Right) triple-slot waveguide. The middle rail width w_{mrail} and side rail width w_{srail} are the same in all polymer waveguides. Residual layer h_{slab}, slot width w_{slot} and slot height h_{slot} are constant 200nm, 330nm and 1500nm, respectively, in all the simulated structures.

To model the waveguide operation, we use finite element (FEM) method which is available in waveguide simulation software, Fimmwave [13]. The FEM divides the calculation area into the triangular meshes and is therefore suitable method for calculating the modes in angled wall waveguides. The FEM mesh grid density parameters n_{xres}=n_{yres} are set to be 120 and the wavelength used in the simulations is λ=1550nm. The refractive index of the Ormocore is 1.538 [11] and the glass substrate is set to 1.45 at 1550nm wavelength. We optimized the height and the width of the waveguide rails in order to achieve the single mode waveguide structure with the highest fraction of the optical mode flux in the slot area. The optical mode flux f_s in the slot is calculated by the equation

$$f_s = \frac{\int_S P_z(a).da}{\int_\infty P_z(a).da} \qquad (1)$$

in which the $P_z(a)$ is time averaged Poynting vector and the nominator is integral over the slot region S [14]. For single slot structure with water cladding (n_{cl}=1.33) the optimal height of the rail is 1300 nm and the width is 1085 nm. These dimensions give the highest mode power flux of 6.3% in the slot. For further increase the mode power flux in the slot region, we added two slots into the structure. The total rail width remained about the same as in single slot structure, when the rail widths in triple-slot structure were 545 nm. Increase in the number of the slots resulted in the increase of the mode power flux up to 12 % in the slot regions. Figure 2 shows the intensity profiles of the quasi-TE modes in the single and triple-slot waveguides. The mode intensity profile resembles the higher order mode profile because of the multiple intensity maximums. However, these multiple intensity maximums are caused by the slot structure and the mode is the first order TE slot mode. As seen from the cross section plot of the transverse electric (E_x) modefield in the bottom, middle and the top of the slot in Figure 2 b) and d), the field is confined and slightly enhanced in the slot region.

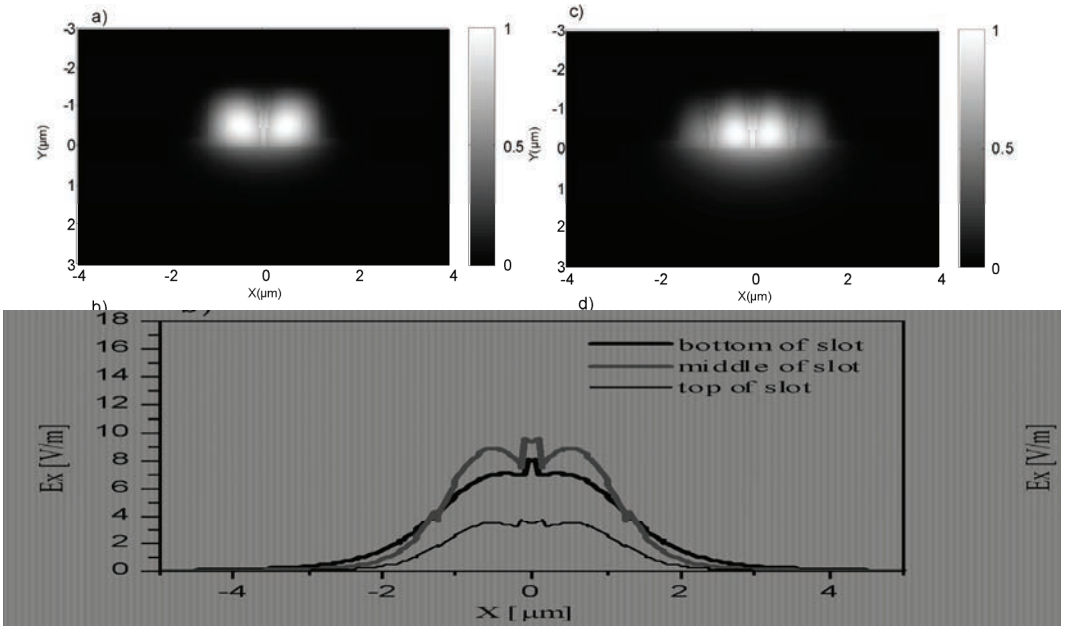

Figure 2. a) The intensity distribution of quasi-TE mode in a single slot waveguide with the 1085 nm rail width and 330 nm slot width. The height of the rail is 1300 nm and the depth of the slot is 1500 nm. b) The cross sections of the transverse electric *Ex* field of TE mode on the bottom, middle and the top of the slot in the single slot structure. c) The intensity distribution of quasi-TE mode in triple-slot waveguide with the 545 nm rail width and 330 nm slot width. d) The cross sections of the *Ex* field on the bottom, middle and the top of the slot in the triple-slot structure.

2.2 TiO_2 covered polymer slot waveguides

The electric field inside the slot of refractive index (n_L) is higher than inside the high index rails (n_H) by the factor of n_H^2/n_L^2. Since the refractive index contrast between the Ormocore and the water cladding is low, the high field enhancement is not achievable in polymer slot waveguide. However, the field can be guided more in the slot region and therefore this kind of structure is more sensitive to refractive index shift of ambient surrounding than conventional ridge waveguide. Increasing the index contrast between the slot and the rail by adding thin high index layer on the top of waveguide enhances the field inside the slot. Manipulation of the optical field by depositing high refractive index inorganic layer on the low refractive index waveguide has been studied in Refs. [9][10]. Amorphous TiO_2 has high refractive index and good optical properties at 1550 nm wavelength. Therefore we studied the influence of the 50 nm thick TiO_2 layer with refractive index of 2.018 on the top of the polymer on the field enhancement and confinement in slot region. The schematic of the structure is shown in Figure 3. Again, the rail height of 1300 nm gives the highest mode power flux in the slot, but the mode power flux could be further increased up to 7% by narrowing the rail width to 585 nm. The total rail width was kept the same in the triple-slot structure, but the width of the middle w_{mrail} and side rails w_{srail} were varied in order to see the effect of the relative distance of the slots on the mode confinement in the slot of the high-index-covered polymer. As seen on the right side of the Figure 3, the mode flux in the triple-slot structure can be increased up to 15%, if the slots are brought very close to each other. In the optimal three-slot structure the side rail and middle rail widths are 500 nm and 100 nm, respectively.

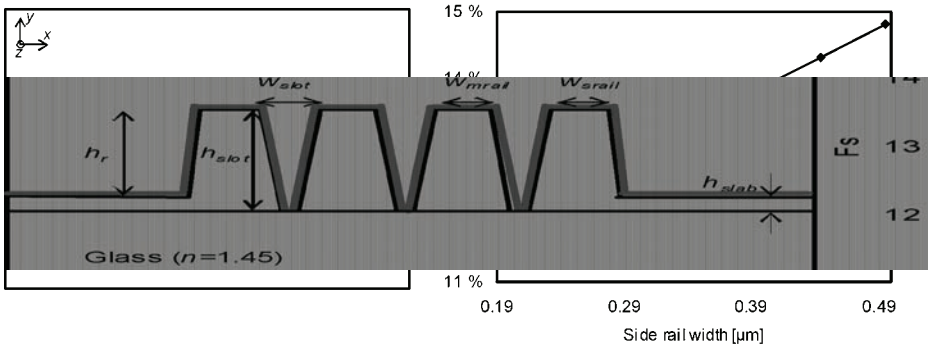

Figure 3. Left) Schematic of the triple-slot waveguide covered with 50nm thick TiO_2 layer. The middle rail width w_{mrail} and the side rail width w_{srail} are varied for highest mode flux in the slot regions. Right) The mode flux in the slot regions as a function of the side rail width.

The intensity distribution of the quasi-TE mode shown in Figure 4 indicates that a thin high index cover cause higher field confinement in the slot region compared to bare polymer structure. The cross section plot in Figure 4 of the E_x modefield shows discontinuity of the electric field at the high-index interfaces and field enhancement in the slot region.

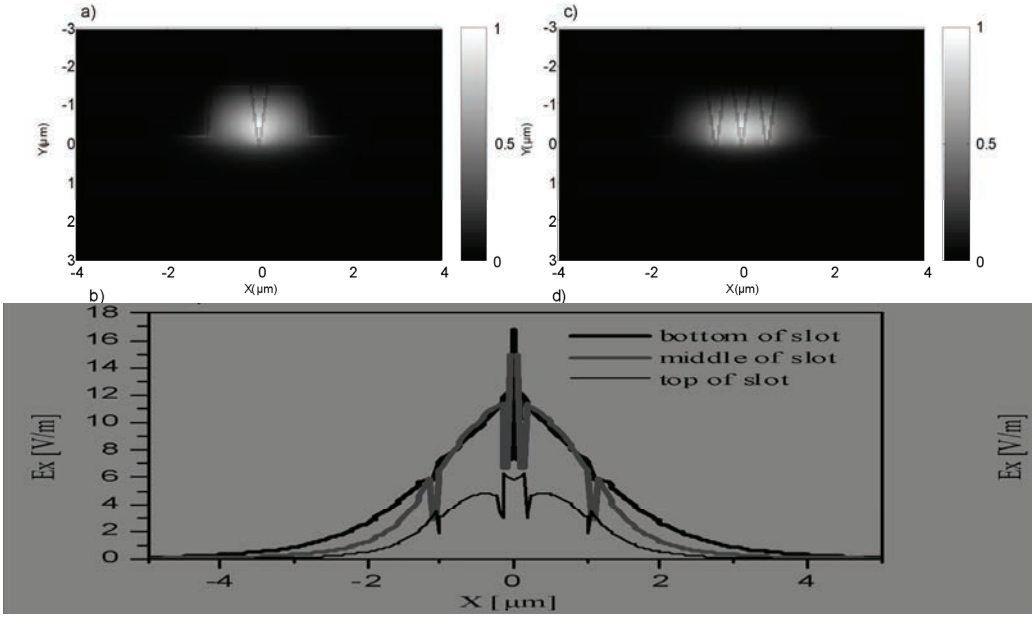

Figure 4. a) The intensity distribution of quasi-TE mode in TiO_2 covered single slot waveguide with the 585 nm rail width and 330 nm slot width. Height of the rail is 1300nm and the depth of the slot is 1500 nm. b) The cross sections of the *Ex* field on the bottom, middle and the top of the slot in the single slot structure. c) The intensity distribution of quasi-TE mode in a triple-slot waveguide with the 500 nm side rail, 100 nm middle rail and 330 nm slot width. d) The cross sections of the *Ex* field on the bottom, middle and the top of the slot in the triple-slot structure.

2.3 Effective index shift

A large effective index shift of the waveguide mode with the small refractive index change in the ambient surrounding of the waveguide is desirable in sensor applications. We changed the top cladding refractive index from 1.32 to 1.33 with 0.01 refractive index step and calculated the normalized effective index change $\Delta n_{eff}/n_{eff}$ of TE mode. We calculated the $\Delta n_{eff}/n_{eff}$ for single and triple-slot bare and TiO_2 covered polymer waveguides and as a reference also the ridge waveguide with the same dimensions as in the single slot waveguide, but without the slot. Figure 5 shows that in a bare polymer ridge waveguide, the refractive index change in the second decimal of the cladding can be seen in the fourth decimal of the effective index. Including one or three slots into the waveguide improves the effective index change three or four times. TiO_2 covered ridge waveguide is twice as sensitive to refractive index shift than the bare polymer ridge waveguide. However, the effective index variation further improves 50% and 90% with one or three slots, respectively, compared to TiO_2 covered ridge waveguide. One must keep in mind, that the slot regions in bare polymer and TiO_2 covered structures are not the same, since the TiO_2 layer narrows the original 330 nm wide slot.

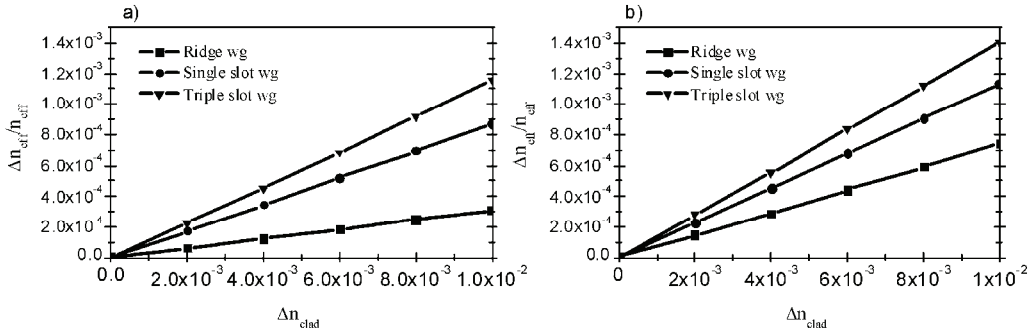

Figure 5. The effective index shift comparison as a function of the cladding refractive index, which is varied from 1.32 to 1.33. a) All polymer waveguides. b) Polymer waveguides covered with a 50 nm thick TiO_2 layer.

3. CONCLUSIONS

Although the formation of the enhanced field in a slot region requires a high refractive index contrast between the rail and the slot, we showed that the mode power flux in the slot can be increased also in lower refractive index polymer slot waveguides. The refractive index contrast between the slot region and the waveguide rails was increased with a 50 nm thick high index coating, causing stronger electric field localization and enhancement in the slot. The field localization was further increased with a triple-slot structure. The relative separation of the slots slightly influences the field localization in the triple slot structure. The sensitivity on the refractive index shift is improved almost five times in the proposed high index coated polymer triple-slot waveguide structure compared to the ridge polymer waveguide.

4. ACKNOWLEDGEMENTS

The research is supported by the Academy of Finland project 137331.

REFERENCES

[1] Almeida V. R, Xu Q., Barrios C. A and Lipson M., “Guiding and confining light in void nanostructure,” Optics Letters 29(11), 1209-1211, (2004).

[2] Sun R., Doing P., Feng N.N, Hong, C., Michel J. Lipson M. and Kimerling L., “Horizontal single and multiple slot waveguides: optical transmission at λ =1550nm”, Optics express 15(26) 17967-17972, (2007).

[3] Xu Q, Almeida V. R, Panepucci R.R. and Lipson M., “Experimental demonstration of guiding and confining light in nanometer-size low-refractive-index material,” Optics Letters 29(14) 1626-1628, (2004).

[4] Alasaarela T. Säynätjoki A., Hakkarainen T., Honkanen S., “Feature size reduction of the silicon slot waveguides by partial filling using atomic layer deposition,” Optical Engineering, 48(8), 080502-1-3, (2009).

[5] Vivien L., Marris-Morini D., Griol A., Gylfason K. B., Hill D., Alvarez J., Sohlström H., Hurtado J., Bouville and Cassan E., “Vertical multiple-sot waveguide ring resonators in silicon nitride”, Optics Express 16(22), 17237-17242, (2008).

[6] Barrios C. A., Sanchez B., Gylfason, Griol A., Sohlström H., Holgado M. and Casquel R., “Demontration of slot-waveguide structures on silicon nitride/silicon oxide platform,” Optics Express 15(11) 6846-6856, (2007).

[7] Barrios C. A. “optical Slot-Waveguide based biochemical sensors,” Sensors 9, 4751-4765, (2009).

[8] Hiltunen J., Hiltunen M., Puustinen J., Lappalainen J. and Karioja P., "Fabrication of optical waveguides by imprinting. Usage of positive tone resist as a mould for UV-curable polymer," Optics Express 17(25), 22813-22822, (2009).

[9] Hiltunen J. Uusitalo S., Karioja P., Pearce S., Charlton M., Wang M., Puustinen J. and Lappalainen J., ” Manipulation of optical field distribution in layered composite polymeric-inorganic waveguides,” Applied Physics Letters 98, 111113-1-3, (2011)

[10] Alasaarela T., Saastamoinen T., Hiltunen J., Säynätjoki A., Tervonen A., Stenberg P., Kuittinen M., and Honkanen S., ”Atomic layer deposited titanium dioxide and its application in resonant waveguide grating,” Applied Optics 49(22), 4321-4325, (2010)

[11] Ormocore Datasheet, Microresist Technology
http://www.microresist.de/products/ormocers/pdf/pi_ormocore_clad_en_07062201_ls_neu.pdf

[12] Cabrini S., Carpentiero a., Kumar R., Businaro L., Candeloro P., Prasciolu M., Gosparini A., Andreani C., De Vittorio M., Stomeo T. and Di Fabrizio E., “ Focused ion beam lithography for two dimensional array structures for photonic applications”, Microelectronic Engineering 78-79, 11-15. (2005).

[13] FimmWave software, Photon Design Ltd., Oxford, U.K.

[14] Visser T.D., Demeulenaere B., haes J., Lenstra D., Baets R. and Blok H., “Confinement and modal gain in dielectric waveguides,” Journal of Lightwave technology 14(5), 885-887 (1996).

PAPER II

Polymeric slot waveguide at visible wavelength

In: Optics Letters 37(21), pp. 4449–4451.

Polymeric slot waveguide at visible wavelength

Marianne Hiltunen,[1,*] Jussi Hiltunen,[1] Petri Stenberg,[2] Jarno Petäjä,[1] Esa Heinonen,[3] Pasi Vahimaa,[2] and Pentti Karioja[1]

[1]*VTT Technical Research Centre of Finland, Kaitoväylä 1, 90570 Oulu, Finland*

[2]*University of Eastern Finland, Department of Physics and Mathematics. P.O. Box 111, 80101 Joensuu, Finland*

[3]*Center of Microscopy and Nanotechnology, PL 7150, 90014 University of Oulu, Finland*

**Corresponding author: Marianne.Hiltunen@vtt.fi*

Received August 23, 2012; revised September 14, 2012; accepted September 17, 2012; posted September 17, 2012 (Doc. ID 174578); published October 23, 2012

Polymeric slot waveguide structure, which pushes the mode field toward the surrounding media, was designed and characterized. The slot waveguide was fabricated by using nanoimprint lithography, and the operation of the slot was demonstrated at 633 nm wavelength with an integrated Young interferometer. The experimental result shows that the nanolithography method provides possibilities to fabricate disposable slot waveguide sensors. © 2012 Optical Society of America

OCIS codes: 220.4241, 230.7370, 120.3180, 280.4788.

In slot waveguides, the optical field is confined and enhanced in the subwavelength slot region of low refractive index material sandwiched between higher refractive index lateral rails or vertical layers [1]. The light-confining feature of slot structures enables various applications, for example, optical trapping, all-optical switching, and sensing [2–4]. Originally, the slot waveguide structure was based on silicon, and to date, silicon and silicon nitride are the most widely investigated materials to produce slot waveguides [4,5]. Demonstrated silicon slot waveguides, however, are working at the near infrared (1300–1550 nm) wavelength due to the fact that silicon is not transparent at visible range. At visible wavelengths, theoretical investigation on modal and sensing properties of slot waveguides have also been carried out [6,7]. Visible wavelengths are often preferred in sensing applications. For example, fluorescence typically requires excitation with visible wavelength. In some sensing applications, the overall device performance is influenced by the optical absorption of water. The absorption of water is about two thousand times lower at visible wavelength range than in near IR [8].

The motivation for the present work was to study the mode properties in the low refractive index polymeric slot waveguides operating at visible wavelength. The fabrication of the designed slot waveguide structures using nanoimprint technology was also investigated in this work. Optical waveguides fabricated by nanoimprinting of UV-curable polymers have good optical transmission [9]. The imprinting technique enables reproducible low-cost and high-throughput fabrication of waveguides. In sensor applications, the reusability might require a complicated cleaning procedure between analyses. Therefore, in this work, we investigate a method to realize disposable polymeric sensor chips for sensing applications.

In order to push the optical field into the slot region, the parameters of the slot waveguide were first optimized. The waveguide structure is shown in Fig. 1. The properties of waveguide modes were calculated with the finite element method available in the commercial waveguide simulation software FIMMWAVE [10]. The refractive indexes in the simulation were 1.457 for the thermal oxide silicon wafer, 1.553 for polymer (Ormocore), 1.33 for water, and 1.0 for air at a wavelength of 633 nm [11]. The ridge height, h; width, W_R; and slot width, W_S were varied in order to maximize the proportion of the modal field in the slot region. The polymer residual layer, h_R, was maintained constant at 150 nm. This residual layer thickness is typical for the available imprinting process.

The filling factor of TE or TM modes in the slot region is defined as the fraction of optical mode flux f_s in the slot by the equation

$$f_s = \frac{\int_S P_Z(a)\mathrm{d}a}{\int_\infty P_Z(a)\mathrm{d}a}, \tag{1}$$

where $P_z(a)$ is the time averaged Poynting vector and the nominator is integral over the slot region S [12]. All the simulated structures support only one TE mode, but some structures have multiple TM modes. The higher order modes can be filtered out by applying an overcladding layer. Figure 2 shows the dependence of percentage of filling factor on the slot width and the ridge height. The ridge width is 1 μm and top cladding material is either water or air. When the filling factor is close to 1%, the mode is leaky. For the fabrication, the nominal parameters of $h = 750$ nm, $W_R = 1$ μm, and $W_S = 100$ nm were chosen. With these parameters, the TE modes are guiding with both top claddings, and over 7% of the optical field is localized in the slot of the water-covered structure. The lateral electric field. E_x, distribution of the fundamental TE mode in such a polymeric slot waveguide with water cladding is shown in Fig. 3(a). The vertical cross-section plot of the E_x field is shown in

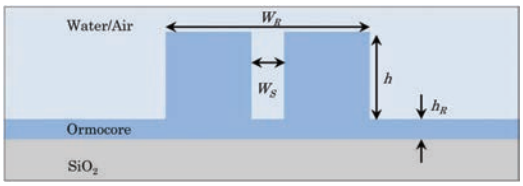

Fig. 1. (Color online) Schematic cross section illustration of the polymer slot waveguide.

0146-9592/12/214449-03$15.00/0

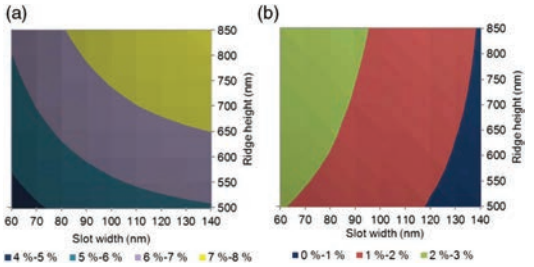

Fig. 2. (Color online) Percentage of filling factor of TE mode in the slot region with water (a) and air top cladding (b).

Fig. 3(b), illustrating that the maximum of the optical field locates in the slot.

In the present work, a Young interferometer configuration, which effectively compensates temperature changes [13], was utilized to experimentally verify that the light propagates in the waveguide as a slot mode. The operation is based on the phase difference produced by two waveguide arms. One waveguide arm of the Young interferometer is a regular ridge waveguide and the other arm includes a slot with a length of 0, 20, 30, or 40 μm. One interferometer was without the slot structure and acted as a reference device.

The master mold for the imprint was fabricated on a silicon substrate. The structures were patterned by e-beam lithography on a negative tone HSQ resist. Then the resist was developed and postbaked at 300°C for 1 h to harden the resist. In the following master fabrication step, the silicon was etched for 6 min in an HBr-based inductively coupled plasma-reactive-ion etching (ICP-RIE) process. Then HSQ resist was removed with buffered hydrofluoric acid (BHF). Finally, the master was treated with an antiadhesion coating material. Fabrication of the waveguide sample included two replication steps. First, the master was replicated on a borofloat glass wafer by dispensing Ormocomp hybrid polymer on the glass, imprinting and UV curing the replicated mold. The Ormocomp mold utilized to fabricate actual waveguides was released from the master and treated with antiadhesion coating. The waveguide replication process was started by spin coating diluted Ormocore (Ormocore:Ma-T1050, 1:7) on a silicon wafer with a 3 μm thick thermal oxide layer acting as an undercladding layer. The thinner portion (Ma-T1050) was evaporated at 85°C for 40 min. Next, the Ormocomp glass

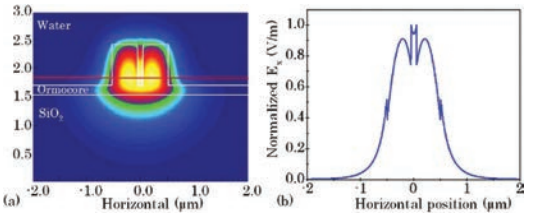

Fig. 3. (Color online) (a) Electric field E_x profile of TE-mode in the slot waveguide. (b) Cross-section plot of the E_x field of TE mode indicated as a red line in the 2D plot of the E_x electric field profile. The waveguide dimensions are $h = 750$ nm, $W_R = 1$ μm, $W_S = 100$ nm, and $h_R = 150$ nm.

mold was used to replicate the final Young interferometer structure on Ormocore by nanoimprinting and UV curing. Then the patterned waveguides were hardened by postbaking for 1 h at 130°C. In order to isolate the nonsensing region of the waveguides from the sensing cell and filter the propagation of higher order TM modes, the overcladding layer of Ormostamp with the refractive index of 1.517 was processed by using photolithography. The opening of the sensing cell was 530 μm ± 3 μm measured with a Veeco white light interferometer. Figure 4 shows the microscope image of the fabricated Young interferometer together with the top and cross-section scanning electron microscope (SEM) images of a slot structure.

Total length of the interferometer was 10 mm, and the distance between two arms was 50 μm. A short distance between the sensing and reference arms decreases the effect of local temperature variation and improves the readability of the interferogram. The interferometric measurement setup is shown in Fig. 5. A laser operating at 633 nm was used as a visible light source. TE or TM polarization was adjusted with the fiber optic polarization controller, and the correct polarization state was verified with an external polarizer before the waveguide measurements. The light from the polarization controller was coupled into the polarization maintaining tapered fiber. The interference pattern was recorded with a VIS-NIR camera. A microscope objective with 20X magnification was placed after waveguides to collect the output beams. Then the microscope objective was moved 1.2 mm away from the focus to get the far-field fringe pattern with vertical parallel lines. The interferogram pattern was video recorded while a droplet of water was applied on the arms of the Young interferometer.

The irradiance of the interferogram pattern can be described by [14]

$$I = I_1 + I_2 + 2\sqrt{I_1 I_2}\cos(\Delta\varphi - \delta), \tag{2}$$

where I_1 and I_2 are intensities of two interfering waveguide beams, $\Delta\varphi$ is the phase difference of the beams, and δ is the additional phase shift due to the difference

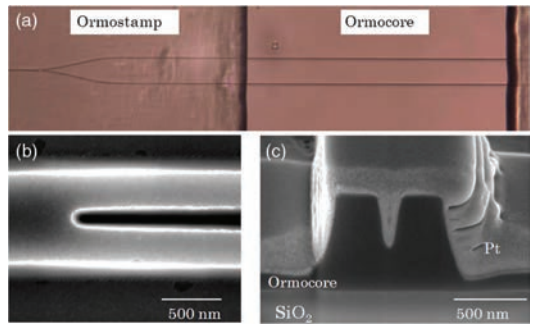

Fig. 4. (Color online) (a) Microscope image of the fabricated slot Young interferometer. The sensing cell is opened from the Ormostamp overcladding layer. (b) SEM image taken from the beginning of the slot. (c) Cross-section SEM image of the slot. Platinum was deposited on the polymer to improve the quality of the image.

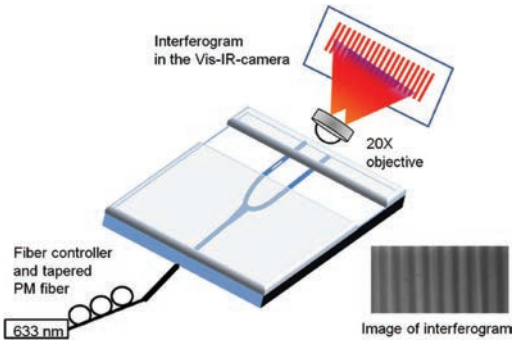

Fig. 5. (Color online) Schematic of the measurement setup. Right: Image of the interferogram on a visible-infrared (VIS-IR) camera.

of effective refractive index changes between two waveguide arms at the length of the slot. The higher fraction of modal power propagates in the top cladding of the arm with a slot rather than in the reference arm, inducing additional phase shift in the fringe pattern. This additional phase shift can be calculated by the equation

$$\delta = 2\pi \frac{L}{\lambda_0} \Delta n_{\text{eff}}, \tag{3}$$

in which L is the length of the slot, λ_0 is the wavelength in vacuum, and $\Delta n_{\text{eff}} = \partial n_{\text{eff}}/\partial n_{\text{clad}}$ is the derivative of effective index change in both waveguide arms as the cladding index n_{clad} changes. The phase shift of interference pattern is evaluated at the respective spatial period by a fast Fourier transform.

Measured and simulated phase shifts for TE and TM polarizations are shown in Table 1. The simulated phase shift values were calculated for the waveguide dimensions derived from the cross-section SEM image in Fig. 4. The effective refractive indices of TE and TM modes in the slot and ridge waveguides both with air and water cladding were calculated and the values were inserted in Eq. (3). There is relatively good correlation between the measured and simulated phase shifts, especially with TE polarization. In the fabricated structure, the calculated effective refractive index change is twice as high in slot waveguide as in ridge waveguide. As seen in Fig. 4, the sidewalls of the ridge and slot are angled. Moreover, the slot is not fully opened down to the bottom. The absolute error of the measurement is estimated to be about ± 0.3 rad for both polarizations. The potential factors for this error are attributed to local waveguide variations, incomplete slot filling, and low intensity level caused from high mode mismatching at Ormostamp-sensing cell interfaces. Even a slot a few tens of nanometers deeper causes a higher phase shift. Potentially, the depth or width of the slot differs a little from the SEM image, causing the difference between the measured and simulated phase shift. In the future the accuracy can be improved; for instance, with an adiabatic taper at the protection cover and sensing cell interface or with a high refractive index coating. In this first demonstration, the refractive index change of top cladding is high. By including a longer slot, the sensitivity of the structure can be greatly improved.

Table 1. Measured and Simulated Phase Shifts

Device/w Slot Length (μm)	Measured Phase Shift TE Polarization	Simulated Phase Shift TE Polarization	Measured Phase Shift TM Polarization	Simulated Phase Shift TM Polarization
0 reference	-0.4 ± 0.3	0	-0.3 ± 0.3	0
20	1.1 ± 0.3	1.34	1.1 ± 0.3	1.04
30	1.9 ± 0.3	2.00	1.8 ± 0.3	1.56
40	3.0 ± 0.3	2.69	2.7 ± 0.3	2.08

In addition, to estimate the propagation loss in the slot, a device with a 6 mm long slot in one arm was fabricated. By comparing the transmission in both arms, the loss in the slot was estimated to be about 20 dB/cm.

In conclusion, we demonstrated the operation of a slot waveguide at visible wavelength. We also demonstrated that slot waveguides can be fabricated from polymer materials, and that potentially low-cost nanoimprint fabrication can be utilized to fabricate such devices, therefore providing the possibility for disposable sensor applications.

This work is supported by the Finnish Academy grants 137331 (M.H.), 137276 (P.S.), and 133814 (J.H.).

References and Notes

1. V. R. Almeida, Q. Xu, C. A. Barrios, and M. Lipson, Opt. Lett. **29**, 1209 (2004).
2. A. H. J. Yang, S. D. Moore, B. S. Schmidt, M. Klung, M. Lipson, and D. Erickson, Nature **457**, 71 (2009).
3. V. R. Almeida, C. B. Barrios, R. R. Panepucci, and M. Lipson, Nature **431**, 1081 (2004).
4. C. A. Barrios, Sensors **9**, 4751 (2009).
5. A. Säynätjoki, L. Karvonen, T. Alasaarela, X. Tu, T. Y. Liow, M. Hiltunen, A. Tervonen, G. Q. Lo, and S. Honkanen, Opt. Express **19**, 26275 (2011).
6. G. Testa and R. Bernini, J. Lightwave Technol. **29**, 2979 (2011).
7. P. Bettotti, A. Pitantti, E. Rigo, F. De Leonardis, V. M. N. Passaro, and L. Pavesi, Sensors **11**, 7327 (2011).
8. W. S. Pegau, D. Gray, and J. R. V. Zaneveld, Appl. Opt. **36**, 6035 (1997).
9. J. Hiltunen, M. Hiltunen, J. Puustinen, J. Lappalainen, and P. Karioja, Opt. Express **17**, 22813 (2009).
10. FIMMWAVE software, Photon Design Ltd., Oxford, UK.
11. Ormocore datasheet, Microresist Technology.
12. T. D. Visser, B. Demeulenaere, J. Haes, D. Lenstra, R. Baets, and H. Blok, J. Lightwave Technol. **14**, 885 (1996).
13. J. S. Kanger, V. Subramaniam, P. H. J. Nederkoorn, and A. Ymeti, in *Advanced Photonic Structures for Biological and Chemical Detection*, X. Fan, ed. (Springer, 2009), pp. 265–295.
14. B. E. A. Saleh and M. C. Teich, *Fundamentals of Photonics* (Wiley, 1991).

PAPER III

Nanoimprint fabrication of slot waveguides

In: Photonics Journal 5(2), pp. 2200808.

IEEE Photonics Journal
An IEEE Photonics Society Publication

Open Access

Nanoimprint Fabrication of Slot Waveguides

Volume 5, Number 2, April 2013

Marianne Hiltunen
Esa Heinonen
Jussi Hiltunen
Jarkko Puustinen
Jyrki Lappalainen
Pentti Karioja

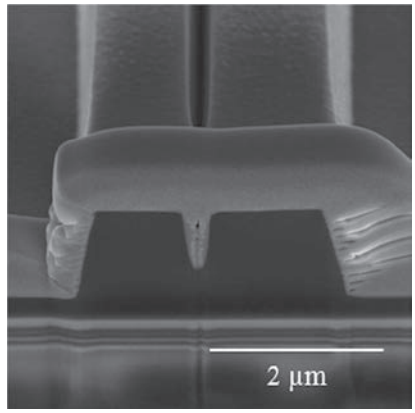

DOI: 10.1109/JPHOT.2013.2251876
1943-0655/$31.00 ©2013 IEEE

Nanoimprint Fabrication of Slot Waveguides

Marianne Hiltunen,[1] Esa Heinonen,[2] Jussi Hiltunen,[1] Jarkko Puustinen,[3] Jyrki Lappalainen,[3] and Pentti Karioja[1]

[1]VTT Technical Research Centre of Finland, 90570 Oulu, Finland
[2]Center of Microscopy and Nanotechnology, University of Oulu, 90014 Finland
[3]Department of Electrical and Information Engineering, Microelectronics and Materials Physics Laboratories, University of Oulu, 90014 Finland

DOI: 10.1109/JPHOT.2013.2251876

Manuscript received February 5, 2013; revised March 1, 2013; accepted March 2, 2013. Date of publication March 8, 2013; date of current version March 15, 2013. This work was supported by the Finnish Academy under Grants 137331 (M. H.) and 133814 (J. H.). Corresponding author: M. Hiltunen (e-mail: Marianne.Hiltunen@vtt.fi).

Abstract: A nanoimprint mold for optical waveguide applications was fabricated by combining photolithography and focused ion beam (FIB) milling. The feasibility of the proposed method was demonstrated by imprinting 15-mm-long Y-branch waveguides, which had nanoscale slots embedded in one arm. Structural analysis of the FIB milled region showed surface roughness values below 2.5 nm. Characterization of the fabricated waveguides proved that 44% of the optical power was transmitted through the slot-embedded waveguide arm. Operation of slot waveguide was demonstrated at a wavelength of 1305 nm using Young interferometer devices.

Index Terms: Waveguides, subwavelength structures, fabrication and characterization.

1. Introduction

In nanoimprint lithography (NIL), the surface–relief features of a mold are transferred to a polymer resist by mechanical replication [1]. Pattern deformation can be based on thermal embossing or ultraviolet (UV) curing of a liquid-phase polymer. Large-area patterns in a nanoimprint mold are typically processed lithographically, for example, using UV-photolithography or electron-beam lithography, followed by a reactive ion etching step. The direct writing focused ion beam (FIB) method has been used to fabricate small-area stamps for NIL or for repairing NIL stamps [2], [3]. FIB writing is a favorable direct writing method in terms of resolution and accuracy. The resolution in the sub-10-nm range is achievable with FIB milling. However, the processing time is the main limitation of the method. The processing times of dimensions above 100 μm begin to become unacceptably high [4].

It is typical of the integrated optical devices that the length of the waveguides is in the order of centimeters. Due to the replication nature of the imprinting, the quality of the mold has to be very high, particularly when fabricating long waveguides with good transmission properties. The smoothness of the patterns, in particular, is of great importance in optical waveguide devices. Photolithography has been shown to be a good option for preparing molds for the imprint fabrication of long waveguides with low surface roughness [5], [6]. However, feature sizes in the shadow-mask photolithography method are restricted by the wave diffraction, and therefore, this method is applicable to fabricate micron-scale and larger features. In modern integrated optics, there is an increasing need for embedding nanoscale structures in waveguides. For example, nanoscale structures can manipulate

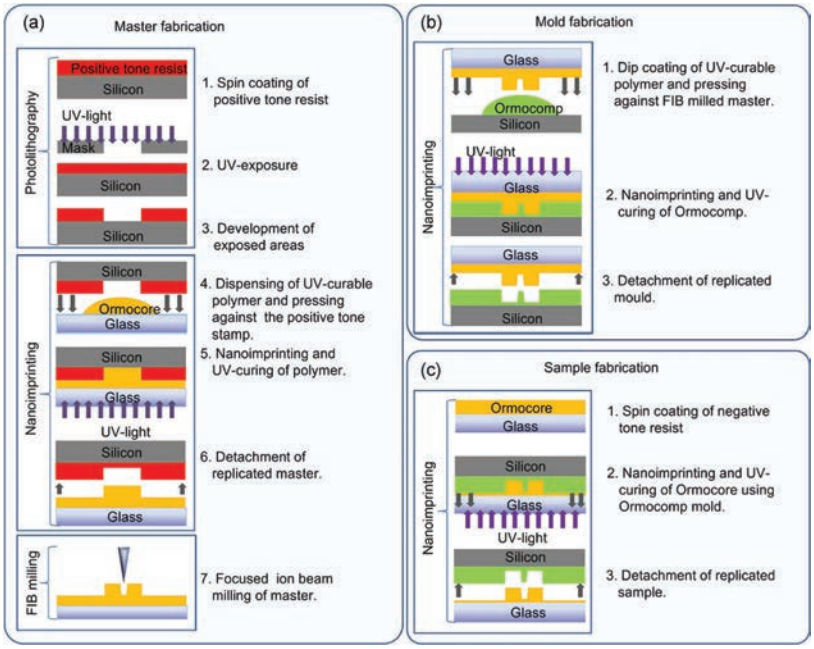

Fig. 1. Main fabrication steps to make nanoslot waveguide. (a) Master fabrication consists of photolithography, nanoimprint, and FIB milling steps. (b) Mold is fabricated by nanoimprinting UV-curable polymer. (c) Nanoslot waveguide is replicated by nanoimprinting mold on spin-coated polymer.

the propagation of the light in a waveguide or influence light coupling properties [7], [8]. For instance, gratings have been used to establish the light coupling into or out from the waveguide. To enhance the light interaction with the ambient, a waveguide structure consisting of a few hundred nanometer-wide slots has been demonstrated [9], [10]. The nanoslot waveguide configuration has an attractive property in simultaneously guiding the light propagation and maintaining a strong light–ambient interaction. This makes various applications possible, for example, optical trapping and sensing [11], [12].

The motivation for this paper was to investigate the fabrication of a NIL master mold for waveguide applications by combining a large-area photolithography process and nanoscale FIB milling. The applicability of modifying a NIL master mold using FIB milling was demonstrated by fabricating centimeter-long Y-branch waveguide devices, which include a nanoscale wide slot embedded in one arm of the branch. Furthermore, the applicability of fabricated waveguide structures for sensor applications was investigated.

2. Simulation and Fabrication

The fabrication of the samples consists of the following three main phases: 1) making the master; 2) fabrication of the replication mold; and 3) nanoimprinting of the waveguide sample. The structures with a size below the diffraction limit were built in the master by combining photolithography, nanoimprint, and FIB milling.

The fabrication of the master involved three steps, which are illustrated in Fig. 1(a). First, the positive tone resist was spin coated on a silicon substrate. The thickness of the positive tone resist

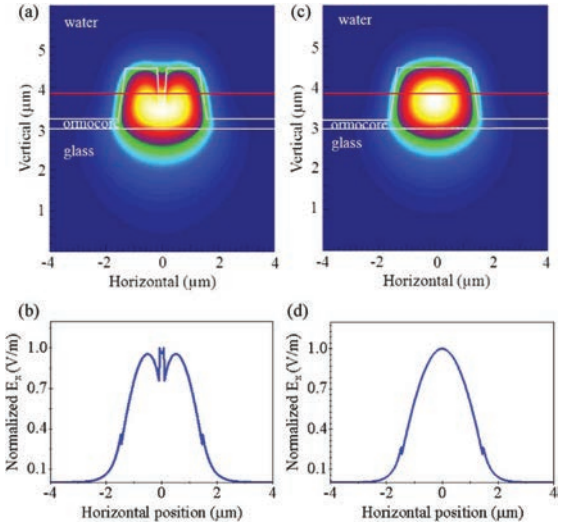

Fig. 2. (a) Electric field E_x profile of TE-mode in the slot waveguide. (b) Cross-sectional plot of the E_x field of TE mode indicated as a red line in (a). (c) Electric field E_x profile of TE-mode in the ridge waveguide. (d) Cross-sectional plot of the E_x field of TE mode indicated as a red line in (c).

layer, which is about 1.3 μm, determines the height of the final waveguide ridge. The resist was photolithographically patterned in order to produce a stamp by exposing UV-light through a shadow mask and removing the exposed areas with a developer. Next, the negative tone resist, i.e., Ormocore, was dispensed on a borofloat glass substrate, and the pattern on the positive tone stamp was replicated on it by imprinting and UV-curing Ormocore resist. The replicated Ormocore master was detached and hardened by post-baking it for 1 h at 130 °C. Then, conductive aluminum coating was vacuum evaporated on the master in order to avoid charge-up of the surface during FIB milling. As the last phase in the master fabrication, nanoscale slots were milled into waveguide templates using the FIB system (FEI Helios Dualbeam 600). The beam current during the milling was 28 pA, and the beam voltage was 30 kV. Three different slot lengths (40, 80, and 120 μm) were milled into the middle of one arm of the Y-branch waveguide master. FIB milling was followed by the removal of the aluminum coating with 10% NaOH solution.

The master was identical with the sample. Therefore, the mold for the sample fabrication was replicated from the master. The mold fabrication phase is shown in Fig. 1(b). First, the master was treated with an antiadhesion coating of (1,1,2,2 H perfluorooctyl)-trichlorosilane. The master was replicated by dispensing resist, Ormocomp, on the silicon wafer, imprinting and UV-curing the replicated mold. The Ormocomp mold utilized to fabricate actual waveguides was released from the master and treated with the antiadhesion coating previously described.

The waveguide sample fabrication illustrated in Fig. 1(c) was started by spin-coating diluted Ormocore (Ormocore: Ma-T1050, 1:7) at 3000 r/min for 60 s on a borofloat glass wafer. The thinner (Ma-T1050) was evaporated at 85 °C for 40 min. Next, the Ormocomp mold was used to replicate the final Y-branch waveguide structures by nanoimprinting and UV-curing the Ormocore resist. Then, the patterned waveguides were hardened by post-baking for 1 h at 130 °C.

The waveguide mode field properties wfere calculated using the finite-element method (FEM) available in the PhotonDesign simulation software [13]. In the simulation, the ambient of the waveguide was considered to be water, which is a typical solution in a sensing application. The refractive indexes (RIs) in the simulation were 1.458 for the borofloat glass wafer, 1.54 for Ormocore, and 1.33 for water at the wavelength of 1305 nm that was used [14]. Fig. 2(a) and (c) shows the lateral electric field E_x distributions of transverse electric (TE) mode in the slot and ridge

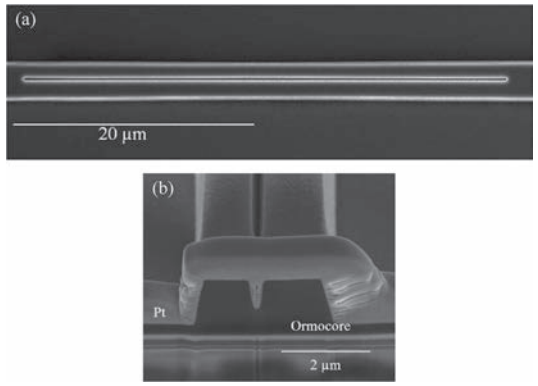

Fig. 3. (a) SEM image from the top of fabricated slot waveguide. (b) Cross-sectional SEM image of the slot part of the waveguide.

waveguides, respectively. The waveguide dimensions for the calculation were achieved from the scanning electron microscope (SEM) image in Fig. 3(b). As shown in Fig. 2(a), the optical field partly propagates in the medium in the slot. The horizontal cross-sectional plots of the E_x fields shown in Fig. 2(b) and (d) illustrate that the maximum of the optical field locates in the water in the slot waveguide and in the core of the ridge waveguide. The E_x field is slightly enhanced in the slot region confirming the slot mode operation. However, this enhancement is low compared with the enhancement achievable with high-index-contrast slot waveguide structures [9].

The interaction of the optical mode with the water ambient in the slot and ridge waveguides was compared by calculating the filling factor for both geometries with the equation

$$f_w = \frac{\int\limits_w P_z(a)da}{\int\limits_{\infty} P_z(a)da}. \tag{1}$$

In (1), $P_z(a)$ is a time-averaged Poynting vector, and the numerator is integral over the water region W [15]. The filling factors for a slot waveguide and a ridge waveguide with the same dimensions are 5.1% and 2.5%, respectively. This shows that the optical field of the slot waveguide interacts more with the ambient than the optical field of the ridge waveguide.

The sensitivity of the waveguide against the ambient RI change is often determined as a slope of the linear regression $\Delta n_{mode}/\Delta n_a$, where Δn_{mode} is the modal effective RI change, and Δn_a is the RI change of the ambient [16]. In Fig. 4, the effective RI changes of TE mode in a slot waveguide and a ridge waveguide against the ambient RI are plotted. The ambient RI is shifted from 1.32 to 1.33. Calculated sensitivities are 0.054 and 0.026 for the slot and ridge waveguides, respectively.

3. Characterization

The characterization covered the analysis of the structural and functional properties. The surface roughness of the FIB milled section was determined with an atomic force microscope (AFM). Waveguide transmission measurement was used for optical characterization of the fabricated waveguides. Furthermore, the operation of the Y-branches in interferometric measurement was demonstrated.

Fig. 3(a) shows the SEM image of the fabricated slot waveguide from the top. The horizontal position of the slot in the ridge is constant through the overall length of 40 μm. The width of the photolithography determined ridge is 3 μm. The corresponding cross-sectional SEM image of the slot region is shown in Fig. 3(b). The slot depth is 830 nm, and the width at the top is 340 nm,

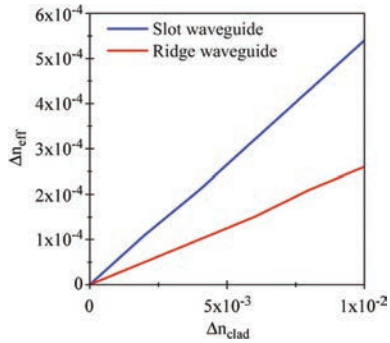

Fig. 4. Effective RI change of TE mode plotted against the RI change of the ambient.

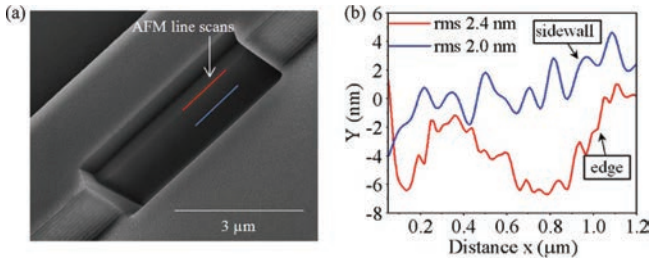

Fig. 5. (a) SEM image of the FIB milled part of the waveguide ridge. The red and blue lines indicate the parts for AFM analysis. (b) Roughness plot of the edge and sidewall region indicated as red and blue lines in (a).

narrowing toward the bottom with a 6.5° angle. The height of the ridge is 1.3 μm. The imprint fabrication method produces a residual layer underneath the replicated pattern. With the process parameters used, the thickness of the residual layer in this paper is about 200 nm.

3.1. Analysis of FIB Milling

In order to investigate the roughness of the FIB milled section, a ridge of the waveguide was milled with FIB using the same parameters as in the master fabrication. The SEM image of the ridge of the waveguide with the FIB milled part is shown in Fig. 5(a). The edge and the sidewall of milled surfaces look smooth. The roughness of the FIB milled part was analyzed by AFM (Veeco Dimension 3100). The root mean square roughness values of the FIB milled edge and the sidewall indicated as a red and blue plot in Fig. 5(b) were 2.4 and 2.0 nm, respectively. Such a small roughness of the edge and the sidewall suggests that FIB milling is a good tool for modifying polymeric molds for waveguides applications.

3.2. Optical Characterization

Transmission of fabricated Y-branch waveguides was analyzed in order to estimate the performance of the slot-embedded waveguide and to evaluate their usability in sensing applications. The transmission measurement setup is illustrated in Fig. 6(a). A laser source operating at a wavelength of 1305 nm was coupled to the polarization-maintaining tapered fiber. The polarization was adjusted with a fiber-optic polarization controller, and the polarization state was verified using an

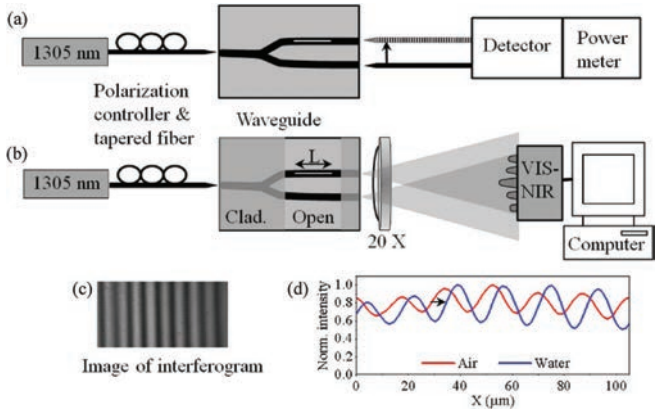

Fig. 6. Schematic of optical characterization methods. (a) Setup for measuring waveguide transmission. (b) Setup for measuring interference of Young interferometry structure. (c) Fringe pattern generated at 700 μm distance on visible-infrared (VIS-IR) camera. (d) Intensity distribution of the interferogram.

external polarizer prior the transmission measurement. The input fiber and the similar output fiber were optimally aligned with the waveguide in order to produce maximum light coupling into the waveguide input facet and from both output arms. The maximum power transmission through the waveguide was measured for both TE and transverse magnetic (TM) polarizations. The average transmissions of eight measured Y-branches were referenced with the fiber-to-fiber power transmission without the waveguide sample between the fibers. The lengths of the Y-branch waveguides were 15 mm. For TE polarization, the average transmission of 31% and 39% were obtained for the slot and reference ridge waveguide arms, respectively. Correspondingly, the average transmission values of 28% and 35% were obtained for TM polarization. These values include the material loss (0.23 dB/cm), coupling losses from the fibers, and the mode coupling loss both in the Y-branch and in the ridge-slot-ridge waveguide interface [14]. From the transmission values measured, the division ratio of the optical power in the slot and ridge waveguide arms was calculated to be 44% and 56%, respectively. The lengths of the slots (40, 80, and 120 μm) in the measured waveguides are too short to enable us to distinguish the transmission loss of the slot waveguide from the other attenuation factors. However, the measured transmission values indicate that the slot waveguide possess good transmission properties.

3.3. Experimental Verification of Slot Mode

The Y-branch waveguide operates as a Young interferometer. The operation is based on the phase difference produced by the two different waveguide arms. One arm of the Young waveguide interferometer was the reference arm, and the other arm consists of a slot with a length of 40, 80, or 120 μm. The operational performance of the Young interferometers with slot waveguides was experimentally verified using the measurement arrangement sketched in Fig. 6(b). The portion of the reference and the sensing arm experiencing the RI variation of the ambient must have the same length in the interference measurement setup used. Therefore, a waveguide sample with an overcladding layer of Ormostamp with a RI of 1.507 was fabricated. The Ormostamp layer was opened for 524 μm $\pm$ 5 μm by using UV-photolithography. The length of the opening determining the sensing area was measured using a white-light interferometer (Wygo, NT3300). The interference measurement was performed for the TE and TM polarizations. The interference pattern was captured with VIS-NIR camera. The output beams of the waveguides were collected by placing a microscope objective with 20$\times$ magnification after the waveguides. Then, the microscope objective was moved 0.7 mm away from the focus in order to acquire the far-field fringe pattern with

TABLE 1

Measured and simulated phase shifts

Device/w Slot length (μm)	Measured phase shift TE polarization	Simulated phase shift TE polarization	Measured phase shift TM polarization	Simulated phase shift TM polarization
0 reference	0.00±0.01	0	0.00±0.01	0
40	1.10±0.01	1.1	0.84±0.01	0.7
80	2.66±0.01	2.3	1.91±0.01	1.4
120	3.68±0.01	3.4	2.32±0.01	2.1

parallel vertical lines. Fig. 6(c) shows an interferogram image on the VIS-NIR camera. The interferogram pattern was video recorded, whereas a water droplet was applied on the opening of Young interferometer. The measured intensity distribution of the interferogram of the Young waveguide structure with a 80-μm-long slot in one arm both with and without water is shown in Fig. 6(d). The phase difference shift is indicated as an arrow in Fig. 6(d).

The intensity of the interferogram picture can be described by the equation

$$I = I_1 + I_2 + 2\sqrt{I_1 I_2}\cos(\Delta\varphi - \delta) \tag{2}$$

where I_1 and I_2 are the intensities of two interfering waveguide beams, and $\Delta\varphi$ is the phase difference of the two beams [17]. The higher fraction of the mode field propagates in the slot and ambient in the slot waveguide, than in the ambient of the ridge reference waveguide. This causes a difference of the effective RI change between the ridge reference arm and the slot waveguide arm at length L of the slot, producing the additional phase shift δ in the fringe pattern. This additional phase shift can be calculated by the equation

$$\delta = 2\pi \frac{L}{\lambda_0} \Delta n_{eff} \tag{3}$$

where $\lambda_0 = 1305$ nm is the wavelength in vacuum and $\Delta n_{eff} = \delta n_{eff}/\delta n_a$ is derivate of the effective RI change in two waveguide arms as the RI of ambient index n_a changes [16]. The phase shift of interference pattern was calculated at the respective spatial period using a fast Fourier transform.

Phase shifts measured and simulated for TE and TM polarizations are shown in Table 1. For the simulation, the effective RI both with air and water ambient in the slot and ridge waveguides were calculated using FEM. The waveguide dimensions for the mode calculation were derived from the cross-sectional SEM image in Fig. 3(b). The effective RI was inserted into equation (2) to calculate the simulated phase shift values. The mode power fraction of TE mode in the slot is higher than in TM mode, causing a bigger phase shift with the TE polarization. The correlation between the measured and the simulated phase shifts is relatively good. The measured values are actually a little higher than the simulated ones. The potential factors for the difference between the measurement and simulation are estimated to be attributed to local waveguide variations such as the residual layer thickness and slot dimension variation.

4. Conclusion

In this paper, we have demonstrated that the FIB milling tool can be used to pattern nanometer scale slot features into the large-dimensional polymeric nanoimprint master mold. SEM and AFM investigations proved that FIB milling provides low surface roughness required in photonic devices. We have also showed that slot waveguides can be nanoimprint fabricated using the FIB modified molds. Proper slot mode propagation was confirmed by interferometric measurements at a wavelength of 1305 nm. Optical analysis also showed that the fabricated slot waveguides possessed good transmission properties.

References

[1] J. L. Guo, "Nanoimprint lithography: Methods and material requirements," *Adv. Mater.*, vol. 19, no. 4, pp. 495–513, Feb. 2007.

[2] H.-W. Sun, J.-Q. Liu, D. Chen, and P. Gu, "Optimization and experimentation of nanoimprint lithography based on FIB fabricated stamp," *Microelectron. Eng.*, vol. 82, no. 2, pp. 175–179, Oct. 2005.

[3] H. D. Wanzenboeck, S. Waid, E. Bertagnolli, M. Muehlberger, I. Bergmair, and R. Schoeftner, "Nanoimprint lithography stamp modification utilizing focused ion beams," *J. Vac. Sci. Technol. B, Microelecton, Nanom. Struct.*, vol. 27, no. 6, pp. 2679–2685, Nov. 2009.

[4] S. Reyntjens and R. Puers, "A review of focused ion beam application in microsystem technology," *J. Micromech. Microeng.*, vol. 11, no. 4, pp. 287–300, Jul. 2001.

[5] J. Hiltunen, M. Hiltunen, J. Puustinen, J. Lappalainen, and P. Karioja, "Fabrication of optical waveguides by imprinting: Usage of positive tone resist as a mould for UV-curable polymer," *Opt. Exp.*, vol. 17, no. 25, pp. 22 813–22 822, Dec. 2009.

[6] M. Wang, J. Hiltunen, S. Uusitalo, J. Puustinen, J. Lappalainen, P. Karioja, and R. Myllylä, "Fabrication of optical inverted-rib waveguides using UV-imprinting," *Microelectron. Eng.*, vol. 88, no. 2, pp. 175–178, Feb. 2011.

[7] M. Hiltunen, L. Dal Negro, N.-N. Feng, L. C. Kimeling, and J. Michel, "Modeling of aperiodic fractal waveguide structures for multifrequency light transport," *J. Lightwave Technol.*, vol. 25, no. 7, pp. 1841–1847, Jul. 2007.

[8] S. Grego, J. R. McDaniel, and B. Stoner, "Wavelength interrogation of grating-based optical biosensors in the input coupler configuration," *Sens. Actuators B, Chem.*, vol. 131, no. 2, pp. 347–355, May 2008.

[9] Q. Xu, V. R. Almeida, R. R. Panepucci, and M. Lipson, "Experimental demonstration of guiding and confining light in nanometer-size low-refractive-index material," *Opt. Lett.*, vol. 29, no. 14, pp. 1626–1628, Jul. 2004.

[10] M. Hiltunen, J. Hiltunen, P. Stenberg, J. Petäjä, E. Heinonen, P. Vahimaa, and P. Karioja, "Polymeric slot waveguide at visible wavelength," *Opt. Lett.*, vol. 37, no. 21, pp. 4449–4451, Nov. 2012.

[11] A. H. J. Yang, S. D. Moore, B. S. Schmidt, M. Klug, M. Lipson, and D. Ericson, "Optical manipulation of nanoparticles and biomolecules in sub-wavelength slot waveguides," *Nature*, vol. 457, no. 7225, pp. 71–75, Jan. 2009.

[12] C. A. Barrios, "Optical slot-waveguide based biochemical sensors," *Sensors*, vol. 9, no. 6, pp. 4751–4765, Jun. 2009.

[13] FimmWave Software Photon Design Ltd., Oxford, U.K.

[14] Datasheet for Ormocore, Microresist Technology. [Online]. Available: http://www.microresist.de/products/ormocers/pdf/pi_ormocore_clad_en_07062201_ls_neu.pdf

[15] T. D. Visser, B. Demeulenaere, J. Haes, D. Lenstra, R. Baets, and H. Blok, "Confinement and modal gain in dielectric waveguides," *J. Lightwave Technol.*, vol. 14, no. 5, pp. 885–887, May 1996.

[16] X. Fan, *Advanced Photonic Structures for Biological and Chemical Detection*. New York, NY, USA: Springer-Verlag, 2009.

[17] B. E. A. Saleh and M. C. Teich, *Fundamentals of Photonics*. New York, NY, USA: Wiley, 1991.

PAPER IV

Polymeric slot waveguide interferometer for sensor application

In: Optics Express 22(6), pp. 7229–7237.

Polymeric slot waveguide interferometer for sensor applications

Marianne Hiltunen,[1*] Jussi Hiltunen,[1] Petri Stenberg,[2] Sanna Aikio,[1] Lauri Kurki,[1] Pasi Vahimaa,[2] and Pentti Karioja[1]

[1]*VTT Technical Research Centre of Finland, Kaitoväylä 1, 90570 Oulu, Finland*
[2] *Institute of Photonics, University of Eastern Finland, P.O. Box 111, 80101 Joensuu, Finland*
[*]*Marianne.Hiltunen@vtt.fi*

Abstract: A refractive index sensor based on slot waveguide Young interferometer was developed in this work. The interferometer was fabricated on a polymer platform and operates at a visible wavelength of 633 nm. The phase shift of the interference pattern was measured with various concentrations of glucose-water solutions, utilizing both TE and TM polarization states. The sensor was experimentally observed to detect a refractive index difference of 6.4×10^{-6} RIU. Furthermore, the slot Young interferometer was found to compensate for temperature variations. The results of this work demonstrate that high performance sensing capability can be obtained with a polymeric slot Young interferometer, which can be fabricated by a simple molding process.

OCIS codes: (130.3120) Integrated optics devices; (130.5460) Polymer waveguides; (130.6010) Sensors; (120.3180) Interferometry.

References and links

1. X. Fan, I. M. White, S. I. Shopova, H. Zhu, J. D. Suter, and Y. Sun, "Sensitive optical biosensors for unlabeled targets: A Review," Anal. Chim. Acta **620**(1-2), 8–26 (2008).
2. P. V. Lambeck, "Integrated optical sensors for the chemical domain," Meas. Sci. Technol. **17**(8), R93–R116 (2006).
3. R. Bruck, E. Melnik, P. Muellner, R. Hainberger, and M. Lämmerhofer, "Integrated polymer-based Mach-Zehnder interferometer label-free streptavidin biosensor compatible with injection molding," Biosens. Bioelectron. **26**(9), 3832–3837 (2011).
4. K. De Vos, I. Bartolozzi, E. Schacht, P. Bienstman, and R. Baets, "Silicon-on-Insulator microring resonator for sensitive and label-free biosensing," Opt. Express **15**(12), 7610–7615 (2007).
5. A. Ksendzov and Y. Lin, "Integrated optics ring-resonator sensors for protein detection," Opt. Lett. **30**(24), 3344–3346 (2005).
6. F. Prieto, B. Sep lveda, A. Calle, A. Llobera, C. Dominguez, A. Abad, A. Montoya, and L. M. Lechuga, "An integrated optical interferometric nanodevice based on silicon technology for biosensor applications," Nanotechnology **14**(8), 907–912 (2003).
7. A. Ymeti, J. S. Kanger, J. Greve, P. V. Lambeck, R. Wijn, and R. G. Heideman, "Realization of a multichannel integrated Young interferometer chemical sensor," Appl. Opt. **42**(28), 5649–5660 (2003).
8. J. J. Hu, N. Carlie, N. N. Feng, L. Petit, A. Agarwal, K. Richardson, and L. Kimerling, "Planar waveguide-coupled, high-index-contrast, high-Q resonators in chalcogenide glass for sensing," Opt. Lett. **33**(21), 2500–2502 (2008).
9. L. Wang, J. Ren, X. Han, T. Claes, X. Jian, P. Bienstman, R. Baets, M. Zhao, and G. Morthier, "A label-free optical biosensor built on a low-cost polymer platform," Photonics Journal **4**, 920–930 (2012).
10. R. Gupta and N. J. Goddard, "A polymeric waveguide resonant mirror (RM) device for detection in microfluidic flow cells," Analyst (Lond.) **138**(11), 3209–3215 (2013).
11. M. Wang, J. Hiltunen, C. Liedert, S. Pearce, M. Charlton, L. Hakalahti, P. Karioja, and R. Myllylä, "Highly sensitive biosensor based on UV-imprinted layered polymeric-inorganic composite waveguides," Opt. Express **20**(18), 20309–20317 (2012).
12. C. Y. Chao, W. Fung, and L. J. Guo, "Polymer microring resonator for biochemical sensing applications," J. of Selected Topics in Quantum Electronics. **12**(1), 134–142 (2006).
13. Q. Xu, V. R. Almeida, R. R. Panepucci, and M. Lipson, "Experimental demonstration of guiding and confining light in nanometer-size low-refractive-index material," Opt. Lett. **29**(14), 1626–1628 (2004).
14. F. Dell'Olio and V. M. N. Passaro, "Optical sensing by optimized silicon slot waveguides," Opt. Express **15**(8), 4977–4993 (2007).
15. V. M. N. Passaro, F. Dell'olio, C. Ciminelli, and M. N. Armenise, "Efficient chemical sensing by coupled slot SOI waveguides," Sensors (Basel) **9**(2), 1012–1032 (2009).

#202021 - $15.00 USD Received 28 Nov 2013; revised 11 Mar 2014; accepted 11 Mar 2014; published 20 Mar 2014

16. C. C. F. Carlborg, K. B. Gylfason, A. Kaźmierczak, F. Dortu, M. J. Bañuls Polo, A. Maquieira Catala, G. M. Kresbach, H. Sohlström, T. Moh, L. Vivien, J. Popplewell, G. Ronan, C. A. Barrios, G. Stemme, and W. van der Wijngaart, "A packaged optical slot-waveguide ring resonator sensor array for multiplex label-free assays in labs-on-chips," Lab Chip **10**(3), 281–290 (2010).
17. C. A. Barrios, K. B. Gylfason, B. Sánchez, A. Griol, H. Sohlström, M. Holgado, and R. Casquel, "Slot-waveguide biochemical sensor," Opt. Lett. **32**(21), 3080–3082 (2007).
18. K. B. Gylfason, C. F. Carlborg, A. Kaźmierczak, F. Dortu, H. Sohlström, L. Vivien, C. A. Barrios, W. van der Wijngaart, and G. Stemme, "On-chip temperature compensation in an integrated slot-waveguide ring resonator refractive index sensor array," Opt. Express **18**(4), 3226–3237 (2010).
19. P. Bettotti, A. Pitanti, E. Rigo, F. De Leonardis, V. M. N. Passaro, and L. Pavesi, "Modeling of slot waveguide sensors based on polymeric materials," Sensors (Basel) **11**(12), 7327–7340 (2011).
20. H. Sun, A. Chen, and L. R. Dalton, "Enhanced evanescent confinement in multiple-slot waveguides and its application in biochemical sensing," Photonics Journal **1**(1), 48–57 (2009).
21. M. Hiltunen, E. Heinonen, J. Hiltunen, J. Puustinen, J. Lappalainen, and P. Karioja, "Nanoimprint fabrication of slot waveguides," Photonics Journal **5**, 2200808 (2013).
22. M. Hiltunen, J. Hiltunen, P. Stenberg, J. Petäjä, E. Heinonen, P. Vahimaa, and P. Karioja, "Polymeric slot waveguide at visible wavelength," Opt. Lett. **37**(21), 4449–4451 (2012).
23. Ormocer datasheet, MicroResistsTechnology.
24. FimmWave Software, Photon Design Ltd, Oxford, UK.
25. A. F. Fucaloro, Y. Pu, K. Cha, A. Williams, and K. Conrad, "Partial molar volumes and refractions of aqueous solutions of fructose, glucose, mannose and sucrose at 15.00, 20.00 and 25.00°C," J. Solution Chem. **36**(1), 61–80 (2007).
26. M. Wang, J. Hiltunen, C. Liedert, L. Hakalahti, and R. Myllylä, "An integrated Young interferometer based on UV-imprinted polymer waveguides for label-free biosensing applications," J. Europ. Opt. Soc. Rap. Public **7**, 12019 (2012).
27. M. Daimon and A. Masumura, "Measurement of the refractive index of distilled water from the near-infrared region to the ultraviolet region," Appl. Opt. **46**(18), 3811–3820 (2007).

1. Introduction

Integrated optical sensors, which utilize the refractive index change as the sensing transduction signal, enable sensitive, real-time, and label-free detection [1–3]. Various planar waveguide sensor geometries has been demonstrated with inorganic dielectrics such as SOI [4], Si_xN_y [5–7], and chalcogenide glass films [8]. In the sensor applications, the regeneration of the sensor between the analyses might be a very complicated procedure. Therefore, reducing the cost of the devices is desired, to provide potential for the use of disposable sensors. An opportunity to apply simple and low-cost fabrication techniques, for example nanoimprinting, makes polymers an attractive option as a sensor platform. In addition, polymers and composite polymers have several attractive features, such as biocompatibility and refractive index tunability, which have attracted interest for using them in sensor applications [9–12].

A slot waveguide structure is able to simultaneously guide the light propagation and confine the light in the low-refractive-index material filling the slot, and therefore the structure enables strong light-ambient material interaction. This characteristic makes the slot waveguide an attractive structure for sensor applications. Originally, the slot waveguide structure was demonstrated for a high refractive index contrast silicon-silica configuration [13]. Sensing properties of silicon slot waveguides have been theoretically investigated [14, 15]. Experimental work on sensors based on a slot waveguide has been mainly focused on Si_3N_4 microring resonators, which have been demonstrated to operate both for homogenous refractive index and surface-sensing applications at near-infrared wavelengths [16, 17]. A ring-resonator constructed from a slot waveguide has also been demonstrated to compensate for temperature variation during measurement [18]. In sensing applications, a visible wavelength is usually preferable. Transparency at visible wavelengths and the potential low-cost fabrication methods have given rise to research on the slot waveguides of polymers [19–22]

The motivation for the present work was to develop a low-cost sensor with reduced temperature dependency. The potential cost reduction is enabled by the usage of a room temperature nanoimprint molding method for fabricating polymeric slot waveguide sensors. In principle, polymer substrate can also be used instead of oxidized silicon. However, this would require that the surface has low roughness and waving, and the refractive index of the

#202021 - $15.00 USD Received 28 Nov 2013; revised 11 Mar 2014; accepted 11 Mar 2014; published 20 Mar 2014

substrate is low enough for this waveguide structure. The sensitivity of the developed sensor was investigated with bulk refractive index changes of glucose-water solutions. Finally, the temperature dependency of the proposed sensor structure was evaluated.

2. Young interferometer sensor fabrication and characterization

2.1. Fabrication

The schematic image in Fig. 1 illustrates the principle of the slot Young interferometer used in this work. It consists of a Y-splitter ridge waveguide in which one arm has a region with a slot waveguide. The 10 µm thick overcladding layer of Ormostamp defines the interaction area between the analyte and waveguides. The preparation of the Young interferometer waveguide started with the master fabrication on a silicon substrate. The details of the master fabrication are described elsewhere [22]. The master was treated with an anti-adhesion coating of (1,1,2,2 H perfluorooctyl)-trichlorosilane. Due to the fact that the master consists of ridges, it had to be replicated in order to make the mold for the final waveguide fabrication. The master was replicated by spin coating Ormostamp on the glass wafer. The master and Ormostamp glass wafer stack was pressed with 1 bar pressure in nanoimprint equipment (Obducat Eitre 6) and exposed with UV-light for 2 minutes. The Ormostamp mold utilized to fabricate the actual waveguides was released from the master and treated with the anti-adhesion coating described above.

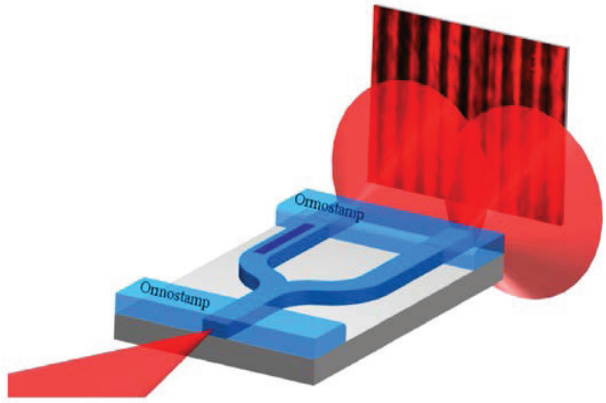

Fig. 1. Schematic image of the slot Young interferometer and the measurement set-up. The left arm includes a slot waveguide part, which produces the phase difference between the waveguide arms, and the right arm acts as a reference ridge waveguide.

The slot interferometer was fabricated using UV-curable hybrid polymers, Ormocers, from Micro resist technology GmbH [23]. The waveguide replication process was started by spin coating diluted Ormocore (Ormocore: Ma-T1050, 1:7) on a silicon wafer with a 2 µm thick thermal oxide layer acting as an undercladding layer for the waveguides. The solvent (Ma-T1050) was evaporated at 130°C for 10 minutes on a hot plate. For the waveguide replication, the Ormostamp glass mold was stacked up in contact with the Ormocore-coated wafer and pressed together in the nanoimprint equipment with 10 bar pressure, followed by a 2 minute UV expose. After the patterned waveguides were released from the mold, they were hardened by post-baking for one hour at 130°C on a hot plate. In order to isolate the non-sensing regions of the waveguides from the sensing window, and to protect the waveguides from contact with the fluid cell, an overcladding layer of Ormostamp was processed using photolithography. Negative tone Ormostamp was spin coated on the wafer. The Ormostamp was UV-exposed through a shadow mask and the unexposed Ormostamp was removed with acetone. It is to be noted that, once the mold is fabricated, it can be used several times to replicate waveguides. Therefore, further sensor chips can be fabricated by two simple

#202021 - $15.00 USD Received 28 Nov 2013; revised 11 Mar 2014; accepted 11 Mar 2014; published 20 Mar 2014

fabrication steps: nanoimprint lithography for waveguide replication and photolithography for overcladding patterning with loose alignment tolerances.

2.2. Theoretical analysis of the interferometer

The slot Young interferometer operation is based on the phase difference produced between the slot and the reference ridge waveguide arms. For proper interferometer operation, both interferometer arms have to support only one mode in the used polarization state. In the proposed geometry, both the slot arm and the ridge arm observe the change of the homogenous refractive index (RI) of the ambient material. The optical field in the slot waveguide interacts more with the ambient material than it does in the ridge waveguide. Therefore, the changes of the effective refractive index Δn_{eff} of the modes, in the slot waveguide and in the ridge waveguide, differ from each other as the ambient RI changes. In the simulation, effective RI, n_{eff}, of the ridge and the slot waveguide modes were calculated using the finite element method (FEM), available in the commercial simulation software Fimmwave [24]. The waveguide dimensions used in the simulation were obtained from the cross-section scanning electron microscope (SEM) images of the fabricated waveguides, shown in Fig. 2. The thickness of the residual layer of polymer outside the waveguide ridges was approximately 140 nm. The width and the height of the waveguide, and the width of the slot in the slot waveguide, were approximately 700 nm, 600 nm, and 140 nm, respectively. For the tolerance analysis, the slot width was varied from 120 nm to 160nm, and the residual polymer layer thickness was varied from 100 nm to 180 nm. The maximum deviation is shown in parentheses after the nominal response value. The following refractive indices were used in the simulations: waveguide core n_{co} = 1.553 (Ormocore) and substrate n_{subst} = 1.457 (SiO_2) as a sensor structure, deionized water n_{DI} = 1.33299 and 1% (mol/L) concentration of glucose-water solution n_{GL} = 1.33427 as ambient materials [23, 25]. The change of the ambient material from DI water to 1% glucose-water solution caused an effective RI change, Δn_{eff}, of 1.52×10^{-4} (2×10^{-5}) in the slot waveguide, and 8.27×10^{-5} (7×10^{-6}) in the ridge waveguide for the transverse electric (TE) polarization state. For the transverse magnetic (TM) polarization state, Δn_{eff} was 1.44×10^{-4}(2×10^{-5}) and 7.03×10^{-5} (1×10^{-5}), respectively. It can be noted that the slot waveguide is more sensitive than the ridge waveguide to the bulk RI change in both polarization states. Although Δn_{eff} in the slot waveguide is higher at TE polarization, the total difference in Δn_{eff} between the ridge and the slot waveguide is slightly higher with TM polarization. Therefore, the polymeric slot Young interferometer allows a choice of either TE or TM polarization.

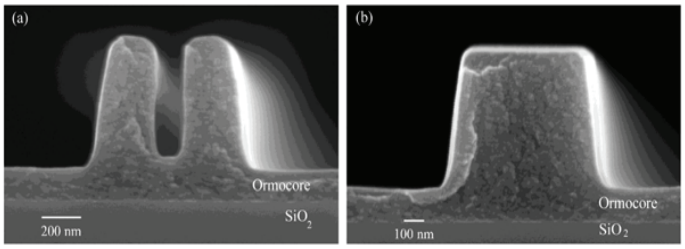

Fig. 2. SEM image of the cross section of a) the sensing slot waveguide, and b) the reference ridge waveguide.

2.3. Waveguide characterization and sensor performance

Stabilized laser operating at 633 nm was used as a visible light source. The quarter-wave plate, placed after the laser, converted the linearly polarized laser light into circularly polarized light. The TE or TM polarization state was adjusted with a polarizer installed between the quarter-wave plate and the device. The laser beam was coupled to the waveguide through a lens. At the output facet of the waveguide, a 40X objective collected and magnified the image of the waveguide modes. The image was captured with a CMOS camera

#202021 - $15.00 USD Received 28 Nov 2013; revised 11 Mar 2014; accepted 11 Mar 2014; published 20 Mar 2014

(PixeLink). A loss in the slot waveguide was deduced from the images of the normalized mode intensity profiles of the ridge waveguide and a waveguide consisting of either a 5 mm or a 10-mm-long slot section. The intensity deviation between the two arms was measured to be below 20%. This value was obtained by comparing the output intensities of two identical waveguide arms (without slot structure). For the TM polarization state, a slot waveguide loss of 14 dB/cm was calculated by comparing the mode intensities of the ridge and the slot waveguide arms of these two slot lengths. This loss includes the coupling loss caused from the mode mismatching of the TM_{00}- modes in ridge and slot waveguide sections. The coupling loss, calculated with an overlap integral method between the TM_{00}- modes in ridge–slot–ridge interfaces, was 1 dB. The loss in the TE polarization state was measured to be 0.8 dB/cm higher than with the TM polarization state. The coupling loss of TE_{00}-modes in interfaces was calculated to be 1.6 dB. A substantial proportion of the modal optical field propagates at the slot edges. Therefore, the high loss in the slot waveguide is attributed to surface roughness of the slot edges.

For the bulk refractive index sensing measurements, glucose-water solutions (D-glucose, Sigma-Aldrich) of various molar concentrations (0.005%, 0.01%, 0.03%, 0.05%, 0.1%, 0.2% mol/L) were prepared. The bulk refractive index change, Δn_B, of the glucose-water solution with respect to deionized (DI) water was calculated based on empirical data from reference [25] at a temperature of 20°C:

$$\Delta n_B = 1.4014 \times \left(\frac{n_g}{n_{DI}} \right), \tag{1}$$

where n_g and n_{DI} are the amounts of substance of glucose and DI water, respectively.

For the homogenous refractive index measurement, a fluidic cell is placed on top of the sensor. The propagation mode profiles at the output facet of the sensor chip are shown in Fig. 3(a). The mode on the left has a lower intensity, which is mainly caused by the loss in a 5-mm-long slot waveguide section. Then the 40x objective lens was moved 1.35 mm away from

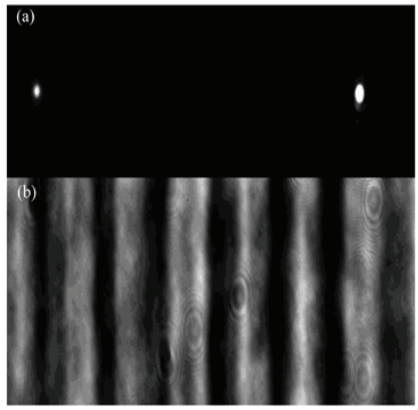

Fig. 3. a) Image captured at the end of the slot Young interferometer waveguide. The left mode intensity profile consists of a waveguide with a 5-mm-long slot section and the right mode intensity profile consist of a ridge waveguide. b) The interferogram generated at a 1.35 mm distance from the waveguide facet.

the waveguide facet focus in order to generate an interference fringe pattern, shown in Fig. 3(b). To evaluate the response of the sensor against the change of the bulk RI, the DI water and various concentrations of glucose-water solutions were applied to the sensing window of the device. To remove the influence of water absorption into the Ormocore during the measurement, the DI water was allowed to stand on the sample for several hours prior the measurement [11]. Liquids were pumped through the flow cell at a flow velocity of 250

#202021 - $15.00 USD Received 28 Nov 2013; revised 11 Mar 2014; accepted 11 Mar 2014; published 20 Mar 2014

μL/min using a syringe pump (Nexus 3000, Chemyx Inc.), and the interference fringe pattern images were recorded with a CMOS camera. The phase of each image at the respective spatial period was extracted using the two-dimensional Fast Fourier Transform (FFT) method. Continuous measurement of the water-glucose-water sequence as a function of time is shown in Fig. 4. The base of the phase shift continues to increase during the sequence, which is assumed to be caused by the accumulation of glucose molecules in the slot region. The slot waveguide sensors investigated in this work showed a different response compared to the inverted ridge waveguide used in reference [26]. Namely, the accumulation effect shown in Fig. 4 was not observed before with water-glucose analyte. Therefore, we believe that the accumulation effect observed in this work is attributed to new waveguide geometry. Although the sensor window is flushed with DI water before applying a new glucose solution, the phase does not return to the original base level. This also indicates that the accumulation of glucose molecules occurs in a nanoslot structure.

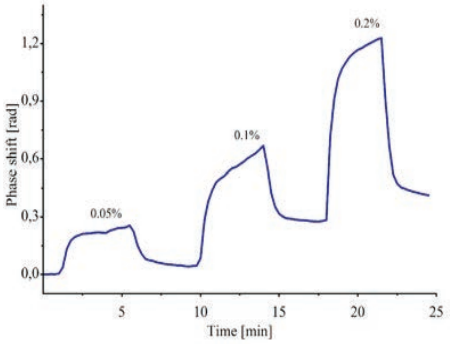

Fig. 4. The measured phase response at TM polarization for three different glucose concentrations, 0.05%, 0.1%, and 0.2%, ran continuously and was flushed with DI water after each addition of glucose-water solution.

For deducting the influence of the phase base drift caused by the glucose-water samples, the homogenous bulk RI measurement was repeated for each glucose-water solution separately, using both polarization states. The smallest measured glucose concentration of 0.005% induced a phase response of 0.04 rad at TM polarization. This glucose concentration corresponds to a bulk refractive index change Δn_B of 6.4×10^{-6} with respect to DI water. Figures 5(a)-(c) show the phase response for 0.01%, 0.03% and 0.05% glucose-water solutions. First the DI water is flown through the sensing window, and then the glucose-water solution is applied in the sensing window. After each measurement, the sensing window is flushed with DI water before repeating the measurement with another glucose concentration. During each glucose-water flow, the phase shift increased in time, although the glucose concentration remained constant. To distinguish the phase shift caused by the RI change of the ambient material from the phase drift caused by the glucose molecule accumulation into the slot, the slope of the phase shift during one minute time period (starting at the moment of glucose-water solution flown into the sensing window) was calculated. This slope of the phase shift is indicated as a dotted line in Fig. 5.

#202021 - $15.00 USD Received 28 Nov 2013; revised 11 Mar 2014; accepted 11 Mar 2014; published 20 Mar 2014

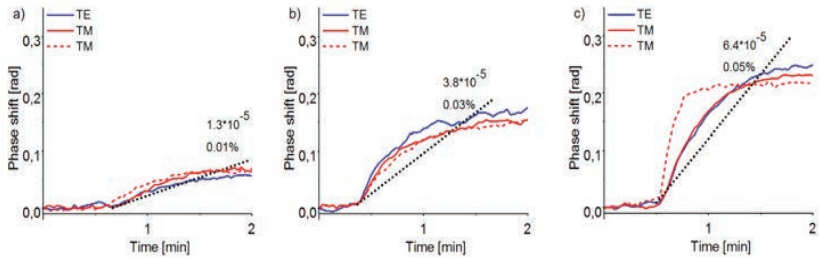

Fig. 5. The phase shift response at TE and TM polarizations measured at various glucose-water concentrations as a function of time, when glucose-water solution is applied to the sensing window. The dashed red line is a repeated measurement for TM polarization. The dotted line indicates the slope of the phase shift in one minute of time. The molar concentration (mol/L) and the corresponding Δn_B with respect to the RI of DI water are marked above the glucose concentration. Glucose concentrations are a) 0.01%, b) 0.03%, and c) 0.05%.

The measured slopes of phase shifts are shown together with simulated phase shifts in Fig. 6. The phase shifts are calculated for the waveguide structures shown in Fig. 2 by the equation

$$\delta = 2\pi \frac{L}{\lambda_0} \Delta n_{eff}, \tag{2}$$

in which L is the length of the slot (or the length of the sensing window), λ_0 is 633 nm, and $\Delta n_{eff} = \partial n_{eff}/\partial n_B$ is the derivative of the effective index change in both waveguide arms as the bulk RI changes. The measured phase responses are in conformity with the simulated phase shifts. The TM polarization shows a slightly higher response compared to the TE polarization. This result is consistent with the theoretical discussion above.

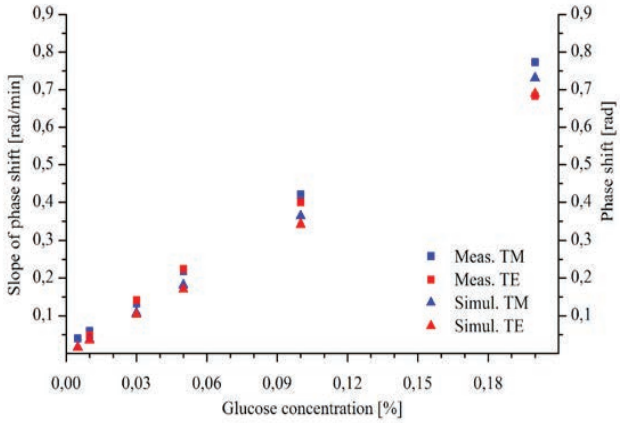

Fig. 6. Plot of the measured slopes of the phase shifts in a one-minute time period, starting at the moment of glucose solution applied in the sensing window. Measurements for TM and TE polarizations are marked as blue and red squares, respectively. The blue (TM polarization) and the red (TE polarization) triangle markers represent the simulated phase shifts at the same glucose concentrations of the fabricated structure.

2.4. Temperature sensitivity of the slot Young interferometer

The stability of the slot Young interferometer against temperature variation was determined for the device with still DI water on the sensor window. The sample was glued to a Peltier heat element and the phase shift was measured as a function of temperature. First, a displacement of mode intensity profiles focused on the camera (Fig. 3(a)) relative to the temperature change was recorded. Due to the thermal expansion of the device holder, the

#202021 - $15.00 USD Received 28 Nov 2013; revised 11 Mar 2014; accepted 11 Mar 2014; published 20 Mar 2014

coupling of the light into the waveguide was lost at the edge of the tunable temperature region, limiting the maximum temperature variation to approximately 5°C. For the phase response measurement, the microscope objective was moved 1.35 mm from the focus to generate the interference pattern (Fig. 3(b)). The fringe pattern was recorded at each temperature after stabilization. TM polarization was chosen for the measurement, because in this polarization state, the loss in slot waveguide was lower. The measurement was performed for two different slot Young interferometers, one with a 5-mm-long slot and another one with a 10-mm-long slot, and also for a reference interferometer (without a slot). In order to remove the thermo-mechanical movement of the device, the displacement of center of mass of the focused mode intensity profiles was extracted from the interference pattern displacement prior the phase shift calculation. The measured and simulated phase shift responses to the temperature change are shown in Table 1. The phase shift is calculated by Eq. (2), with a modification of the symbol Δn_{eff} describing the derivative of the effective RI change in both of the waveguide arms, as the RI of the waveguide and ambient material change. For the simulation, waveguide dimensions in Fig. 2 and the thermo-optic coefficient (TOC) of -2.5×10^{-4}/°C and -9.4×10^{-5}/°C were used for Ormocore and DI water, respectively [27]. There is a good correlation between the measured and simulated phase shifts. The measured phase shift compared to the simulated one is higher in the device with the longer slot, which is potentially attributed to local waveguide variations. Usually, in the integrated Young interferometers detecting ambient RI change, a part of the sensing arm is open, while the rest of the interferometer is protected. Therefore, the thermal phase shift of the structure similar to the regular Young interferometer was also calculated. In the simulation, the whole reference arm was assumed to be covered with Ormostamp (n = 1.515, TOC = -2.8×10^{-4}/°C) and the length of the sensing window in the reference structure (without a slot) was 5 mm. The structure with the whole reference arm protected is more than twice as sensitive to thermal variations. Therefore, the temperature dependence of a slot Young interferometer structure with both sensing and reference arms open is greatly reduced compared to a regular Young interferometer.

Table 1. Measured and simulated phase shifts for temperature change

Device/w Slot length (mm)	Measured phase shift (rad/°C)	Simulated phase shift (rad/°C)	Simulated phase shift covered reference arm (rad//°C)
0 reference	–0.3	0	2.9 (L = 5 mm)
5	2.1	2.2	5.1
10	5.7	4.3	10.1

The slot Young interferometer with a 5-mm-long slot is simulated to have a 2.2 rad/°C response to the temperature change. This is slightly lower than in a ridge Young interferometer with a covered reference arm (2.9 rad/°C). We simulated the phase shift caused by the ambient change from DI water to 1% glucose-water solution for the same structures discussed in the previous paragraph and in Table 1. In these simulations, a constant temperature of 20°C was used. The simulated phase shifts caused by bulk RI change of ambient material for each structure are presented in Table 2.

Table 2. Simulated phase shift for ambient change from DI water to 1% glucose-water solution

Geometry	Phase shift for TM polarization (rad)
Slot YI, 5-mm-long slot waveguide, both arms open	3.6
Slot YI, 5-mm-long slot waveguide, reference arm covered	7.1
Ridge YI, 5-mm-long sensing window, reference arm covered	3.5

The sensitivity of the slot Young interferometer (YI) with both arms open is approximately the same as the sensitivity of the ridge YI with a covered reference arm. The sensitivity of the slot YI is doubled when the reference arm is covered.

#202021 - $15.00 USD Received 28 Nov 2013; revised 11 Mar 2014; accepted 11 Mar 2014; published 20 Mar 2014

3. Conclusions

In this paper, a sensitive polymeric Young interferometer that has a slot waveguide as a sensing region was developed. The emphasis was to demonstrate that high performance sensor configuration is attainable with the simple low-cost UV-nanoimprint fabrication method. This opens up the possibility for mass producible fabrication of disposable sensors. The final device fabrication consists of just a single nanoimprint lithography step, followed by a photolithography step, which determines the window for the analyte fluid flow. The bulk RI response of the slot Young interferometer was characterized with glucose-DI water solutions, both with TE and TM polarization states. The measured responses had a good correlation with the simulated phase responses. The lowest measured RIU change was 6.4×10^{-6}. Both the sensing arm and the reference arm of the interferometer detect the bulk RI change of the ambient material, as well as the ambient temperature changes. The bulk RI sensitivity of the slot Young interferometer could be further increased by covering the reference arm with a cladding layer. The structure with both arms open is simulated to be less than half as sensitive to temperature change than the structure with a covered reference arm. Therefore, the proposed structure geometry effectively compensates for the noise caused by temperature fluctuations.

Acknowledgments

This work was supported by Finnish Academy grants 137331 (M.H.) and 137276 (P.S.).

#202021 - $15.00 USD Received 28 Nov 2013; revised 11 Mar 2014; accepted 11 Mar 2014; published 20 Mar 2014

Series title and number
VTT Science 62

Title	**Polymeric slot waveguide interferometers**
Author(s)	Marianne Hiltunen
Abstract	Slot waveguide is a specific light-guiding structure with a property to enhance the optical field in a nanometer scale void of low refractive index (RI) material embedded between higher RI material rails. Typically, slot waveguides have been fabricated from high refractive index inorganic dielectrics or semiconductors, such as silicon or silicon nitride, and they operate in the near infrared (NIR) wavelength region. The slot waveguide structure enables strong light–ambient interaction, a property that is preferred, for instance, in integrated optical sensors utilizing the change of the refractive index as the sensing transduction signal. In this thesis; the characteristic properties of slot waveguides were studied as regards their usage in polymer platforms. The polymers are transparent in the visible and NIR wavelength region. In this work, the operation of the polymer slot waveguide was demonstrated for both visible and NIR wavelengths by using Young interferometer devices. For the device fabrication, the ultraviolet (UV) assisted nanoimprint moulding method was utilized. The emphasis was to demonstrate that the high performance slot waveguide sensor configuration is attainable with a simple low-cost fabrication method, enabling usage as disposable sensors. The bulk refractive index (RI) response of the slot waveguide-based Young interferometer was characterized with glucose – deionized water solutions. With this arrangement, an ambient RI change of 6.4×10^{-6} was measured. In the slot Young interferometer structure, both waveguide arms of the interferometer detect the bulk RI changes of the ambient material. This novel structure was proved to effectively compensate for thermo-optic originated response drift while maintaining high sensitivity against bulk RI change.
ISBN, ISSN	ISBN 978-951-38-8271-6 (Soft back ed.) ISBN 978-951-38-8272-3 (URL: http://www.vtt.fi/publications/index.jsp) ISSN-L 2242-119X ISSN 2242-119X (Print) ISSN 2242-1203 (Online)
Date	August 2014
Language	English, Finnish abstract
Pages	73 p. + app. 35 p.
Name of the project	
Commissioned by	
Keywords	Slot waveguide, polymer waveguide, nanoimprint moulding, Young interferometer
Publisher	VTT Technical Research Centre of Finland P.O. Box 1000, FI-02044 VTT, Finland, Tel. +358 20 722 111

Julkaisun sarja ja numero
VTT Science 62

Nimeke	**Polymeeriset uravalokanavainterferometrit**
Tekijä(t)	Marianne Hiltunen
Tiivistelmä	Uravalokanavarakenteessa optinen kenttä on vahvistunut nanometrien levyisessä matalataitekertomisessa raossa, jota reunustavat kummaltakin puolelta korkeataitekertomiset harjanteet. Tyypillisesti uravalokanavarakenteet on valmistettu korkean taitekertoimen omaavista epäorgaanisista eristeistä tai puolijohteista, kuten piistä ja pii-nitridistä. Uravalokanava mahdollistaa voimakkaan valon ja materian vuorovaikutuksen. Tämä ominaisuus on erityisen tärkeä optisissa antureissa, joissa taitekertoimen muutosta hyödynnetään signaalin tunnistuksessa. Tässä työssä tutkitaan mahdollisuutta hyödyntää uravalokanavarakenteiden ominaisuuksia käytettäväksi polymeerialustalla. Polymeerit läpäisevät valoa sekä näkyvän että lähi-infrapuna (NIR) aallonpituuden alueilla. Tässä työssä Youngin interferometrirakennetta hyödyntäen osoitettiin polymeeristen uravalokanavien toimivan näkyvällä ja NIR-aallonpituudella. Näytteet valmistettiin UV-valotusta hyödyntävällä painatusmenetelmällä. Tarkoituksena oli osoittaa, että yksinkertaisilla ja edullisilla valmistusmenetelmillä voidaan tehdä herkkiä uravalokanaviin perustuvia anturirakenteita. Rakenteen valmistuskustannusten pienentäminen saattaa mahdollistaa kertakäyttöisten antureiden hyödyntämisen. Uravalokanavaan perustuvan Youngin interferometrin taitekerroinvastetta mitattiin glukoosi- ja ionipoistetun veden liuoksilla. Mittauksilla pystyttiin havaitsemaan suuruudeltaan 6.4×10^{-6} oleva taitekerroinmuutos liuoksessa. Tässä työssä käytetyssä Youngin interferometrirakenteessa sekä anturoiva uravalokanavahaara että referenssivalokanava havaitsevat ympäristön taitekerroinmuutoksen. Tämän uudenlaisen anturirakenteen osoitettiin kompensoivan lämpötilan muutoksesta aiheutuvaa vasteen ryömintää, vaikka rakenne pysyikin samanaikaisesti herkkänä taitekertoimen muutokselle.
ISBN, ISSN	ISBN 978-951-38-8271-6 (nid.) ISBN 978-951-38-8272-3 (URL: http://www.vtt.fi/publications/index.jsp) ISSN-L 2242-119X ISSN 2242-119X (painettu) ISSN 2242-1203 (verkkojulkaisu)
Julkaisuaika	Elokuu 2014
Kieli	Englanti, suomenkielinen tiivistelmä
Sivumäärä	73 s. + liitt. 35 s.
Projektin nimi	
Toimeksiantajat	
Avainsanat	Slot waveguide, polymer waveguide, nanoimprint moulding, Young interferometer
Julkaisija	VTT PL 1000, 02044 VTT, puh. 020 722 111

Polymeric slot waveguide interferometers

Slot waveguide is a specific light-guiding structure with a property to enhance the optical field in a nanometer scale void of low refractive index (RI) material embed-ded between higher RI material rails. Typically, slot waveguides have been fabri-cated from high refractive index inorganic dielectrics or semiconductors, such as silicon or silicon nitride, and they operate in the near infrared (NIR) wavelength region. The slot waveguide structure enables strong light–ambient interaction, a property that is preferred, for instance, in integrated optical sensors utilizing the change of the refractive index as the sensing transduction signal. In this thesis; the characteristic properties of slot waveguides were studied as regards their usage in polymer platforms.

The polymers are transparent in the visible and NIR wavelength region. In this work, the operation of the polymer slot waveguide was demonstrated for both visible and NIR wavelengths by using Young interferometer devices. For the device fabrication, the ultraviolet (UV) assisted nanoimprint moulding method was utilized. The emphasis was to demonstrate that the high performance slot waveguide sensor configuration is attainable with a simple low-cost fabrication method, enabling usage as disposable sensors.

The bulk refractive index (RI) response of the slot waveguide-based Young in-terferometer was characterized with glucose – deionized water solutions. With this arrangement, an ambient RI change of 6.4×10-6 was measured. In the slot Young interferometer structure, both waveguide arms of the interferometer detect the bulk RI changes of the ambient material. This novel structure was proved to effectively compensate for thermo-optic originated response drift while maintaining high sen-sitivity against bulk RI change.

ISBN 978-951-38-8271-6 (Soft back ed.)
ISBN 978-951-38-8272-3 (URL: http://www.vtt.fi/publications/index.jsp)
ISSN-L 2242-119X
ISSN 2242-119X (Print)
ISSN 2242-1203 (Online)